THE UNIVERSITY OF CHICAGO

SENSORIMOTOR REPRESENTATIONS OF MANUAL BEHAVIOR

A DISSERTATION SUBMITTED TO

THE FACULTY OF THE DIVISION OF THE BIOLOGICAL SCIENCES

AND THE PRITZKER SCHOOL OF MEDICINE

IN CANDIDACY FOR THE DEGREE OF

DOCTOR OF PHILOSOPHY

COMMITTEE ON COMPUTATIONAL NEUROSCIENCE

BY

ANEESHA SAHU

CHICAGO, ILLINOIS

DECEMBER 2019

Table of Contents

Table of Figures

Table of Supplementary Figures

Table of Tables

Table of Equations

Acknowledgements

Advisor
Sliman Bensmaia

Thesis Committee
Wim van Drongelen
Murray Sherman
Lee Miller

Neurosurgeons
Joshua Rosenow
Amit Ayer

Bensmaia Lab
Jeremy Winberry
Hannes Saal
Benoit Delhaye
Katie Long
James Goodman

Collaborators
Matthew Kaufman
Nicholas Hatsopoulos
Previous Mentors
Zev Rymer
Sara Aton

Family
Amma (Nina Suresh) : thank you for your relentless encouragement
Appa (Santhanam Suresh)
Sunitha Suresh
Madhav Suresh
Maitrayee Sahu
Abhiram Sahu

Anirban Sahu : thank you for supporting me every step of the way, and reminding me to laugh through the failures and challenges.
Keshav and Kavitha Sahu : thank you for inspiring me to work harder, and remain curious

Dedication| To my Thatha and Patti: KS Rajan, PhD and Sakuntala Rajan

Abstract

The hand is an exceptionally versatile effector that enables a wide range of behaviors, ranging from picking up a coffee cup to playing the piano. From a neural standpoint, the versatility of the hand depend on a sophisticated motor system that has evolved to give rise to dexterity (Bortoff and Strick 1993; Lemon 1999). Manual interactions also require sensory feedback, including vision, proprioception, and touch. Proprioceptive afferents provide weak sensitivity to mechanical fingertip contact (Macefield and Johansson 1996), and visual signals convey little information about contact events. Instead, most manual interactions with objects require the sense of touch, which provides precise information about objects – their local contours, their surface texture, their motion across the skin – and about our interactions with them – the location, magnitude, and directionality of contact forces (Johansson and Flanagan 2009). Ultimately, tactile signals are used to guide object interactions, as evidenced by the deficits that arise when these signals are abolished, through digital anesthesia (Augurelle et al. 2003), or disease (Jeannerod et al. 1984).

The goal of my dissertation is to investigate different representations of hand-object interactions across the neuraxis, beginning with the coding of task relevant features in individual tactile fibers and culminating with representations of hand movements in populations of motor cortical neurons.

Chapter 1 | Introduction

1.1 | Tactile processing pathway

The primary pathway that mediates tactile perception is the medial lemniscal pathway (Figure 1.1). Mechanical signals are transduced by one of four low-threshold cutaneous mechanoreceptive afferents: Slowly Adapting type 1 (SA1) which terminate in Merkel disks, Slowly adapting type 2 SA2 which innervate Ruffini cylinders, rapidly adapting afferents (RA) which innervate Meissner corpuscles, and Pacinian corpuscle (PCs) afferents. SA2 afferents are absent in macaques, and are located around the nail in humans.

Signals from the three classes of cutaneous nerve fibers ascend the ipsilateral posterior column then synapse onto neurons in the cuneate nucleus (CN), located in the medulla. CN axons decussate and travel towards the ventroposterior lateral nucleus of the thalamus.

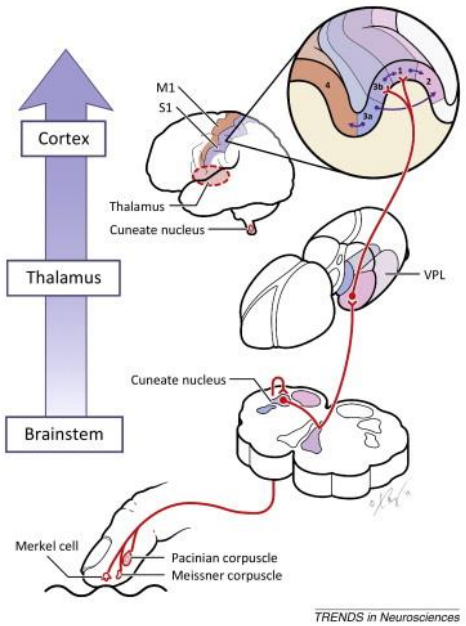

Figure 1.1. Section of the Medial Lemniscal pathway that carries information from the hand. Reproduced from (Saal and Bensmaia 2014a).

Then, tactile thalamic neurons project to areas 3b and 1 of primary somatosensory cortex. The medial lemniscal pathway comprises four main signal processing stages: peripheral, brainstem, thalamic, and cortical. In this thesis, we explore tactile processing in three of these, namely the periphery, the brainstem, and cortex.

1.2 | Tactile signals in the nerve

The function of the different tactile submodalities. One of the most influential theories of tactile coding in the somatosensory nerves is that the different tactile submodalities – SA1, SA2, RA, PC – play different functional roles in touch and remain segregated along the neuraxis. For example, SA1 fibers convey information about shape and texture, RA fibers about motion, SA2 fibers about skin stretch, and PC fibers about distal events (by transducing traveling waves)(Johnson 2001). However, during hand-object interactions, all afferents are activated and recent evidence and reexamination of older evidence suggests that each class of nerve fibers conveys information about most tactile features (Saal and Bensmaia 2014b).

1.2.1| Vibration

The presence of different types of nerve fibers was first discovered in psychophysical experiments in which it was shown that sensitivity to vibrations in different ranges of frequencies could be independently manipulated (Verrillo 1985). Not only do different classes of afferents exhibit different frequency sensitivity profiles, but the investigation of the perception and neural coding of vibrations provides a window into the temporal response properties of somatosensory neurons. Vibrations are also important from an ecological standpoint. Interactions with objects cause propagating vibrations across wide

swaths of skin, which are transduced by PC fibers (Brisben et al. 1999; Manfredi et al. 2012; Shao et al. 2016). Furthermore, texture perception relies on the transduction and processing of vibrations evoked in the skin as we run our fingers across a textured surface (see below). Skin vibrations evoke distinct sensations depending on the mechanical frequency applied (Talbot et al. 1968a). Humans can detect and distinguish skin vibrations precisely, across a wide range of frequencies (Goff 1967; Franzén and Nordmark 1975; Salinas et al. 2000; Güçlü et al. 2002; Simons et al. 2005). In the low frequency, or "flutter" range (5-50Hz), a 10% change in frequency can be perceived 75% of the time, while >100Hz, a 30% change in frequency is required. Each afferent class exhibits distinct sensitivity to a specific frequency bandwidth: SA1s exhibit peak sensitivity at ~5Hz, PC fibers are sensitive to high frequencies (peak 250Hz), and RA fibers are sensitive to a broad range of intermediate frequencies. Furthermore, afferent responses to sinusoidal vibration are phase locked to skin vibrations, spiking within restricted phases of each stimulus cycle (Talbot et al. 1968b; Mackevicius et al. 2012a). This precise patterning has been shown to convey information about stimulus frequency and texture (Mackevicius et al. 2012a; Weber et al. 2013b). In Chapter 6, we investigate how these vibrotactile signals are transformed in the cuneate nucleus.

1.2.2| Shape

During dexterous manipulation, tactile signals convey information about the shape of an object grasped in the hand. Indeed, skin deformations at each point of contact with the object match its local contours. The spatial pattern of the skin indentation is reflected in the spatial pattern of activation evoked in SA1 and RA afferents (Wheat et al. 1995; Wheat

and Goodwin 2000). SA1 afferents provide the most precise and spatially acute information, while RA signals convey more coarse spatial features (Bensmaia et al. 2006). In Chapter 2, we test an alternative hypothesis – that spatial features are encoded in temporal patterns of activation rather than spatial ones.

1.2.3| Texture

Our perception of coarse textural features is mediated by the same mechanism as the one that mediates the perception of local contours: The pattern of skin deformation that is produced by the coarse features is reflected in the spatial pattern of activation in SA1 (and to a lesser extent RA) fibers (Johnson et al. 2000). While the density of innervation of SA1 and RA afferents implies a spatial resolution on the order of 0.5 mm, however, our ability to discriminate surface microstructure extends to features on the order of nanometers (Skedung et al. 2013). To perceive fine textures, we scan our fingers across the surface (Klatzky and Lederman 1993), and without this movement, we cannot discern fine textural features (Hollins and Risner 2000). Scanned movements produce skin vibrations, which excite RA and PC afferents (Weber et al. 2013a). Spatial signals carried by SA1 fibers and temporal signals carried by RA and PC fibers not only convey information about texture but also contribute to its perception. Indeed, spatial and temporal signals can be used to predict the perceived roughness of a surface (Weber et al. 2013a)(see Figure 1.2). In chapter 3, we investigate the degree to which texture signals carried by the three classes of nerve fibers are dependent the way in which textures are explored.

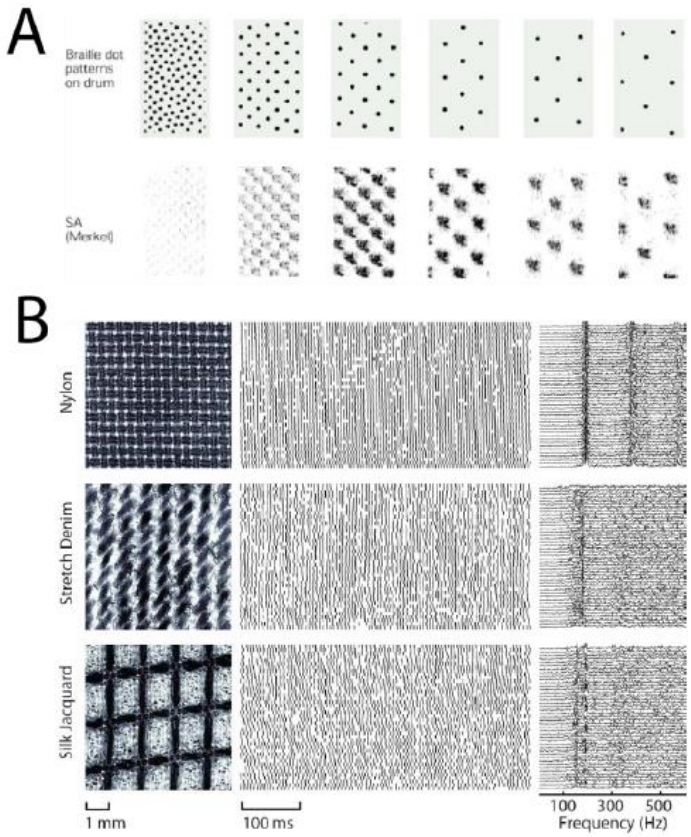

Figure 1.2 | Responses of afferents to texture presentations.
(A) Reconstruction of the response in a population of SA1 afferents evoked by embossed dot patterns scanned across the skin. The spatial configuration of the dots is reflected in the pattern of activation evoked in the afferents. (B) Response of a PC fiber to three finely textured fabrics. Left: Microscope image of the texture; middle: spiking responses to 40 repeated presentations of the textured surface; right: power spectrum of the neural response. Each texture produces a different but highly repeatable temporal spiking pattern (Weber et al., 2013).

1.2.4| Object Manipulation

As noted above, integral to dexterous manipulation are the tactile signals related to contact with objects, including contact force, mostly mediated by SA1 and SA2 fibers. Indeed, these two classes of slowly adapting fibers carry information about both the magnitude and direction of forces exerted on the skin (Birznieks et al. 2001; Wheat et al. 2010). Notably, elimination of these cutaneous cues by anesthetizing fingertips results in a huge increase

in the force exerted on objects during grasp (Augurelle et al. 2003). Object manipulation can be broken down into a sequence of action phases defined by mechanical events associated with the subgoals of the task (Johansson and Flanagan 2009). The task is split into four phases: contact, load, lift, and hold, and afferent response properties vary within each of these phases. For example, during contact and lift, fingerpad afferent responses demonstrate recruitment across large swaths of skin on the hand (Bisley et al. 2000; Birznieks et al. 2001). Within this contact/lift phase, first spike latency has been shown to encode surface curvature (Johansson and Flanagan 2009). Due to the challenging nature of recording afferent activity during dynamic tasks, there are many unanswered questions in regards to how afferents encode specific features of hand-object interactions. In chapter 4, we attempt to fill this gap by investigating how populations of afferents encode features of contact events.

1.3 | Tactile signals in cortex

The main cortical recipient of tactile signals from the periphery is the somatosensory cortex (SCx), which consists of Brodmann areas 3a, 3b 1 and 2. Area 3b – primary somatosensory cortex proper – receives the strongest thalamocortical projections and areas 1 and 2 are considered higher cortical areas due to their large RFs and complex response properties (Felleman and Van Essen 1991). That all four cortical fields – areas 3a, 3b, 1 and 2 – are referred to as primary somatosensory cortex is thus a misnomer (Kaas et al. 1979; Krubitzer et al. 1990; Reed et al. 2010).

1.3.1 Convergence of afferent modalities

As discussed above, mechanoreceptive afferents were thought to play mutually exclusive functional roles based on their response properties and signals from the various classes of nerve fibers were thought to remain segregated throughout the neuraxis, including somatosensory cortex. That is, individual cortical neurons were thought to receive input from only one type of nerve fiber. However, recent evidence and reexamination of the data from the original studies have revealed that cortical responses integrate input from

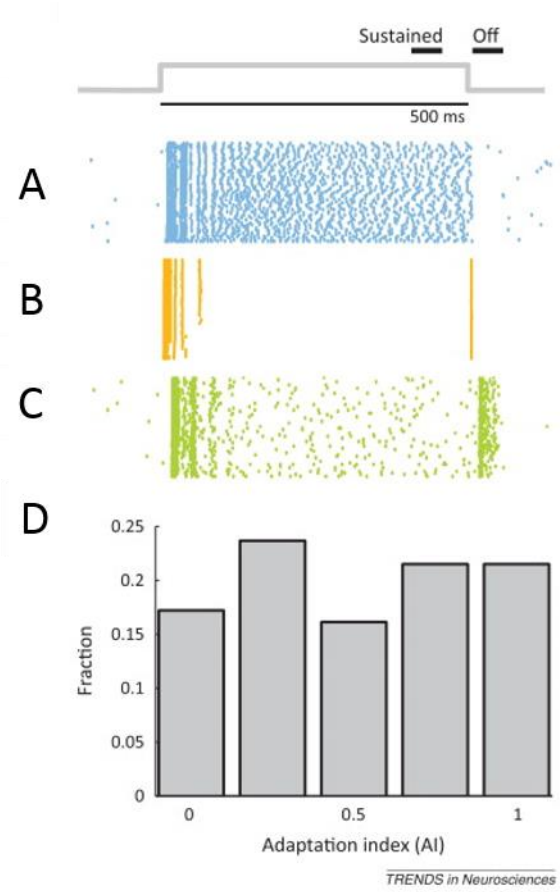

Figure 1.3. Adaptation responses in cortex demonstrate submodality convergence.

(A) Responses of a typical slowly adapting type 1 (SA1) afferent to 60 repeated presentations of a step indentation lasting 500 ms (depicted by the grey trace at the top). (B) Responses of a rapidly adapting (RA) afferent to the same stimulus. (C) Response of a typical neuron in area 3b. (D) The adaptation index, AI, is determined by the ratio of the OFF response to the SUSTAINED response, each normalized by their respective population means.

multiple submodality classes (Pei et al. 2009; Saal and Bensmaia 2014b). A clear manifestation of this integration is observed in the cortical responses to step indentations (Fig 1.3). While SA1 fibers exhibit sustained responses and no off-response (Fig. 1.3A) and RA responses exhibit off-responses but no sustained response (Fig 1.3B), individual S1 neuron tend to exhibit both, indicating convergent input from the two populations (Figure 1.3C). The adaptation index, which gauges the degree to which individual neurons exhibit sustained responses exclusively (AI=0, SA1-like), off responses exclusively (AI=1, RA-like), or both (0<AI<1) is uniformly distributed over the range of possible values, demonstrating that cortical neurons tend to receive convergent input from more than one class of nerve fibers (Fig 2D). Previous work has suggested that afferent channels remain segregated at intermediate processing areas, including in the cuneate nucleus (Dykes et al. 1982), but the determination of submodality input was qualitative, an approach that had also led to the erroneous conclusion that cortical responses were unimodal. Thus, the degree of submodality convergence in subcortical structures needs to be re-examined, which we do in chapter 6.

1.3.2 | Receptive Field Structure of S1 neurons

A well-established property of S1 neurons is that their receptive fields comprise excitatory subfields flanked by inhibitory ones, resembling their counterparts in primary visual cortex (V1)(DiCarlo et al. 1998). Furthermore, S1 RFs tend to be elongated, as are their V1 counterparts, which confers to the neurons a selectivity for the orientation of edges indented or scanned across the skin (Bensmaia et al. 2008). Whether this RF structure and the resulting orientation tuning first emerges in S1 or is inherited from upstream structures

remains to be determined, and a question we hope to begin to address in our study of the CN (See Chapter 6).

1.3.3| Coding of Vibrotactile Signals in S1

As detailed above, the different classes of nerve fibers exhibit different frequency sensitivity profiles for vibrotactile stimulation: SA1 afferents are most sensitive at low frequencies (peak sensitivity ~5Hz), PC fibers at high frequencies (peak 250Hz), and RA fibers at intermediate frequencies. Since S1 neurons receive convergent input from multiple afferent classes, they tend to exhibit broader bandwidth than do individual nerve fibers (Harvey et al. 2013a; Saal et al. 2015).

As is the case in nerve fibers, S1 neurons exhibit phase locked responses to skin vibrations. However, phase-locking weakens as frequency increases, with only a small proportion of S1 neurons phase-locked above 300 Hz, though phase locking is sometimes observed up to 800 Hz (Harvey et al. 2013a). S1 firing rates tend to increase with frequency up to about 50 Hz, after which they become nearly frequency independent; at the higher frequencies, phase locking is preserved, but individual neurons do not necessarily spike on every stimulus cycle. At those frequencies, information about frequency is thought to be conveyed in the temporal patterning across a subpopulation of neurons.

The responses of nerve fibers increases as the vibratory amplitude increases, but since the response is also frequency dependent, information about amplitude is ambiguous, both at the single neuron level and at the population level (Mackevicius et al. 2012b). S1 responses to vibrations also increases with amplitude (Talbot et al. 1968a; Harvey et al. 2013b), and these are also frequency dependent up to 50Hz (Hernández et al. 2000; Salinas et al. 2000)

so, at those frequencies, amplitude and frequency are confounded in the rates. In contrast, the relationship between firing rate and amplitude is nearly frequency independent for high frequency vibrations (> 50 Hz), so information about amplitude is unambiguously in cortical firing rates (Saal et al. 2015). In chapter 6, we examine how skin vibrations are encoded in CN and compare these vibrotactile representations with cortical counterparts.

1.4 | Neural Representations of Hand Movements

Dexterous manipulation of objects involves the simultaneous control of more than 20 degrees of mechanical degrees of freedom and 39 muscles (Schieber and Santello 2004). The human hand is remarkably versatile, enabling a wide range of behaviors, ranging from adopting appropriate hand postures for grasping to moving individual fingers for typing or playing the piano. Notably, in humans, basic grasping behavior is present at birth, before we can walk, talk, or perform other most other basic motor functions. As development progresses, the ability to perform individuated finger movements matures (Forssberg et al. 1992).

1.4.1 | Hand Behavior during Grasping

Reaching to grasp is an intentional movement that involves three distinct processes: target identification, action planning, and action execution. During reaching movements, the hand pre-shapes to the object to be grasped, demonstrating that finger movements exhibit precise coordination well before they are forced to conform to the shape of an object (Santello and Soechting 1998; Mason et al. 2001). Analysis of hand kinematics during grasping reveals that these movements may be simpler than one might expect given the apparent complexity of the hand. Indeed, dimensionality reduction techniques, such as

principal components analysis, reveal that a very small number of dimensions can account for a large amount of variance in grasp kinematics (Mason et al. 2001). However, while lower order components (reflecting covariation in the metacarpophalageal and proximal interphalangeal joints (Santello et al. 1998, 2002)) capture the coarse structure of hand postures, higher-order components exhibit a high degree of task dependence, suggesting they too are under volitional control (Yan et al. 2019). In other words, while a small number of dimensions capture the coarse structure of hand movements, these seem to occupy a high dimensional space, which implies a sophisticated sensory and motor system.

1.4.2| Primary Motor Cortical Representations of Hand Movements

Primary motor cortex descends projections to the spinal cord along the corticospinal tract to control limb movements. This pathway is essential for hand control as evidenced by the fact that lesions to these areas impair skilled and coordinated hand movements (Lang and Schieber 2003). Reversible inactivation of monkey M1 hand representation also results in weakened individuated finger movements while maintaining coarse grasp capability, which suggests that other pathways, possibly subcortical, may mediate simple manual behaviors (Schieber and Poliakov 1998; Brochier et al. 1999). Importantly, a subset of M1 efferents reveal monosynaptic spinal projections, which have been shown to play an integral role in the generation of individuated finger movements (Lemon et al. 1995).

Individual M1 neurons innervate motoneuron pools spanning a range of forearm and intrinsic hand muscles rather than individual muscles (Fetz and Cheney 1980; Buys et al. 1986). As might be expected, then, the somatotopic organization of M1 is much less well defined than is that of S1. Indeed, inactivation of part of the hand representation in

macaque M1 impairs one finger more than the others, but adjacent fingers are not weakened more than are nonadjacent fingers (Schieber and Hibbard 1993). In humans, small strokes in the M1 hand representation affect thumb and index finger movements more than other fingers (Schieber 1999). Although coarse somatotopy has been observed, M1 neurons have been shown to encode coordinated, rather than individual finger movements: single M1 units exhibit broad tuning for all digits and the wrist (Schieber and Hibbard 1993; Schieber 2002; Goodman et al. 2019). Indeed, M1 neurons with similar muscle outputs are spatially clustered and often are co-activated, which suggest a functional topography in M1 but one that is not explicitly somatotopic (Cheney and Fetz 1985; Jackson et al. 2003). One possibility is that muscle synergies underlie this functional organization, but the evidence for this hypothesis is mixed (Overduin et al. 2012; Kirsch et al. 2014; Mollazadeh et al. 2014; Leo et al. 2016).

Although the hand representation in M1 exhibits a semblance of somatotopic and functional organization, the nature of this representation remains elusive. Specifically, the relationship between movement parameters and M1 firing rates has yet to be established. In light of this ambiguity, M1 has been hypothesized to act as a pattern generator rather than explicitly representing movements (Churchland et al. 2010; Ames et al. 2014; Kaufman et al. 2014; Elsayed et al. 2016; Stavisky et al. 2017). Specifically, the dynamics of the responses of populations of M1 neurons drive the muscles that give rise to movement. According to this view, there is no explicit relationship between the responses of individual neurons and movement features. However, these studies have focused on the proximal limb as animals perform planar reaching or cycling movements, so the question remains

whether the principles of motor control derived from these studies will extend to hand control for more complex tasks (Gao and Ganguli 2015; Gao et al. 2017) (although see (Gallego et al. 2018) for methods to dissociate low-dimensional manifolds from task constraints). In the last chapter of this thesis, we apply population-level analyses to the neuronal representations of grasp, which requires complex coordination of the hand to conform to a wide variety of different objects. We assess the dynamical systems hypothesis of M1 function in the context of hand movements.

1.5 | References

Ames KC, Ryu SI, Shenoy KV. Neural Dynamics Of Reaching Following Incorrect Or Absent Motor Preparation. *Neuron* 81: 438–451, 2014.

Augurelle A-S, Smith AM, Lejeune T, Thonnard J-L. Importance Of Cutaneous Feedback In Maintaining A Secure Grip During Manipulation Of Hand-Held Objects. *J Neurophysiol* 89: 665–71, 2003.

Bensmaia SJ, Craig JC, Yoshioka T, Johnson KO. SA1 And RA Afferent Responses To Static And Vibrating Gratings [Online]. *J Neurophysiol* 95: 1771–1782, 2006. Http://Jn.Physiology.Org/Content/95/3/1771.Short [21 Aug. 2014].

Bensmaia SJ, Denchev P V., Dammann JF, Craig JC, Hsiao SS. The Representation Of Stimulus Orientation In The Early Stages Of Somatosensory Processing. *J Neurosci* 28: 776–786, 2008.

Birznieks I, Jenmalm P, Goodwin AW, Johansson RS. Encoding Of Direction Of Fingertip Forces By Human Tactile Afferents. *J Neurosci* 21: 8222–37, 2001.

Bisley JW, Goodwin AW, Wheat HE. Slowly Adapting Type I Afferents From The Sides And End Of The Finger Respond To Stimuli On The Center Of The Fingerpad. *J Neurophysiol* 84: 57–64, 2000.

Bortoff GA, Strick PL. Corticospinal Terminations In Two New-World Primates: Further Evidence That Corticomotoneuronal Connections Provide Part Of The Neural Substrate For Manual Dexterity. *J Neurosci* 13: 5105–18, 1993.

Brisben AJ, Hsiao SS, Johnson KO. Detection Of Vibration Transmitted Through An Object Grasped In The Hand. *J Neurophysiol* 81: 1548–1558, 1999.

Brochier T, Boudreau MJ, Paré M, Smith AM. The Effects Of Muscimol Inactivation Of Small Regions Of Motor And Somatosensory Cortex On Independent Finger Movements

And Force Control In The Precision Grip. [Online]. *Exp Brain Res* 128: 31–40, 1999. Http://Www.Ncbi.Nlm.Nih.Gov/Pubmed/10473737 [6 Aug. 2018].

Buys EJ, Lemon RN, Mantel GW, Muir RB. Selective Facilitation Of Different Hand Muscles By Single Corticospinal Neurones In The Conscious Monkey. *J Physiol* 381: 529–549, 1986.

Cheney PD, Fetz EE. Comparable Patterns Of Muscle Facilitation Evoked By Individual Corticomotoneuronal (CM) Cells And By Single Intracortical Microstimuli In Primates: Evidence For Functional Groups Of CM Cells. *J Neurophysiol* 53: 786–804, 1985.

Churchland MM, Cunningham JP, Kaufman MT, Ryu SI, Shenoy K V. Cortical Preparatory Activity: Representation Of Movement Or First Cog In A Dynamical Machine? *Neuron* 68: 387–400, 2010.

Dicarlo J, Neuroscience KJ-J Of, 2000 Undefined. Spatial And Temporal Structure Of Receptive Fields In Primate Somatosensory Area 3b: Effects Of Stimulus Scanning Direction And Orientation [Online]. *Soc Neurosci.* Http://Www.Jneurosci.Org/Content/20/1/495.Short [3 May 2018].

Dicarlo JJ, Johnson KO, Hsiao SS. Structure Of Receptive Fields In Area 3b Of Primary Somatosensory Cortex In The Alert Monkey. *J Neurosci* 18: 2626–45, 1998.

Dykes RW, Rasmusson DD, Sretavan D, Rehman NB. Submodality Segregation And Receptive-Field Sequences In Cuneate, Gracile, And External Cuneate Nuclei Of The Cat. [Online]. *J Neurophysiol* 47: 389–416, 1982. Http://Jn.Physiology.Org/Content/Jn/47/3/389.Full.Pdf [20 Aug. 2014].

Elsayed GF, Lara AH, Kaufman MT, Churchland MM, Cunningham JP. Reorganization Between Preparatory And Movement Population Responses In Motor Cortex. *Nat Commun* 7: 13239, 2016.

Felleman DJ, Van Essen DC. Distributed Hierarchical Processing In The Primate Cerebral Cortex. *Cereb Cortex* 1: 1–47, 1991.

Fetz EE, Cheney PD. Postspike Facilitation Of Forelimb Muscle Activity By Primate Corticomotoneuronal Cells. *J Neurophysiol* 44: 751–772, 1980.

Forssberg H, Kinoshita H, Eliasson AC, Johansson RS, Westling G, Gordon AM. Development Of Human Precision Grip. *Exp Brain Res* 90: 393–398, 1992.

Franzén O, Nordmark J. Vibrotactile Frequency Discrimination. *Percept Psychophys* 17: 480–484, 1975.

Gallego JA, Perich MG, Naufel SN, Ethier C, Solla SA, Miller LE. Cortical Population Activity Within A Preserved Neural Manifold Underlies Multiple Motor Behaviors. *Nat Commun* 9: 4233, 2018.

Gao P, Ganguli S. On Simplicity And Complexity In The Brave New World Of Large-Scale Neuroscience. *Curr Opin Neurobiol* 32: 148–155, 2015.

Gao P, Trautmann E, Yu BM, Santhanam G, Ryu S, Shenoy K, Ganguli S. A Theory Of Multineuronal Dimensionality, Dynamics And Measurement. *Biorxiv* (November 5, 2017). Doi: 10.1101/214262.

Goff GD. Differential Discrimination Of Frequency Of Cutaneous Mechanical Vibration. *J Exp Psychol* 74: 294–299, 1967.

Goodman JM, Tabot GA, Lee AS, Suresh AK, Rajan AT, Hatsopoulos NG, Bensmaia SJ. Postural Representations Of The Hand In Primate Sensorimotor Cortex. *Biorxiv* (March 2019). Doi: 10.1101/566539.

Tommerdahl M, Whitsel B, Tommerdahl M, Whitsel B, Favorov O, Metz C, BL O, Jones E, Porter R, Powell T, Mountcastle V. Amplitude-Dependency Of Response Of SI Cortex To Flutter Stimulation. *J Comput Neurosci* 12: 201–218, 2002.

Harvey MA, Saal HP, Dammann 3rd JF, Bensmaia SJ. Multiplexing Stimulus Information Through Rate And Temporal Codes In Primate Somatosensory Cortex. *Plos Biol* 11: E1001558, 2013a.

Harvey MA, Saal HP, Dammann III JF, Bensmaia SJ, Iii JFD, Bensmaia SJ. Multiplexing Stimulus Information Through Rate And Temporal Codes In Primate Somatosensory Cortex. *Plos Biol* 11: E1001558, 2013b.

Hernández A, Zainos A, Romo R. Neuronal Correlates Of Sensory Discrimination In The Somatosensory Cortex. *Proc Natl Acad Sci* 97: 6191–6196, 2000.

Hollins M, Risner SR. Evidence For The Duplex Theory Of Tactile Texture Perception. *Percept Psychophys* 62: 695–705, 2000.

Jackson A, Gee VJ, Baker SN, Lemon RN. Synchrony Between Neurons With Similar Muscle Fields In Monkey Motor Cortex. [Online]. *Neuron* 38: 115–25, 2003. Http://Www.Ncbi.Nlm.Nih.Gov/Pubmed/12691669 [16 Jul. 2019].

Jeannerod M, Michel F, Prablanc C. The Control Of Hand Movements In A Case Of Hemianaesthesia Following A Parietal Lesion. *Brain* 107: 899–920, 1984.

Johansson RS, Flanagan JR. Coding And Use Of Tactile Signals From The Fingertips In Object Manipulation Tasks. *Nat Rev Neurosci* 10: 345–59, 2009.

Johnson KO. The Roles And Functions Of Cutaneous Mechanoreceptors. *Curr Opin Neurobiol* 11: 455–461, 2001.

Johnson KO, Yoshioka T, Vega-Bermudez F. Tactile Functions Of Mechanoreceptive Afferents Innervating The Hand. [Online]. *J Clin Neurophysiol* 17: 539–58, 2000. Http://Www.Ncbi.Nlm.Nih.Gov/Pubmed/11151974 [23 Jul. 2019].

Kaas JH, Nelson RJ, Sur M, Lin CS, Merzenich MM. Multiple Representations Of The Body Within The Primary Somatosensory Cortex Of Primates. *Science* 204: 521–3, 1979.

Kaufman MT, Churchland MM, Ryu SI, Shenoy K V. Cortical Activity In The Null Space:

Permitting Preparation Without Movement. *Nat Neurosci* 17: 440–448, 2014.

Kirsch E, Rivlis G, Schieber MH. Primary Motor Cortex Neurons During Individuated Finger And Wrist Movements: Correlation Of Spike Firing Rates With The Motion Of Individual Digits Versus Their Principal Components [Online]. *Front Neurol* 5, 2014. Http://Www.Ncbi.Nlm.Nih.Gov/Pmc/Articles/PMC4032981/ [24 Sep. 2014].

Klatzky RL, Lederman SJ. Toward A Computational Model Of Constraint-Driven Exploration And Haptic Object Identification. *Perception* 22: 597–621, 1993.

Krubitzer LA, Kaas JH, Kaas JH. The Organization And Connections Of Somatosensory Cortex In Marmosets. *J Neurosci* 10: 952–74, 1990.

Lang CE, Schieber MH. Differential Impairment Of Individuated Finger Movements In Humans After Damage To The Motor Cortex Or The Corticospinal Tract. *J Neurophysiol* 90: 1160–1170, 2003.

LAWRENCE DG, KUYPERS HGJM. THE FUNCTIONAL ORGANIZATION OF THE MOTOR SYSTEM IN THE MONKEY. *Brain* 91: 1–14, 1968.

Lemon RN. Neural Control Of Dexterity: What Has Been Achieved? *Exp Brain Res* 128: 6–12, 1999.

Lemon RN, Johansson RS, Westling G. Corticospinal Control During Reach, Grasp, And Precision Lift In Man. *J Neurosci* 15: 6145–56, 1995.

Leo A, Handjaras G, Bianchi M, Marino H, Gabiccini M, Guidi A, Scilingo EP, Pietrini P, Bicchi A, Santello M, Ricciardi E. A Synergy-Based Hand Control Is Encoded In Human Motor Cortical Areas. *Elife* 5, 2016.

Macefield V, Johansson R. Control Of Grip Force During Restraint Of An Object Held Between Finger And Thumb: Responses Of Muscle And Joint Afferents From The Digits. *Exp Brain Res* 108, 1996.

Mackevicius EL, Best MD, Saal HP, Bensmaia SJ. Millisecond Precision Spike Timing Shapes Tactile Perception. *J Neurosci* 32: 15309–15317, 2012a.

Mackevicius EL, Best MD, Saal HP, Bensmaia SJ. Millisecond Precision Spike Timing Shapes Tactile Perception. *J Neurosci* 32: 15309–15317, 2012b.

Manfredi LR, Baker AT, Elias DO, Dammann 3rd JF, Zielinski MC, Polashock VS, Bensmaia SJ, Dammann JF, Zielinski MC, Polashock VS, Bensmaia SJ, Dammann 3rd JF, Zielinski MC, Polashock VS, Bensmaia SJ, Dammann JF, Zielinski MC, Polashock VS, Bensmaia SJ, Dammann 3rd JF, Zielinski MC, Polashock VS, Bensmaia SJ, Dammann JF, Zielinski MC, Polashock VS, Bensmaia SJ, Dammann 3rd JF, Zielinski MC, Polashock VS, Bensmaia SJ. The Effect Of Surface Wave Propagation On Neural Responses To Vibration In Primate Glabrous Skin. *Plos One* 7: E31203, 2012.

Mason CR, Gomez JE, Ebner TJ. Hand Synergies During Reach-To-Grasp | Journal Of Neurophysiology [Online]. *J Neurophysiol* 86: 2896–2910, 2001.

Http://Jn.Physiology.Org/Content/86/6/2896.Short [22 Aug. 2014].

Mollazadeh M, Aggarwal V, Thakor N V., Schieber MH. Principal Components Of Hand Kinematics And Neurophysiological Signals In Motor Cortex During Reach To Grasp Movements. *J Neurophysiol* 112: Jn–00481, 2014.

Overduin SA, d'Avella A, Carmena JM, Bizzi E. Microstimulation Activates A Handful Of Muscle Synergies. *Neuron* 76: 1071–1077, 2012.

Pei Y-C, Denchev P V., Hsiao SS, Craig JC, Bensmaia SJ. Convergence Of Submodality-Specific Input Onto Neurons In Primary Somatosensory Cortex [Online]. *J Neurophysiol* 102: 1843–1853, 2009. Http://Jn.Physiology.Org/Content/102/3/1843.Short [21 Aug. 2014].

Reed JL, Qi H-X, Zhou Z, Bernard MR, Burish MJ, Bonds AB, Kaas JH. Response Properties Of Neurons In Primary Somatosensory Cortex Of Owl Monkeys Reflect Widespread Spatiotemporal Integration. *J Neurophysiol* 103: 2139–2157, 2010.

Saal HP, Bensmaia SJ. Touch Is A Team Effort: Interplay Of Submodalities In Cutaneous Sensibility. *Trends Neurosci* 37: 689–697, 2014a.

Saal HP, Bensmaia SJ. Touch Is A Team Effort: Interplay Of Submodalities In Cutaneous Sensibility. *Trends Neurosci* 37: 689–697, 2014b.

Saal HP, Harvey MA, Bensmaia SJ. Rate And Timing Of Cortical Responses Driven By Separate Sensory Channels. *Elife* 4: E10450, 2015.

Salinas E, Hernandez A, Zainos A, Romo R. Periodicity And Firing Rate As Candidate Neural Codes For The Frequency Of Vibrotactile Stimuli. *J Neurosci* 20: 5503–15, 2000.

Santello M, Flanders M, Soechting JF. Postural Hand Synergies For Tool Use [Online]. *J Neurosci* 18: 10105–10115, 1998. Http://Www.Jneurosci.Org/Content/18/23/10105 [20 Aug. 2014].

Santello M, Flanders M, Soechting JF. Patterns Of Hand Motion During Grasping And The Influence Of Sensory Guidance [Online]. *J Neurosci* 22: 1426–1435, 2002. Http://Www.Jneurosci.Org/Content/22/4/1426 [20 Aug. 2014].

Santello M, Soechting JF. Gradual Molding Of The Hand To Object Contours [Online]. *J Neurophysiol* 79: 1307–1320, 1998. Http://Jn.Physiology.Org/Content/79/3/1307 [29 Apr. 2015].

Schieber MH. Somatotopic Gradients In The Distributed Organization Of The Human Primary Motor Cortex Hand Area: Evidence From Small Infarcts. [Online]. *Exp Brain Res* 128: 139–48, 1999. Http://Www.Ncbi.Nlm.Nih.Gov/Pubmed/10473752 [16 Jul. 2019].

Schieber MH. Motor Cortex And The Distributed Anatomy Of Finger Movements. In: *Advances In Experimental Medicine And Biology*, P. 411–416.

Schieber MH, Hibbard LS. How Somatotopic Is The Motor Cortex Hand Area? [Online]. *Science (80-)* 261: 489–492, 1993. Http://Www.Jstor.Org/Stable/2881942 [22 Apr. 2015].

Schieber MH, Poliakov A V. Partial Inactivation Of The Primary Motor Cortex Hand Area: Effects On Individuated Finger Movements. *J Neurosci* 18: 9038–54, 1998.

Schieber MH, Santello M. Hand Function: Peripheral And Central Constraints On Performance. *J Appl Physiol* 96: 2293–2300, 2004.

Shao Y, Hayward V, Visell Y. Spatial Patterns Of Cutaneous Vibration During Whole-Hand Haptic Interactions. *Proc Natl Acad Sci U S A* 113: 4188–93, 2016.

Simons SB, Tannan V, Chiu J, Favorov O V, Whitsel BL, Tommerdahl M. Amplitude-Dependency Of Response Of SI Cortex To Flutter Stimulation. *BMC Neurosci* 6: 43, 2005.

Skedung L, Arvidsson M, Chung JY, Stafford CM, Berglund B, Rutland MW. Feeling Small: Exploring The Tactile Perception Limits. *Sci Rep* 3: 2617, 2013.

Stavisky SD, Kao JC, Ryu SI, Shenoy K V. Motor Cortical Visuomotor Feedback Activity Is Initially Isolated From Downstream Targets In Output-Null Neural State Space Dimensions. *Neuron* 95: 195–208.E9, 2017.

Talbot WH, Darian-Smith I, Kornhuber HH, Mountcastle VB. The Sense Of Flutter-Vibration: Comparison Of The Human Capacity With Response Patterns Of Mechanoreceptive Afferents From The Monkey Hand. [Online]. *J Neurophysiol* 31: 301–34, 1968a. Http://Www.Ncbi.Nlm.Nih.Gov/Pubmed/4972033 [11 Oct. 2017].

Talbot WH, Darian-Smith I, Kornhuber HH, Mountcastle VB. The Sense Of Flutter-Vibration: Comparison Of The Human Capacity With Response Patterns Of Mechanoreceptive Afferents From The Monkey Hand. *J Neurophysiol* 31: 301–34, 1968b.

Verrillo RT. Psychophysics Of Vibrotactile Stimulation. *J Acoust Soc Am* 77: 225–232, 1985.

Weber AI, Saal HP, Lieber JD, Cheng J-WW, Manfredi LR, Dammann 3rd JF, Bensmaia SJ, Dammann JF, Bensmaia SJ. Spatial And Temporal Codes Mediate The Tactile Perception Of Natural Textures. *Proc Natl Acad Sci* 110: 17107–17112, 2013a.

Weber AI, Saal HP, Lieber JD, Cheng JW, Manfredi LR, Dammann 3rd JF, Bensmaia SJ. Spatial And Temporal Codes Mediate The Tactile Perception Of Natural Textures. *Proc Natl Acad Sci U S A* 110: 17107–17112, 2013b.

Wheat HE, Goodwin AW. Tactile Discrimination Of Gaps By Slowly Adapting Afferents: Effects Of Population Parameters And Anisotropy In The Fingerpad. *J Neurophysiol* 84: 1430–1444, 2000.

Wheat HE, Goodwin AW, Browning AS. Tactile Resolution: Peripheral Neural Mechanisms Underlying The Human Capacity To Determine Positions Of Objects Contacting The Fingerpad [Online]. *J Neurosci* 75: 5582–5595, 1995. Http://Www.Jneurosci.Org/Content/Jneuro/15/8/5582.Full.Pdf [8 Dec. 2017].

Wheat HE, Salo LM, Goodwin AW. Cutaneous Afferents From The Monkeys Fingers: Responses To Tangential And Normal Forces. *J Neurophysiol* 103: 950–961, 2010.

Yan Y, Goodman JG, Bensmaia SJ. Unexpected Complexity Of Everyday Manual Behaviors. *Biorxiv* (July 8, 2019). Doi: 10.1101/694778.

Chapter 2 | Edge Orientation Signals in Tactile Afferents of Macaques[1]

The orientation of edges indented into the skin has been shown to be encoded in the responses of neurons in primary somatosensory cortex in a manner that draws remarkable analogies to their counterparts in primary visual cortex. According to the classical view, orientation tuning arises from the integration of untuned input from thalamic neurons with aligned but spatially displaced receptive fields (RFs). In a recent microneurography study with human subjects, the precise temporal structure of the responses of individual mechanoreceptive afferents to scanned edges was found to carry information about their orientation. This putative mechanism could in principle contribute to or complement the classical rate-based code for orientation.

In the present study, we further examine orientation information carried by mechanoreceptive afferents of Rhesus monkeys. To this end, we recorded the activity evoked in cutaneous mechanoreceptive afferents when edges are indented into or scanned across the skin. First, we confirmed that information about the edge orientation can be extracted from the temporal patterning in afferent responses of monkeys, as is the case in humans. Second, we found that while the coarse temporal profile of the response can be predicted linearly from the layout of the RF, the fine temporal profile cannot. Finally, we show that orientation signals in tactile afferents are often highly dependent on stimulus features other than orientation, which complicates putative decoding strategies. We

[1] This chapter was published : Suresh AK, Saal HP, Bensmaia SJ (2016) Edge orientation signals in tactile afferents of macaques. J Neurophysiol 116:2647–2655

discuss the challenges associated with establishing a neural code at the somatosensory periphery, where afferents are exquisitely sensitive and nearly deterministic.

2.1| Introduction

Our ability to dexterously grasp and manipulate objects relies critically on our sense of touch, without which we would struggle to perform even the most basic activities of daily living (Witney et al. 2004; Johansson and Flanagan 2009). To successfully grasp and manipulate an object requires that we acquire information about the object at the contact points (Augurelle et al. 2003). Neurons in primary somatosensory cortex (S1) exhibit strong tuning for edge orientation in their firing rates, a tuning that is not observed in the responses of cutaneous mechanoreceptive afferents (Warren et al. 1986; Bensmaia et al. 2008a). The orientation tuning in S1 draws a powerful analogy to that found in primary visual cortex (Pack and Bensmaia 2015), which is thought to originate from the integration of weakly tuned input from thalamic neurons with spatially displaced receptive fields, as first proposed by Hubel and Wiesel (Hubel and Wiesel 1962; Priebe and Ferster 2012).

The classical model of orientation coding in vision may not tell the whole story about how tactile edges are encoded, however. In recent microneurography experiments with human subjects, temporal spiking patterns of cutaneous mechanoreceptive afferents were shown to carry information about edge orientation not in their rates but in their precise spiking patterns. Indeed, the temporal sequence of spikes evoked by scanned edges in two types of tactile fibers – slowly adapting type 1 (SA1) and rapidly adapting (RA) afferents – differed depending on the orientation of the edges (Pruszynski and Johansson 2014). Receptive

fields (RFs) comprise multiple hotspots, (Cauna 1956; Johansson 1978; Paré et al. 2002) so scanning edges across the RF at different orientations excite the fiber's hotspots in different sequences. The different sequences of hotspot recruitment was hypothesize to drive the orientation-dependence of the spiking patterns. In principle, then, these orientation signals in the nerve could contribute to the tuning in S1 or serve to complement rate-based representations of edge orientation (Scholl et al. 2013).

In the present study, we investigated the nature of the orientation signals at the tactile periphery. First, we determined whether monkey afferents convey information about edge orientation in their responses. Next, we assessed the degree to which these afferent responses could be predicted from RF topography. Third, we assessed whether edge orientation signals in tactile afferents are robust to changes in other stimulus parameters, for example scanning direction or indentation depth, as rate-based cortical representations tend to be (Bensmaia et al. 2008a). Finally, we discuss the implications of these results on tactile orientation processing and consider the challenges associated with establishing a neural code at the somatosensory periphery.

2.2 | Results

We recorded the responses of 22 afferents (12 SA1 and 10 RA) to scanned edges and of a subset of these to indented edges (18 total: 10 SA1 and 8 RA, Figure 2.1).

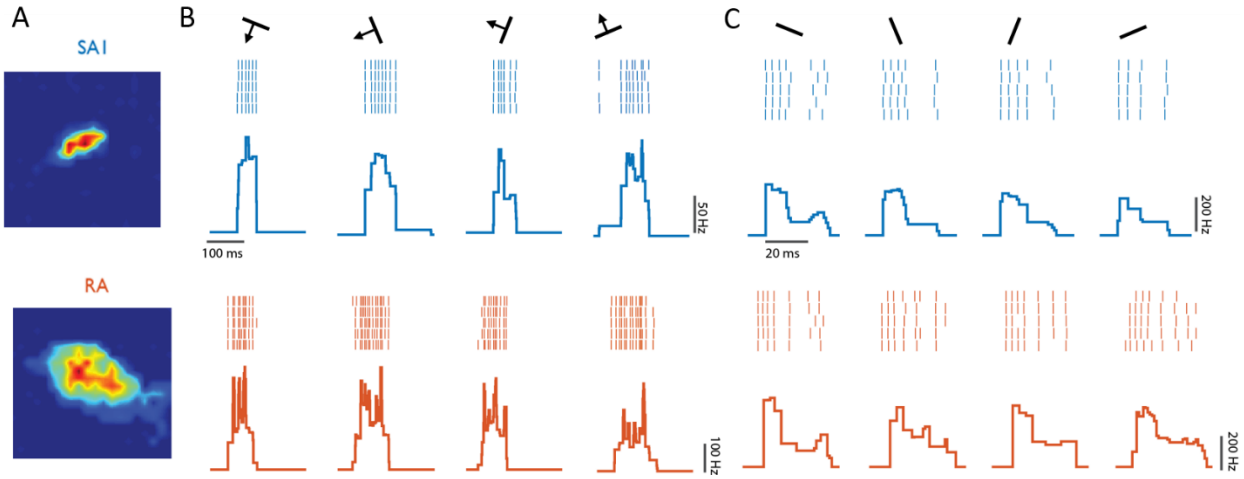

Figure 2.1 Responses to oriented edges.

A| RF map for a typical SA1 (top) and RA (bottom) afferent. B| Rasters of the response evoked in the two afferents shown in panel A by 5 repeated presentations of each of a subset of scanned edges and the corresponding peri-stimulus time histograms (SA1 in blue, RA in orange). C| Responses evoked by a subset of indented edges in the same two afferents. Firing rate profiles are consistent within but vary across orientations for both scanned and indented edges.

2.2.1| Edge orientation signals in afferent responses

Our first objective was to replicate the finding that the spiking responses of mechanoreceptive afferents carry information about the orientation of edges scanned across the skin in monkeys (Pruszynski and Johansson 2014). To this end, we attempted to classify the orientation of scanned edges based on the responses evoked in individual afferents using a nearest neighbor classifier, which gauges the degree to which the responses to edges at a given orientation are similar to each other and different from those at different orientations. The dissimilarity between spike trains was measured using spike

distance, which is the cost to transform one spike train into another (Victor and Purpura 1997). We performed the classification analysis at different temporal resolution to assess the degree to which precise spike timing conveys orientation information.

2.2.2| Scanned Edges

Edges at 8 orientations (ranging from 0 to 167.5° in 22.5° steps) and three indentation levels (100, 200, and 300 μm) were scanned across each afferent's RF in 2 directions, both perpendicular to the edge see Figure 2.1). First, we classified orientation based on the spiking responses evoked in a single direction for each orientation (at an amplitude of 300 μm), to match the stimulation paradigm used in the human microneurography study to the extent possible. That is, we split the data set in two, with each half containing afferent responses to each orientation in one of the two directions (each perpendicular to the edge's orientation). The classification analysis revealed that orientation could be resolved with high fidelity (>90%) at a temporal resolution of ~2 ms (Figure 2.2A-C) with both SA1 and RA responses (averaged across both scanning directions), consistent with results obtained with human tactile afferents (Pruszynski and Johansson 2014). However, as temporal resolution decreased, discriminability markedly declined and was near chance at the coarsest temporal resolution, consistent with earlier observations that firing rates are not tuned for orientation in the periphery (Bensmaia et al. 2008a). Furthermore, when we compared classification with the 300-μm edges to that with shallower edges, we found that higher stimulus amplitudes resulted in better direction classification for SA1 fibers but not

RA fibers, likely because SA1 fibers respond more strongly to higher-amplitude stimuli while RA fibers less so (Figure 2.2D) (Blake et al. 1997).

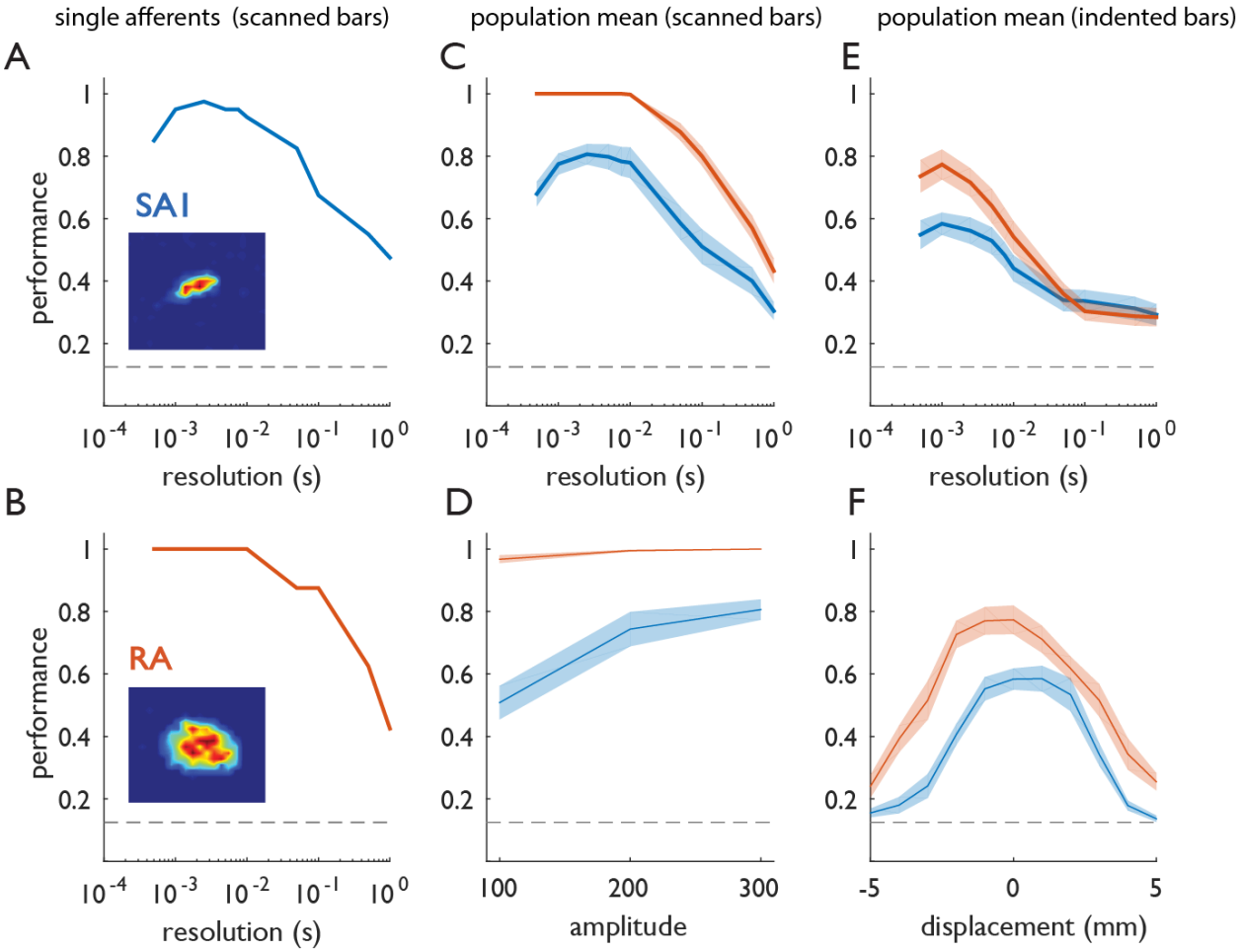

Figure 2.2 Afferent orientation signals for scanned and indented edges.

A| Classification performance based on the responses of an SA1 afferent to 300-μm scanned edges at 8 orientations as a function of the temporal resolution of the classifier ($1/q$). The leftmost extreme of the curve shows classification performance when sub-millisecond differences in spike timing are taken into consideration, the rightmost extreme of the curve shows classification performance based solely on spike counts over the stimulus interval. B| Classification performance based on the responses of an RA afferent. C| Mean classification performance based on the responses of 10 SA1 (blue) and 12 RA fibers (orange) to scanned edges. D| Peak classification performance at three amplitudes. E| Mean classification performance based on the responses of 8 SA1 and 10 RA fibers to indented edges. F| Peak classification performance at different locations relative to the hotspot (located at displacement = 0 mm). In this analysis, classification is performed at each location separately. As was found in humans, tactile fibers carry considerable information about edge orientation in the precise timing of their responses. Error shading denotes

Figure 2.2, continued. standard error of the mean. The horizontal dashed lines denote chance performance (0.125) given the 8 possible edge orientations.

Finally, RA afferents were found to encode orientation substantially better than SA1 afferents, especially at lower indentation levels. Differences in performance may be attributable in part to the larger RF size of RA afferents (SA1: 12.14 ± 3.38 mm^2 SD; RA: 24.32 ± 7.35 mm^2 SD), which allows for a more temporally extended response to the same scanned stimulus and thus for more opportunity for the time-varying responses to differ across stimuli. Overall, these results demonstrate that individual afferent firing patterns convey information about orientation in response to scanned edges (single direction) and do so in the precise timing of their spikes, replicating the result obtained with human tactile afferents (Pruszynski and Johansson 2014).

2.2.3| Predicting responses from RF topography

The orientation-specific spiking responses have been suggested to arise as a consequence of the sequential activation of spatially displaced receptors as the edge moves over each receptor in turn (Pruszynski and Johansson 2014). To test this hypothesis, we first investigated the degree to which a neuron's responses to scanned edges is shaped by the spatial arrangement of its transduction sites, replicating the model established in the human microneurography study (Pruszynski and Johansson 2014). To this end, we assessed

the degree to which the spiking responses to each edge could be predicted linearly from the RF topography (Figure 2.3A-B).

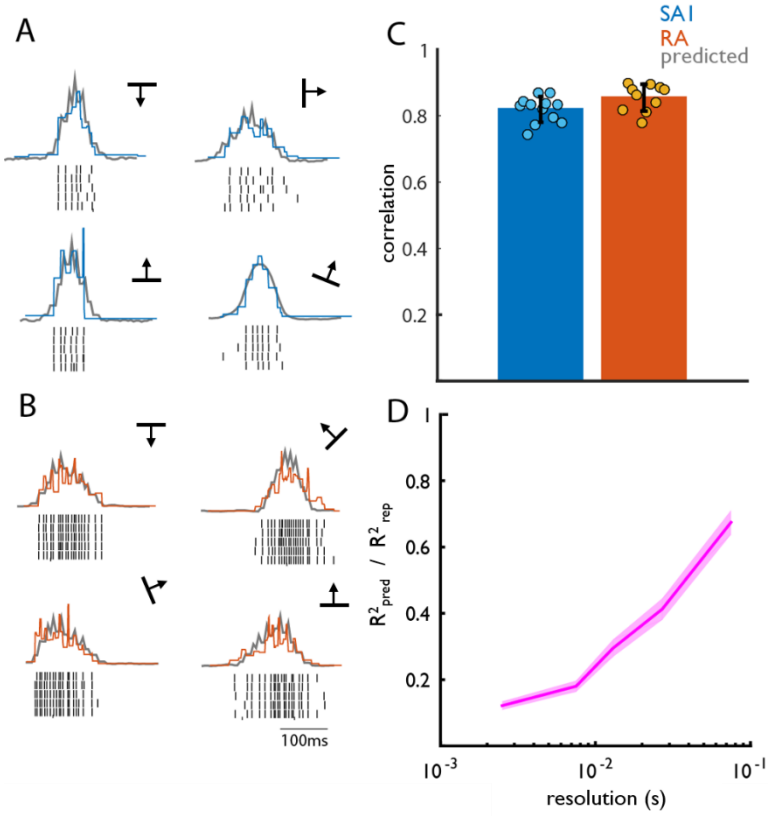

Figure 2.3 Predicting the firing rate profiles from RF topography.

A| Example of predicted (gray) and observed (blue) firing rate profiles for a single SA1 afferent. B| Example of predicted (gray) and observed (orange) firing rate profiles for a single RA afferent. Although observed and predicted firing patterns are highly correlated, predicted firing patterns capture the coarse structure of the firing profiles, but not their fine structure. C| Mean maximum cross correlation between predicted and observed firing rate profiles for SA1 and RA afferent populations. The error bar represents the standard error of the mean. D| Ratio of R^2 for predicted vs. observed (R^2_{pred}) to the R^2 for observed vs. observed (R^2_{rep}) across multiple temporal resolutions. Error shading denotes standard error of the mean. Predicted firing rate profiles closely match observed firing rate profiles at coarse but not fine temporal resolutions.

We found that the linear predictions matched the observed firing profiles, each in 1 ms bins, for both SA1 and RA afferents (Figure 2.3C) (r = 0.83 ± 0.04, mean ± s.d.), as was found with human afferents.

We then wished to determine the degree to which the predicted responses captured the fine temporal structure in their observed counterparts. To this end, we band-

passed filtered the predicted and observed responses within multiple frequency ranges: 333-500 Hz (2-3ms); 125-200Hz (5-8 ms); 66-100 Hz (10-15ms); 33-50Hz (20-33ms); 10-20Hz (50-100ms). Next, we cross-correlated the filtered predicted and observed responses within each frequency band. We also cross-correlated the filtered observed responses to repeated presentation of each stimulus amongst themselves to assess the degree to which responses were repeatable within each band. At the lower frequency ranges, and thus coarser temporal resolutions, the cross-correlations with the predictions became closer to the cross-correlations across repeats (Figure 2.3D). In other words, the coarse structure of the response is reflected in the linear prediction while its fine structure is not. Given that the orientation information is conveyed at a fine temporal resolution, it is likely that the spatial configuration of the RF is not sufficient to account for the orientation signals.

2.2.4| Indented Edges

To further test the sequential activation hypothesis, we investigated whether the spiking responses to indented edges carry orientation information even though the edge does not move relative to the RF. Each afferent was indented with edges at 8 different orientations, with the center of the edges positioned on the RF center or slightly shifted therefrom (by up to 5 mm in 1-mm steps in each direction, see Figure 2.5C). As with scanned edges, we

achieved high classification performance at fine temporal resolutions (~2 ms) (Figure 2.2E), even when the indented edge was presented at an offset from the center of the RF of up to ~2 mm in each direction (Figure 2.2F), as might be predicted from the measured RF size. This high level of classification performance is surprising given the short duration of the stimulus (30 ms).

In summary, then, individual afferents carry edge orientation information throughout their RF, even for indented edges, suggesting that the sequential contact with spatially displaced hotspots is not required for the genesis of precisely timed spiking patterns carrying orientation information.

2.2.5| Testing the robustness of orientation signals across conditions

A neural code for orientation would be robust to changes in other stimulus properties so that orientation information could be decoded by downstream structures regardless of the precise geometry of the edge or of its motion across the RF (or lack thereof). To the extent that orientation signals vary depending on other stimulus properties, decoding becomes more challenging and a biologically plausible decoder must be formulated. For example, orientation signals dilate or contract systematically with decreases or increases in scanning speed (Pruszynski and Johansson 2014). In principle, then, speed could be corrected for when decoding orientation. Here, we wished to characterize whether the temporal spiking sequences that signal orientation depend on other stimulus properties, including their amplitude, movement direction, and precise location on the RF. To this end, we attempted to classify the orientation of stimuli that also differed in other stimulus parameters based

on the evoked neuronal response. To the extent that the orientation signals were consistent across changes in other stimulus features, classification performance would be high.

First, we examined the effect of changes in indentation amplitude on classification performance. That is, we pooled responses to scanned edges at amplitudes of 100 and 300 μm, and assessed whether responses at 200 μm were more similar to their counterparts at 100 and 300 μm when the orientation was the same than when it was different. We found that classification was poor under these circumstances (Figure 2.4A), despite the fact that classification performance was high at each amplitude separately (Figure 2.2D). That is, we could classify orientation when the amplitude was held constant, but not when it varied. These results suggest that orientation signals are amplitude-dependent. Performance levels for amplitude pooled responses fell to 0.42 (SEM .018) for RA fibers, and to 0.13 (SEM .026) for SA1 fibers.

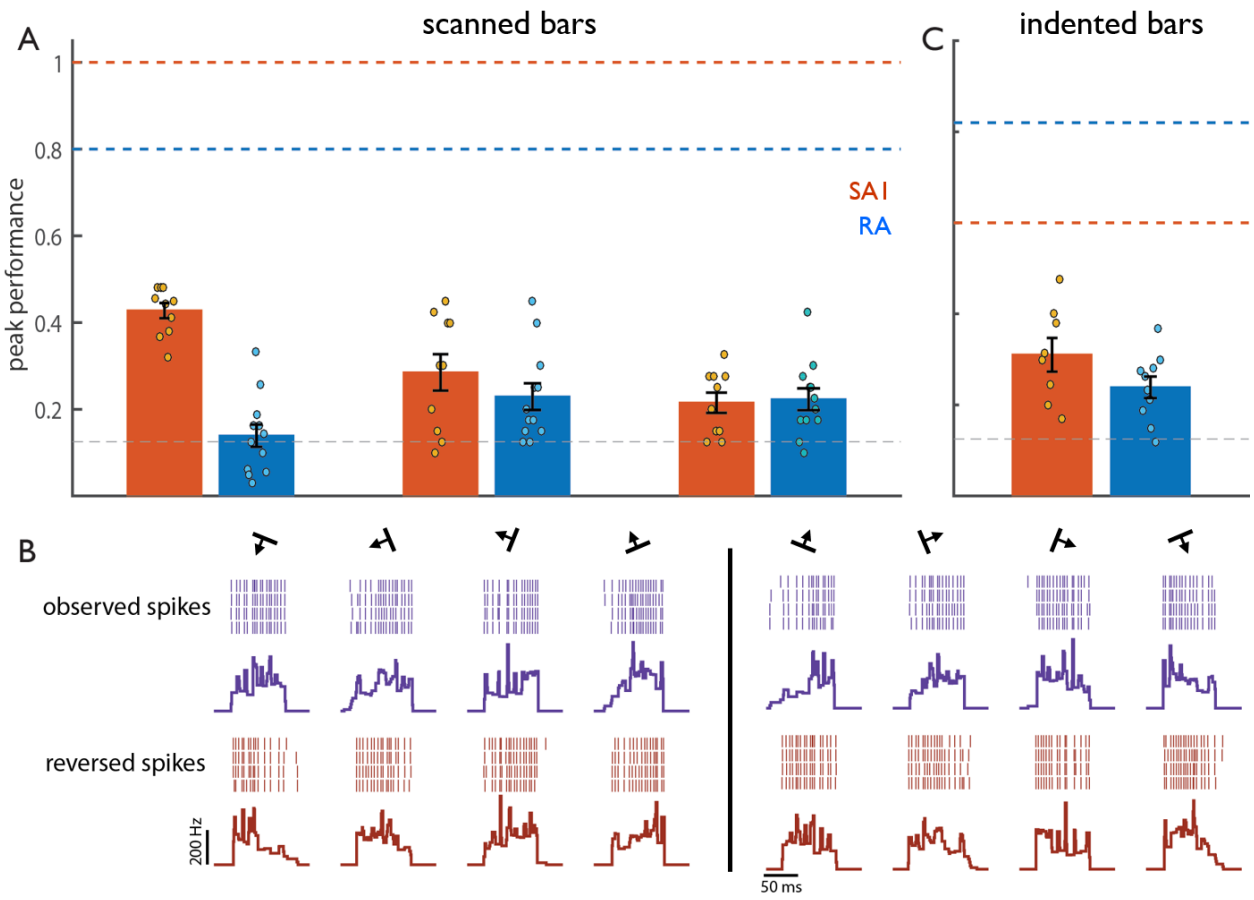

Figure 2.4. Robustness of orientation signals.

A| Performance of the orientation classifier for scanned edges when other stimulus parameters vary. Amplitude: Comparison of the responses at 100-μm and 300-μm to those at 200-μm. Direction: Comparison of the responses in one direction to those in the opposite direction. Direction (rev): Comparison of the responses in one direction to reversed responses in the opposite direction. Horizontal dashed lines (SA1 orange, RA blue) denote peak classification performance when all other stimulus features are constant while the gray dashed line denotes chance performance (0.125). B| Example of spike patterns evoked from a single RA afferent for one scanned direction (left, purple rasters and mean firing rate profiles) and the opposite scanned direction (right, purple rasters and mean firing rate profiles). Reversed spike trains and mean firing rate profiles of the corresponding opposite scanned direction are displayed in red (bottom). C| Classification performance for indented edges that vary in location. The horizontal dashed edges denote peak classification performance when the edge is centered on the hotspot (SA1 orange, RA blue), while chance level is denoted by the gray dashed line. Error bars represent standard error of the mean. Classification performance is substantially reduced when other stimulus features vary.

Second, we gauged the degree to which information about the orientation of a scanned edged was consistent across scanning directions. To this end, we computed the distance between spike trains evoked in one direction to those evoked in the opposite direction. We then used these spike distances to classify edge orientation, and found that performance fell to near chance levels: 0.29 (SEM .042) for RA fibers, and 0.23 (SEM .031) for SA1 fibers (Figure 2.4A). That is, the spiking response to a given orientation scanned in a given direction is no more similar to the response to the same orientation scanned in the opposite direction than it is to the response to a different orientation. Orientation signals are thus highly dependent on scanning direction. To the extent that orientation signals are determined by the sequential activation of receptors, we might expect that the spiking pattern in one direction might match the reversed spike pattern in the opposite direction. We tested this hypothesis by comparing the responses to one direction with the reversed responses to the opposite direction (Figure 2.4B). Again, we found that classification was poor: 0.22 (SEM .023) for RA fibers, and 0.22 (SEM .025) for SA1 fibers (Figure 2.4A), which constitutes further evidence that RF topography cannot fully account for the orientation information in afferent responses.

Third, we investigated the dependence of the orientation signals for indented edges on the precise location within the RF at which they were presented. To this end, we compared the responses evoked by edges offset by 1 mm from the RF center to those evoked by edges delivered at the RF center. We chose this range of offsets because our initial analysis revealed that orientation discriminability remained relatively constant over this range, when classification was performed at each location separately (Figure 2.2F). Again, we

found that classification was poor, indicating that spiking patterns depend critically on the location of the stimulus within the RF (Figure 2.4C).

In conclusion, then, spike patterns evoked in the nerve depend not only on orientation but also on other stimulus features. In fact, the responses evoked by edges at the same orientation that differ in other ways are no more similar to each other than they are to responses to edges at different orientations. The strong susceptibility of single afferent responses to influence from all stimulus features makes the decoding of orientation from these responses challenging.

2.3| Discussion

2.3.1| Explicit signaling of edge orientation by mechanoreceptive afferents

We aimed to address the following three questions: 1) Do mechanoreceptive afferents of non-human primates carry edge orientation signals as do those of humans? 2) Can firing rate patterns be predicted from RF topography? 3) How robust are these edge orientation signals when other stimulus features vary?

First, our findings suggest that afferents in human and non-human primates respond similarly to scanned edges. Indeed, our analyses of data analogous to those from the previous human microneurography study (Pruszynski and Johansson 2014) – namely afferent responses to edges scanned in a single direction – yield results that are virtually identical, despite differences in the stimuli. Indeed, the stimuli used in the present study consisted of pins sequentially indented in the skin rather than scanned embossed edges. One minor difference between human and non-human afferents is that, in monkeys, RA fibers seem to signal orientation better than do their SA1 counterparts, a discrepancy

that can be attributed to differences in RF size. Indeed, some SA1 afferents in monkeys have such tiny RFs that there is little opportunity for temporal modulation as the edge is scanned across the RF (see also (Sripati et al. 2006)). Such an effect might not be observed in humans because RA and SA1 receptive fields are more comparable to each other in size (Johansson 1978; Vallbo and Johansson 1984).

Second, we showed that, while the coarse temporal structure of afferent responses could be linearly predicted from the RF topography, the fine temporal structure could not. Since edge orientation signals rely on spiking patterns at the millisecond timescale, the fine spatial structure of afferent RFs topography is not sufficient to account for the resulting orientation information.

Finally, we explored the dependence of orientation signals on other stimulus features by testing the ability of classifiers to generalize across stimulus conditions. In the human microneurography study, afferent responses to scanned edges remained consistent across speeds, and were consistently warped in time depending on the speed (Pruszynski and Johansson 2014). Here, we aimed to explore the effect of other stimulus parameters, including those whose impact on cortical orientation signals and on human perception has been shown to be minimal (Bensmaia et al. 2008a, 2008b). We found that slight changes in the location at which the stimulus was delivered abolished the ability to classify its orientation, as did changes in amplitude or scanning direction. Given their dependence on other stimulus features, then, orientation signals can only be decoded in a context-dependent manner. In light of this, it is critical to articulate a biologically plausible decoder that could make use of these signals. Indeed, questions remain as to their role in perception

or in motor control. Regarding the perceptual coding of orientation, one might ask whether these temporal orientation signals contribute to the robust rate-based orientation signals observed in S1, or complement them in some way. In motor control, information about the presence and orientation of edges would support the dexterous manipulation of objects. How such a susceptible signal might drive subtle adjustments of hand posture during object interactions has yet to be clearly articulated.

2.3.2| Stimulus coding in tactile afferents

Cutaneous mechanoreceptive afferents produce spiking responses that are (1) remarkably repeatable, with precision down to the sub-millisecond time scale (Johansson and Birznieks 2004; Mackevicius et al. 2012; Bale et al. 2015) and (2) exquisitely sensitive to skin stimulation. In other words, tactile fibers produce responses that are virtually identical when the same stimulus is presented repeatedly, and different when different stimuli are presented, even if these stimulus differences are very subtle (Goodwin and Morley 1987; Khalsa et al. 1998; Khamis et al. 2015). As a result, the information about stimulus identity in afferent responses is off the charts if spike timing is taken into consideration, particularly with good stimulus control that allows for precise repeated presentation of the same stimulus (Maia Chagas et al. 2013). In other words, almost any pair of non-identical stimuli can be distinguished based on the spiking patterns they evoke in mechanoreceptive afferents. The key to understanding neural coding in the nerve, then, is to identify how different aspects of the afferent response systematically encode different aspects of the stimulus in such a way that these aspects can be decoded by downstream structures.

There are several ways to establish a neural code. One way is to demonstrate that information about a stimulus quantity, known to be accessible perceptually, is only carried in a given aspect of the neuronal response (Jacobs et al. 2009). For example, we have shown that the frequency composition of a skin vibration is encoded in the timing of the responses and that it cannot be decoded from their rates (Mackevicius et al. 2012). Similarly, information about fine textures is only carried in the temporal spiking patterns evoked in RA and PC fibers (Weber et al. 2013). Another way is to demonstrate that an aspect of the neural response covaries with a stimulus property in the same way as does the corresponding perceptual dimension (Johnson et al. 2002). For example, we have shown that, while several aspects of afferent responses change when the stimulus amplitude increases (firing rate, size of the activated population, etc.), one of these covaries more strongly than the others with the perceived magnitude of the stimulus (population firing rate weighted by afferent type), which strongly bolsters its claim as the neural code for intensity (Muniak et al. 2007). The third and probably most powerful way to confirm a neural code is to test it causally by artificially inducing a pattern of neuronal activation (through electrical or optogenetic stimulation, e.g.), and assessing whether it results in the predicted perceptual consequence. In a recent study, we confirmed the intensity coding hypothesis mentioned above by showing that it accounted for the perceived magnitude of electrically induced activation of the peripheral nerve (Graczyk, E. et al. 2016)

The remarkable sensitivity and precision of afferents presents a unique challenge in understanding how they encode stimulus information. There is little question that spike timing carries stimulus information and is behaviorally relevant (Saal et al. 2016). The

orientation of edges impinging on the skin can theoretically be decoded from the temporal spiking patterns evoked tactile fibers. The challenge will be to determine if and how this is accomplished given the volatility of these signals.

2.4| Methods

2.4.1| Neurophysiology

All experimental protocols complied with the guidelines of The Johns Hopkins University Animal Care and Use Committee and the National Institutes of Health's Guide for the Care and Use of Laboratory Animals. We recorded single units from the median and ulnar nerves of four anaesthetized macaque monkeys using standard methods (Mountcastle et al. 1967; Talbot et al. 1968) as previously described in detail (Bensmaia et al. 2008a). Each animal contributed up to eight recording sessions – upper and lower sites on median and ulnar nerve – separated by two or more weeks. Briefly, the forearm and hand were fixed by a clamp, and the ulnar or median nerve was exposed in the upper or lower arm. Next, a skin flap pool was formed, and a small bundle of axons was separated from the nerve trunk and wrapped around a silver electrode.

An afferent was classified as SA1 if it had a small RF and produced a sustained firing response to a skin indentation, as RA if it had a small RF and responded only at the onset and offset of an indentation, and as Pacinian (PC) if it had a large, diffuse RF and was activated by air blown gently over the hand. The point of maximum sensitivity (hotspot) was located using a handheld probe and the stimulus was centered on the hotspot. We only recorded the responses of RA and SA1 afferents with RFs located on the distal fingerpad of

digits 2 through 5 (PC fibers were not included for analysis as their RF properties are ill suited to encode the spatial properties of isolated spatial features).

2.4.2| Stimuli

Stimulator

Stimuli were delivered using a dense array tactile stimulator consisting of 400 probes arrayed in a 20 by 20 grid spanning 1 cm x 1 cm (Killebrew et al. 2007) (Figure 2.5A). Each probe was driven along the axis perpendicular to the skin's surface by a dedicated motor, under

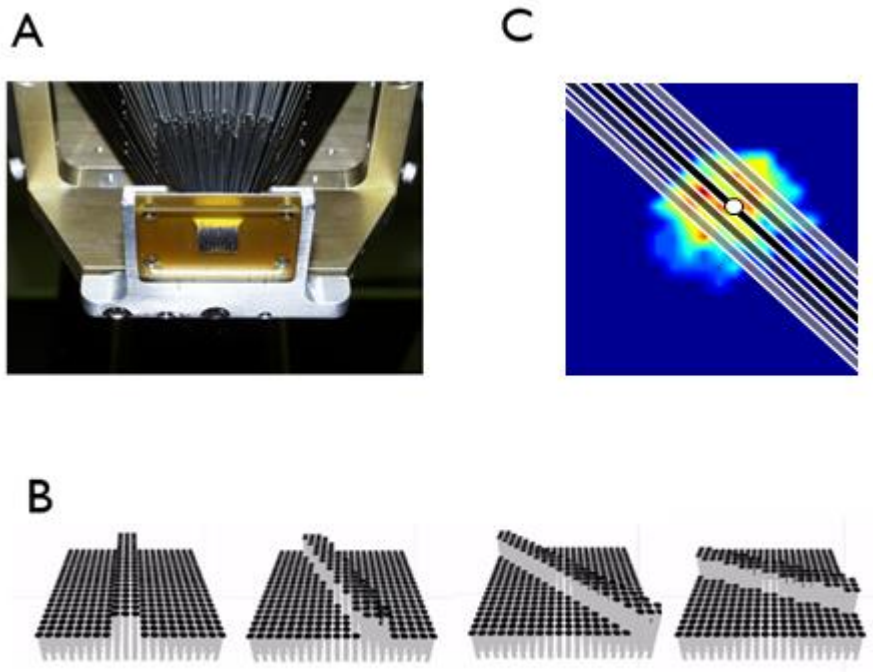

Figure 2.5 Experimental set up.

A| Bottom view of the 400-probe stimulator (Killebrew et al. 2007). Individual pins converge onto a 1 cm^2 area over the skin. B| Sequence of snapshots depicting an edge at different edge orientations. Note that pins are close enough together that the pixilation of the array is not felt. C| Location of indented edges with respect to the receptive field. The heat map shows the RF topography overlaid with edges at orientation 130°. The black edge is centered on the hotspot, the dark and light gray edges are displaced by ±1 mm and ±2 mm respectively. The hotspot is indicated by the white circle.

independent computer control. The stimulator is the tactile equivalent of a video monitor, endowing the experimenter with the ability to activate each pin independently to create arbitrary spatiotemporal patterns over an area of 1 cm^2. Edges were two pins (1 mm) wide and always extended beyond the afferent RF. Scanned edges were generated by sequentially activating neighboring pins on the array.

Single probe indentations

This stimulation protocol was used to characterize the receptive field topography. On each trial, a probe was indented into the skin for 100 ms at an amplitude of 300 μm with an inter-stimulus interval of 100 ms. Consecutively indented probes were not adjacent to reduce confounding effects of skin mechanics (Pawluk and Howe 1997; Pawluk et al. 1998). To reconstruct each afferent's RF, we computed the mean of five responses to each of the 400 pins. The point of maximum sensitivity was selected as the hotspot.

Scanned edges

This protocol most closely matched that used in the previous study investigating orientation signals in the nerve (Pruszynski and Johansson 2014). On each trial, an edge was scanned across the fingertip in one of 16 directions, ranging from 0 to 337.5° in 22.5° steps (Figure 2.1, 0° corresponds to rightward motion) and one of three indentation depths (100, 200, and 300 μm). Each direction and amplitude pair was presented five times in pseudorandom order, yielding a total of 240 trials. The scanning speed was 40 mm/s, and the inter-stimulus interval was 200 ms. The edge was always scanned in a direction

perpendicular to its orientation to avoid the confounds of length and effective speed that are faced when all edges are scanned in the same direction.

Indented edges

We wished to extend the results from the original study by examining whether afferent responses to indented edges also conveyed information about their orientation. Indeed, to the extent that orientation signals are dependent on the sequential activation of multiple spatially displaced receptors innervated by a given afferent, responses to indented edges will not carry orientation information. On each trial, an edge was indented into the skin at one of 8 orientations, ranging from 0 to 157° in 22.5° steps (with 0° degrees corresponding to the long axis of the finger). The indentation depth of the edge was always 500 μm, and its duration 30 ms. The edge was either indented in the center of the RF (determined from the RF map derived from the single probe indentations), or it was displaced by 1 to 5 mm along the axis normal to the orientation of the edge (for a total of 11 different locations at each orientation, Figure 2.5C). Edges were each presented 10 times at each orientation and location for a total of 880 trials.

2.4.3| Data Analysis

Metric space analysis for orientation classification

To assess the degree to which information about orientation is carried in the spiking responses of individual afferents, we implemented a classification analysis. Specifically, we wished to determine whether we could classify stimuli that differed in orientation based on the responses they evoked in individual afferents. We used a nearest neighbor classifier, which gauges whether spike trains evoked by a class of stimuli (edges at a specific

orientation in this case) are more similar to each other than to those evoked by other classes of stimuli (edges at different orientations). We implemented a leave-one-out approach, in which we computed the distance between each spike train, S_i, and every other spike train. The orientation was correctly classified when the mean distance between S_i and spike trains from the same orientation was lower than the mean distance between S_i and spike trains from each of the other orientations. This procedure was repeated for every spike train obtained from each afferent. We used spike distance as a measure of dissimilarity between two spike trains (Victor and Purpura 1996), as we have previously done (Mackevicius et al. 2012; Weber et al. 2013). In brief, spike distance is the smallest possible cost of transforming one spike train into another: There is a cost (of 1) associated with adding and deleting spikes, and a cost per unit time, q, associated with moving spikes. A benefit of this analysis is that, by varying the parameter q, we can manipulate the contribution of precise spike timing to the distance computation and thus to the classification analysis. If q is 0, then the distance amounts to computing the difference in spike count. As q increases, it becomes less and less advantageous to move spikes around rather than to add and subtract them, and so small differences in the timing of individual spikes increasingly determines spike distance. We modified this analysis by computing the pairwise spike distance between temporally shifted spike trains (shifted by 1ms increments, up to 100ms) and using the minimum distance across all shifts to ensure that classification did not exploit differences in absolute response latency, which is largely determined by the precise location of the RF relative to the stimulus. Using spike distance with different values of q is analogous to taking the cross correlation between spike trains convolved with filters at different widths

(Pruszynski and Johansson 2014) but the temporal precision is more clearly defined with spike distance than for filtered spike trains and we found classification performance to be consistently higher with the former than with the latter (data not shown).

Prediction of firing rates based on receptive field topography

To determine whether the profile of afferent responses to edges could be predicted based on RF topography, we convolved each afferent's RF with each time-varying stimulus pattern. For this analysis, we interpolated the RF map and stimulus pattern to achieve a temporal resolution of 2.5 ms in our response predictions. Model performance was quantified by cross correlating predicted firing profiles and the mean instantaneous firing profiles for each scanning direction. We could then compare the linear prediction to the measured response profile for each afferent and stimulus (Pruszynski and Johansson 2014).

To assess the temporal resolution at which predicted responses matched observed responses, we measured the cross-correlation of predicted and observed responses after filtering the responses in different frequency bands: High-frequency bands tested the ability of the linear model to predict precise spike timing; low-frequency bands tested its ability to reconstruct the slow waxing and waning of the responses. We used a 6^{th} order bandpass Butterworth filter across the following frequency ranges: 333-500 Hz (2-3ms); 125-200Hz (5-8 ms); 66-100 Hz (10-15ms); 33-50Hz (20-33ms); 10-20Hz (50-100ms). We then cross-correlated band-passed predicted responses with band-passed observed responses within each frequency range. This way, we could determine which frequency band, or temporal resolution, yielded the highest correlation. We also computed the cross-

correlation of observed responses to repeated presentations of each stimulus at the different frequency bands to establish the repeatability of the response within each band and thus the best possible performance for any model. We then assessed how close the predictions were to the best possible performance by calculating the ratio between the mean R^2 value for predicted vs. observed and that for observed vs. observed within each frequency range.

2.5| References

Augurelle A-S, Smith AM, Lejeune T, Thonnard J-L. Importance of cutaneous feedback in maintaining a secure grip during manipulation of hand-held objects. J Neurophysiol 89: 665–671, 2003.

Bale MR, Campagner D, Erskine A, Petersen RS. Microsecond-Scale Timing Precision in Rodent Trigeminal Primary Afferents. J Neurosci 35: 5935–5940, 2015.

Bensmaia SJ, Denchev P V, Dammann JF, Craig JC, Hsiao SS. The representation of stimulus orientation in the early stages of somatosensory processing. J Neurosci 28: 776–786, 2008a.

Bensmaia SJ, Hsiao SS, Denchev P V, Killebrew JH, Craig JC. The tactile perception of stimulus orientation. Somatosens Mot Res 25: 49–59, 2008b.

Blake DT, Hsiao SS, Johnson KO. Neural coding mechanisms in tactile pattern recognition: the relative contributions of slowly and rapidly adapting mechanoreceptors to perceived roughness. J Neurosci 17: 7480–9, 1997.

Cauna N. Nerve supply and nerve endings in Meissner's corpuscles. Am J Anat 99: 315–350, 1956.

Goodwin AW, Morley JW. Sinusoidal movement of a grating across the monkey's fingerpad: effect of contact angle and force of the grating on afferent fiber responses. J Neurosci 7: 2192–202, 1987.

Graczyk, E.; Schiefer, M.; Delhaye, B.; Saal, H.; Bensmaia, S.; Tyler D. The Role of Sensory Adaptation in Artificial Tactile Intensity. In: Neural Interfaces Conference. 2016.

Hubel DH, Wiesel TN. Receptive fields, binocular interaction and functional architecture in the cat's visual cortex. J Physiol 160: 106–154, 1962.

Jacobs AL, Fridman G, Douglas RM, Alam NM, Latham PE, Prusky GT, Nirenberg S. Ruling out and ruling in neural codes. P Natl Acad Sci Usa 106: 5936–5941, 2009.

Johansson RS, Birznieks I. First spikes in ensembles of human tactile afferents code complex spatial fingertip events. Nat Neurosci 7: 170–177, 2004.

Johansson RS, Flanagan JR. Coding and use of tactile signals from the fingertips in object manipulation tasks. Nat Rev Neurosci 10: 345–359, 2009.

Johansson RS. Tactile sensibility in the human hand: receptive field characteristics of mechanoreceptive units in the glabrous skin area. J Physiol 281: 101, 1978.

Johnson KO, Hsiao SS, Yoshioka T. Neural Coding and the Basic Law of Psychophysics. Neuroscientist 8: 111–121, 2002.

Khalsa PS, Friedman RM, Srinivasan MA, Lamotte RH. Encoding of shape and orientation of objects indented into the monkey fingerpad by populations of slowly and rapidly adapting mechanoreceptors. J Neurophysiol 79: 3238–51, 1998.

Khamis H, Birznieks I, Redmond SJ. Decoding tactile afferent activity to obtain an estimate of instantaneous force and torque applied to the fingerpad. J Neurophysiol 114: 474–84, 2015.

Killebrew JH, Bensmaia SJ, Dammann JF, Denchev P, Hsiao SS, Craig JC, Johnson KO. A dense array stimulator to generate arbitrary spatio-temporal tactile stimuli. J Neurosci Methods 161: 62–74, 2007.

Mackevicius EL, Best MD, Saal HP, Bensmaia SJ. Millisecond precision spike timing shapes tactile perception. J Neurosci 32: 15309–15317, 2012.

Maia Chagas A, Theis L, Sengupta B, Stüttgen MC, Bethge M, Schwarz C. Functional analysis of ultra high information rates conveyed by rat vibrissal primary afferents. Front Neural Circuits 7: 190, 2013.

Mountcastle VB, Talbot WH, Darian-Smith I, Kornhuber HH. Neural basis of the sense of flutter-vibration. Science. 155: 597–600, 1967.

Muniak MA, Ray S, Hsiao SS, Dammann JF, Bensmaia SJ. The neural coding of stimulus intensity: linking the population response of mechanoreceptive afferents with psychophysical behavior. J Neurosci 27: 11687–11699, 2007.

Pack CC, Bensmaia SJ. Seeing and Feeling Motion: Canonical Computations in Vision and Touch. PLOS Biol 13: e1002271, 2015.

Paré M, Smith AM, Rice FL. Distribution and terminal arborizations of cutaneous mechanoreceptors in the glabrous finger pads of the monkey. J Comp Neurol 445: 347–359, 2002.

Pawluk D, Howe R. A holistic model of human touch. Comput. Neurosci. 1997.

Pawluk D, Son J, Wellman P. A distributed pressure sensor for biomechanical measurements. J BIOMECH ENG. 1998.

Priebe NJ, Ferster D. Mechanisms of Neuronal Computation in Mammalian Visual Cortex. Neuron 75: 194–208, 2012.

Pruszynski JA, Johansson RS. Edge-orientation processing in first-order tactile neurons. Nat Neurosci 17: 1404–1409, 2014.

Saal HP, Wang X, Bensmaia SJ. Importance of spike timing in touch: an analogy with hearing? Curr Opin Neurobiol 40: 142–149, 2016.

Scholl B, Tan AYY, Corey J, Priebe NJ. Emergence of Orientation Selectivity in the Mammalian Visual Pathway. J Neurosci 33: 10616–10624, 2013.

Sripati AP, Yoshioka T, Denchev P V, Hsiao SS, Johnson KO. Spatiotemporal receptive fields of peripheral afferents and cortical area 3b and 1 neurons in the primate somatosensory system. J Neurosci 26: 2101–2114, 2006.

2.4Talbot WH, Darian-Smith I, Kornhuber HH, Mountcastle VB. The sense of flutter-vibration: comparison of the human capacity with response patterns of mechanoreceptive afferents from the monkey hand. J Neurophysiol 31: 301–34, 1968.

Vallbo AB, Johansson RS. Properties of cutaneous mechanoreceptors in the human hand related to touch sensation. Hum Neurobiol 3: 3–14, 1984.

Victor JD, Purpura KP. Nature and precision of temporal coding in visual cortex: a metric-space analysis. J Neurophysiol 76: 1310–1326, 1996.

Victor JD, Purpura KP. Metric-space analysis of spike trains: Theory, algorithms and application. Network-Comp Neural 8: 127–164, 1997.

Warren S, Hamalainen HA, Gardner EP. Objective Classification of Motion-and Direction-Sensitive Neurons in Primary Somatosensory Cortex of Awake Monkeys. Journal of Neurophysiol 56, 1986.

Weber AI, Saal HP, Lieber JD, Cheng J-WW, Manfredi LR, Dammann JF, Bensmaia SJ, Dammann 3rd JF, Bensmaia SJ. Spatial and temporal codes mediate the tactile perception of natural textures. Proc Natl Acad Sci U S A 110: 17107–12, 2013.

Witney AG, Wing A, Thonnard J-L, Smith AM. The cutaneous contribution to adaptive precision grip. Trends Neurosci 27: 637–643, 2004.

Chapter 3 | The Effect of Contact Force on the Responses of Tactile Nerve Fibers to Scanned Textures[2]

The perception of fine textures relies on highly precise and repeatable spiking patterns evoked in tactile afferents. These patterns have been shown to depend not only on the surface microstructure and material but also on the speed at which it moves across the skin. Interestingly, the perception of texture is independent of scanning speed, implying the existence of downstream neural mechanisms that correct for scanning speed in interpreting texture signals from the periphery. What force is applied during texture exploration also has negligible effects on how the surface is perceived, but the consequences of changes in contact force on the neural responses to texture have not been described. In the present study, we measure the signals evoked in tactile afferents of macaques to a diverse set of textures scanned across the skin at two different contact forces and find that responses are largely independent of contact force over the range tested. We conclude that the force invariance of texture perception reflects the force independence of texture representations in the nerve.

[2] This chapter was published : Saal, H.P., Suresh, A.K., Solorzano, L.E., Weber, A.I., and Bensmaia, S.J. (2017). The effect of contact force on the responses of tactile nerve fibers to scanned textures. Neuroscience.

3.1| Introduction

Scanning a texture with our fingertip elicits highly precise and repeatable temporal spiking patterns in tactile afferents, and these spike sequences carry information about texture identity (Weber et al., 2013). Temporal spiking patterns mediate our ability to distinguish fine surfaces with different fine microstructure, measured in the tens of microns (Skedung et al., 2013; Weber et al., 2013; Manfredi et al., 2014). Spiking patterns do not simply depend on the textured surface, however; they also depend on the speed at which it moves across the skin: patterns contract and dilate with increases and decreases in scanning speed, respectively (Weber et al., 2013).

While natural texture exploration involves scanning movements that vary widely in speed and in contact force (Morley et al., 1983; Smith et al., 2002a, 2002b; Tanaka et al., 2014; Callier et al., 2015), our perception of texture depends little on these scanning movements: Velvet feels like velvet and sandpaper like sandpaper no matter how we touch them, suggesting that some aspect of the evoked response is invariant with respect to scanning parameters. For example, changes in scanning speed do not affect roughness perception (Lederman, 1974; Meftah el-M et al., 2000), despite its powerful influence on texture responses in tactile afferents (Weber et al., 2013). Similarly, the perceived roughness of textured surfaces is relatively insensitive to huge changes in contact force (Lederman and Taylor, 1972; Lederman, 1981): a five-fold increase in force only leads to a 10% increase in perceived roughness.

In the present study, we examine the degree to which texture-specific spiking sequences evoked during texture scanning depend on contact force. We find that, while firing rates

increase slightly at higher forces, the precise temporal patterning is almost completely unaffected and remains highly informative about texture identity across contact forces. Thus, while speed invariance of texture perception likely relies on specialized neural circuits (Saal et al., 2016), force invariance of perception simply reflects the force-independence of texture representations in the nerve.

3.2 | Results

We assessed how much varying the level of normal force exerted by the drum during texture scanning affected the neural responses of the three different afferent types implicated in texture perception: slowly-adapting type I (SA1), rapidly-adapting (RA), and Pacinian (PC) afferents (see Figure 3.1 for examples of neural responses recorded at different force levels). Data were obtained both through single-unit recordings from the peripheral nerve (SA1 and PC fibers) and array recordings from the dorsal root ganglia (RA fibers, see Methods for details).

Figure 3.1 | Texture Spike Trains

Figure 3.1, continued. Sample spike trains evoked in one afferent of each type by three different textures at two different contact forces. Visual inspection suggests that both the strength and temporal patterning in the response are relatively consistent across contact force conditions. These afferent responses were collected from the nerves.

3.2.1 Effects of force on firing rates

First, we examined the influence of contact force on the firing rates elicited in the three different afferent populations (Figure 3.2). We found that doubling the force (from 25 to 50 g wt) results in an increase in firing rate of 30% for SA1 fibers and 24% for PC fibers. RA afferents are even less susceptible to changes in force, as evidenced by the fact that a fivefold increase in force (from 10 to 50 g wt) resulted in a 16% increase in firing rate.

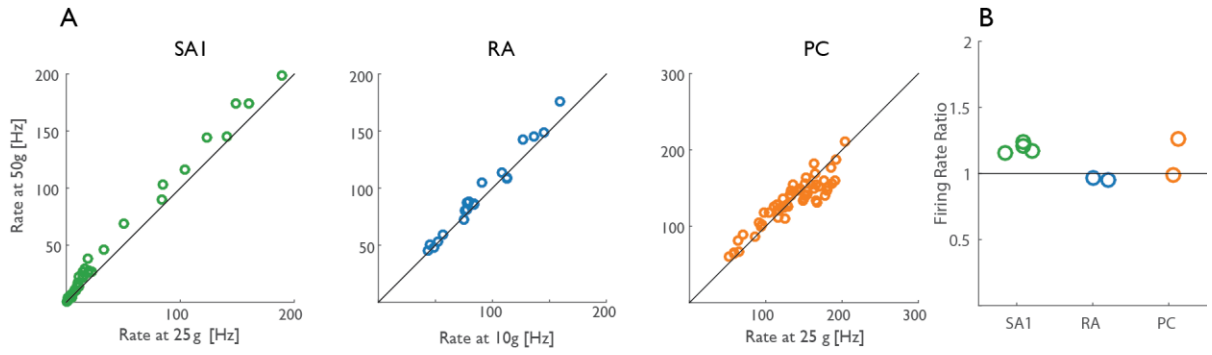

Figure 3.2. Firing Rate Responses to Force Variation

A| Mean firing rate evoked in three individual afferents at a high force (50 g) versus that evoked at a low one (25 g or 10g). **B|** Ratio of the firing rate evoked at a high contact force to that evoked at a low one, averaged across textures, for the three different afferent classes.

3.2.2 Effects of force on precise spike timing

Next, we examined whether the precise spiking sequences evoked during texture scanning were different at different levels of contact force. To test the robustness of the texture signals conveyed through temporal spiking patterns, we classified texture identity from the neural responses at different temporal resolutions. To the extent that temporal spiking sequences evoked by a given texture were consistently more similar to each other across contact forces than they were to patterns evoked by other textures, then texture identity

could be decoded from these patterns by downstream structures, regardless of contact force. The analysis also allows us to determine the optimal temporal resolution to extract texture information.

First, we tested spike sequences at each force level individually and found that classification performance was consistently well above chance at both force levels for all three afferent types (Figure 3.3, blue and orange traces). Note that classification performance is poor with rates alone and that the optimal resolution is highest for PC responses, lowest for SA1 responses, and intermediate for RA responses, as has been previously shown (Weber et al., 2013).

Second, we gauged whether spiking sequences were sufficiently similar across force levels to support texture classification. We found that, indeed, classification performance achieved by comparing neural responses evoked at high contact force (50g) to those collected at a low one (25 g or 10 g) was also far above chance for each class of nerve fibers at their optimal temporal resolution, albeit lower than that achieved at each level separately (Figure 3.3, yellow traces). This was also true for the finest textures, the perception of which relies exclusively on these temporal patterns. Indeed, classification performance for the four smoothest textures – chiffon, denim, silk, and upholstery – was 71, 66, and 63% for SA1, RA, and PC fibers, respectively, so performance was better than chance (25%) for those too. In conclusion, then, texture-specific temporal spiking patterns are preserved across changes in force level.

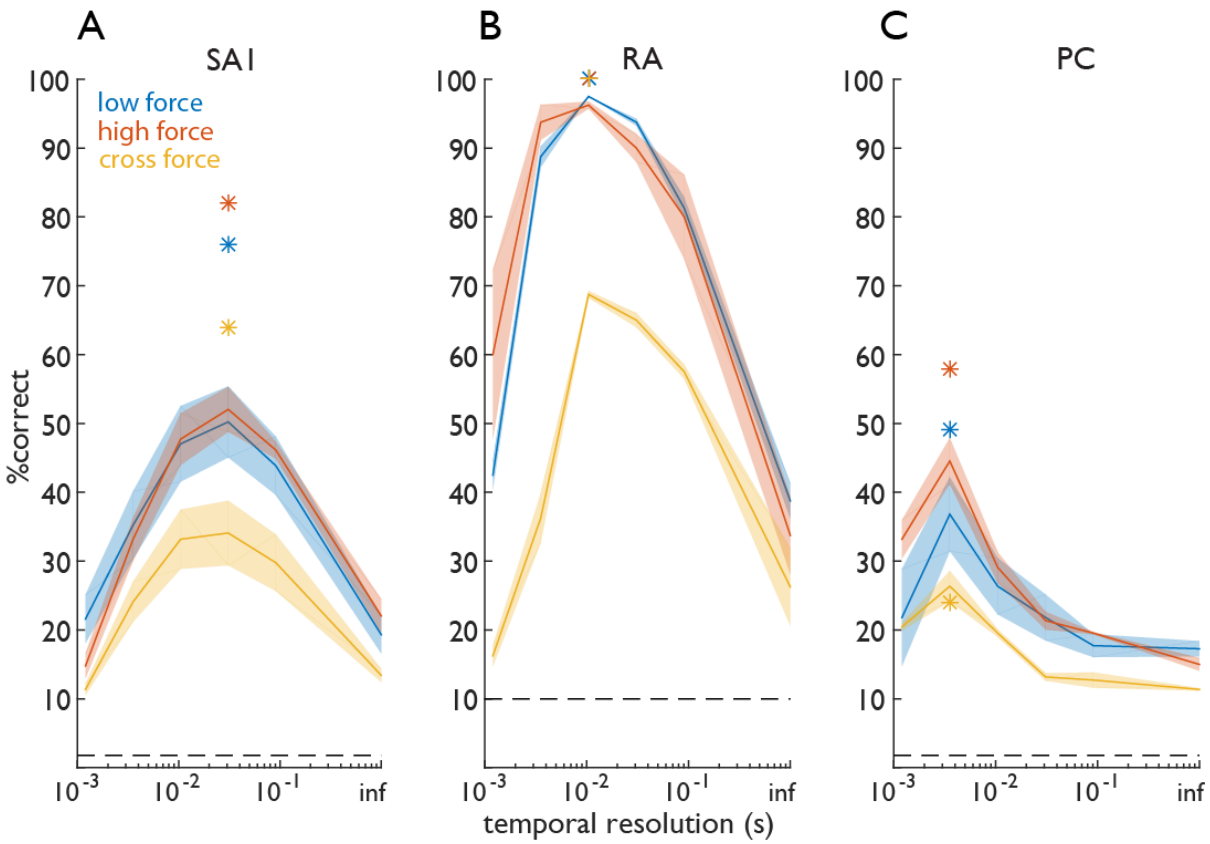

Figure 3.3 Texture Classification with Force Variation

A| Percentage of correctly classified textures at different temporal resolutions for SA1 (A), RA (B), and PC (C) afferents within force condition (blue and red) or across force conditions (yellow). Asterisks represent performance of a small sample of nerve fibers at their peak temporal resolution (n=4, 2, and 2 for SA1, RA, and PC fibers, respectively).

Next, we found that combining responses from a few fibers (4 SA1, 2 RA, and 2 PC fibers), yielded improved classification (except for PC fibers, asterisks in Figure 3.3), suggesting that a complete afferent population, comprising hundreds of nerve fibers, could convey texture information that is robust across contact forces.

3.3 | Discussion

Our ability to discern fine textures is thought to be mediated by the elicitation of precise temporal spiking sequences in somatosensory afferents as the fingertip moves across the surface (Bensmaïa and Hollins, 2003; Weber et al., 2013). For this neural code to be viable,

however, these patterns have to remain consistent when the movements used to explore the surface change, or vary systematically. Indeed, both scanning speed and contact force vary widely during the natural exploration of textures (Smith et al., 2002b; Callier et al., 2015). If the texture signals from the hand changed in unpredictable ways with changes in scanning parameters, these signals would be impossible to interpret. Instead, our perception of texture is mostly independent of exploratory parameters (Lederman, 1974) (but see Cascio and Sathian, 2001), suggesting that some aspect of these spiking sequences is consistent across changes in scanning speed and contact force.

In previous work, we have shown that changes in scanning speed lead to systematic changes in the neural responses: the spiking patterns dilate and contract as scanning speed decreases or increases, respectively (Weber et al., 2013). Here, we found that the temporal structure of the spiking sequences is relatively consistent across contact force levels so that textures can be reliably classified across different force conditions when spike timing is taken into account. In other words, the neural code for texture is robust across changes in contact force.

Note that the sample size in the present study is small, particularly for RA and PC afferents. The experimental protocol in which we probed the effects of contact force on afferent responses was one of several, and we were often unable to maintain stable recordings from a nerve fiber to run that particular protocol. However, SA1 afferents are the most sensitive to changes in contact force (Knibestöl, 1975) and the other two classes of afferents respond primarily to changes in indentation rather than absolute levels of indentation (Knibestöl, 1973; Johansson and Vallbo, 1983). We might thus expect the texture signals carried by SA1

fibers to be most sensitive to changes in contact force, and they are not. In fact, SA1 responses have been shown to respond to surface elements that create local deformations within the fingertip in a way that is relatively independent of the overall force exerted on the skin (Vega-Bermudez and Johnson, 1999), consistent with the present findings. Thus, the preservation of spiking sequences across force levels is not only consistent across fiber types, but also observed in the fiber type that should be most sensitive and has the largest sample size. We thus feel that our conclusion – that texture-specific spiking sequences are preserved across force levels and form the basis for perceptual invariance – is justified.

3.4 | Methods

3.4.1| Peripheral Nerve Recordings

Stimuli. A diverse set of 55 textured surfaces (see Manfredi et al., 2014 for complete list) was presented to the fingertips of anesthetized macaques using a custom-built rotating drum stimulator, as described previously in detail (Weber et al., 2013). In brief, textured strips (2.5 cm wide x 16 cm in scanning direction) were wrapped around an acrylic drum (25.4 cm in diameter and 30.5 cm in length). The texture set included gratings and tetragonal arrays of embossed dots created from a photosensitive polymer (Printight, Toyobo Co., Ltd.), as well as finer, more naturalistic textures such as fabrics and sandpapers. Textures were scanned across the skin at 80 mm/s for 1.2 s at two different normal forces: 50 and 25 g wt. Each individual texture presentation lasted 1.2 s, followed by an inter-trial interval of 3.5 s, designed to be long enough to minimize the effects of afferent adaptation (Bensmaia et al., 2005; Leung et al., 2005). Each texture was presented two or three times.

Neurophysiology. Extracellular single-unit recordings were obtained from the median and ulnar nerves innervating the distal fingertips of 4 Rhesus macaques (*Macaca mulatta*) as described previously (Muniak et al., 2007; Weber et al., 2013). Data were collected from 4 SA1 a, 1 RA, and 2 PC fibers. All procedures complied with the NIH Guide for the Care and Use of Laboratory Animals and were approved by the Animal Care and Use Committee of the University of Chicago. Some of the data obtained from the one RA was compromised, and so the (good) data from this afferent were used for display purposes only (in Figure 3.1). Responses from two additional RA fibers were obtained in a separate experiment involving recordings from the dorsal root ganglia, described below.

3.4.2| Dorsal Root Ganglion Recordings

Stimuli. The stimuli consisted of 10 textured surfaces – Chiffon, City Light, Corduroy, Crocodile Skin, Deck Chair, Denim, Hucktowel, Metallic Silk, Nylon, and Upholstery –, seven of which were also used in the peripheral nerve recordings. Textures were scanned across the fingertips of anesthetized macaques using a custom-built rotating drum stimulator, a smaller version of the previously described one (Weber et al., 2013). Textured strips, each 2.5 cm wide and 16 cm long along the scanning direction, were wrapped around the drum, itself 14 cm long and 6.4 cm in diameter. Textures were scanned at a speed of 80 mm/s and presented at two different normal forces: 10 and 50 g wt. Each texture was scanned across the skin four times, each for 1.2 s, and texture presentations were separated by inter-trial intervals lasting 3.5 s.

Neurophysiology. Extracellular single-unit recordings were obtained from the dorsal root ganglia of 1 Rhesus macaque, as described previously in cats (Gaunt et al., 2009). Animals

were anesthetized with ketamine and maintained on isoflurane anaesthesia for the duration of the procedure. The C3 though T2 vertebrae were exposed through a midline incision and retraction of the overlying musculature and a dorsal laminectomy was performed to expose the spinal cord from C5 through T1. The laminectomy was extended laterally through the articular processes past the foramina of the C6-C8 spinal roots to expose the dorsal root ganglia (DRG). Ligaments and other issue over the DRG were resected to provide a clear view of the DRG enlargement. 32-channel microelectrode arrays (4x8, Blackrock microsystems) were positioned over the C6-C8 DRG and inserted using a pneumatic high-speed inserter.

Extracellular single-unit recordings were obtained from the dorsal root ganglia innervating the distal fingertips (D2 and D4) of 1 Rhesus macaque (*Macaca mulatta*) using a high density microelectrode array (Utah Array, BlackRock Microsystems, Salt Lake City, Utah). Data were collected from 2 RA fibers. All procedures complied with the NIH Guide for the Care and Use of Laboratory Animals and were approved by the Animal Care and Use Committee of the University of Pittsburgh.

3.4.3| Texture Classification from Neural Data.

For all analyses, we used 500 ms of steady-state spiking data (after the onset transient and before the texture began to lift off the fingertip). To determine the extent to which textures can be distinguished based on spiking sequences evoked in individual afferents, we implemented a nearest neighbour classifier. This classification analysis gauges whether spike trains evoked by one stimulus (in this case a given texture) are more similar to each other than to those evoked by other stimuli (different textures). Specifically, we applied a

leave-one-out approach, in which we computed the dissimilarity between each spike train S_i, and every other spike train. The texture was correctly classified when then mean dissimilarity between S_i and spike trains from the same texture was lower than the mean dissimilarity between S_i and spike trains from each of the other textures. This procedure was repeated for every spike train obtained from each afferent. As a measure of dissimilarity, we employed a spike train distance metric (D_{spike}), used in our previous studies, that computes the cost to transform one spike train into another (Victor and Purpura, 1997; Mackevicius et al., 2012; Weber et al., 2013; Suresh et al., 2016). A cost of 1 is incurred for adding and deleting spikes, and a cost per unit time, q, is incurred to move spikes. By varying q, we can assess the contribution of precise spike timing to the distance computation and thus to the classification performance. That is, a q of 0 leads to a distance metric based solely on differences in spike count: Two spike trains will be different to the extent that the number of spikes is different. With non-zero q's, shifting spikes in time is less expensive than adding or subtracting spikes when the required shifts are less than $2/q$ ms. For each pair of spike trains, we shifted one spike train relative to the other (in 1-ms increments, for up to 100 ms in each direction) and used the minimum distance across all shifts to ensure that the classification analysis could not exploit differences in absolute response phase, which depends on the precise location of the stimulus relative to the receptive field of the nerve fiber. We performed this analysis in two different ways: First, on a subset of the data including only trials at a single contact force (either 25 g wt or 10 g wt, and 50 g wt); second, on the full data set comparing trials from one force to trials from the other. While the former analysis tests whether and at what temporal resolution

information about texture identity is encoded in the spiking sequences, the latter analysis tests the robustness of the neural code across different force levels, and therefore how robust the neural code is to changes in force.

3.5| References

Bensmaïa SJ, Hollins M (2003) The vibrations of texture. Somatosens Mot Res 20:33–43

Bensmaia SJ, Leung YY, Hsiao SS, Johnson KO (2005) Vibratory adaptation of cutaneous mechanoreceptive afferents. J Neurophysiol 94:3023–3036.

Callier T, Saal HP, Davis-Berg EC, Bensmaia SJ (2015) Kinematics of unconstrained tactile texture exploration. J Neurophysiol 113:3013–3020.

Cascio CJ, Sathian K (2001) Temporal cues contribute to tactile perception of roughness. J Neurosci 21:5289–5296.

Gaunt RA, Hokanson JA, Weber DJ (2009) Microstimulation of primary afferent neurons in the L7 dorsal root ganglia using multielectrode arrays in anesthetized cats: thresholds and recruitment properties. J Neural Eng 6:055009 Available at: http://www.ncbi.nlm.nih.gov/pubmed/19721181 [Accessed July 20, 2017].

Johansson RS, Vallbo AB (1983) Tactile sensory coding in the glabrous skin of the human hand. Trends Neurosci 6:27–32.

Knibestöl M (1973) Stimulus-response functions of rapidly adapting mechanoreceptors in the human glabrous skin area. J Physiol 232:427–452.

Knibestöl M (1975) Stimulus-response functions of slowly adapting mechanoreceptors in the human glabrous skin area. J Physiol 245:63–80.

Lederman S (1981) The perception of surface roughness by active and passive touch. Bull Psychon Soc 18:253–255.

Lederman SJ (1974) Tactile roughness of grooved surfaces: The touching process and effects of macro- and microsurface structure. Percept Psychophys 16:385–395.

Lederman SJ, Taylor MM (1972) Fingertip force, surface geometry, and the perception of roughness by active touch. Percept Psychophys 12:401–408.

Leung YY, Bensmaia SJ, Hsiao SS, Johnson KO (2005) Time-course of vibratory adaptation and recovery in cutaneous mechanoreceptive afferents. J Neurophysiol 94:3037–3045 Available at: http://jn.physiology.org/content/94/5/3037.short [Accessed August 21, 2014].

Mackevicius EL, Best MD, Saal HP, Bensmaia SJ (2012) Millisecond precision spike timing shapes tactile perception. J Neurosci 32:15309–15317.

Manfredi LR, Saal HP, Brown KJ, Zielinski MC, Dammann JF, Polashock VS, Bensmaia SJ (2014) Natural scenes in tactile texture. J Neurophysiol 111:1792–1802 Available at: http://www.ncbi.nlm.nih.gov/pubmed/24523522 [Accessed August 21, 2014].

Meftah el-M, Belingard L, Chapman CE (2000) Relative effects of the spatial and temporal characteristics of scanned surfaces on human perception of tactile roughness using passive touch. Exp Brain Res 132:351–361.

Morley JW, Goodwin AW, Darian-Smith I (1983) Tactile discrimination of gratings. Exp Brain Res 49:291–299.

Muniak MA, Ray S, Hsiao SS, Dammann JF, Bensmaia SJ (2007) The neural coding of stimulus intensity: linking the population response of mechanoreceptive afferents with psychophysical behavior. J Neurosci 27:11687–11699 Available at: http://www.jneurosci.org/content/27/43/11687.short [Accessed August 21, 2014].

Saal HP, Wang X, Bensmaia SJ (2016) Importance of spike timing in touch: an analogy with hearing? Curr Opin Neurobiol 40:142–149 Available at: http://www.ncbi.nlm.nih.gov/pubmed/27504741 [Accessed August 18, 2016].

Skedung L, Arvidsson M, Chung JY, Stafford CM, Berglund B, Rutland MW (2013) Feeling small: exploring the tactile perception limits. Sci Rep 3:2617.

Smith AM, Chapman CE, Deslandes M, Langlais J-S, Thibodeau M-P (2002a) Role of friction and tangential force variation in the subjective scaling of tactile roughness. Exp Brain Res 144:211–223.

Smith AM, Gosselin G, Houde B (2002b) Deployment of fingertip forces in tactile exploration. Exp brain Res 147:209–218.

Suresh AK, Saal HP, Bensmaia SJ (2016) Edge orientation signals in tactile afferents of macaques. J Neurophysiol 116:2647–2655.

Tanaka Y, Bergmann Tiest WM, Kappers AML, Sano A (2014) Contact Force and Scanning Velocity during Active Roughness Perception. PLoS One 9:e93363.

Vega-Bermudez F, Johnson KO (1999) Surround suppression in the responses of primate SA1 and RA mechanoreceptive afferents mapped with a probe array. J Neurophysiol 81:2711–2719.

Victor JD, Purpura KP (1997) Metric-space analysis of spike trains: Theory, algorithms and application. Network-Comp Neural 8:127–164.

Weber AI, Saal HP, Lieber JD, Cheng J-WW, Manfredi LR, Dammann 3rd JF, Bensmaia SJ, Dammann JF, Bensmaia SJ (2013) Spatial and temporal codes mediate the tactile perception of natural textures. Proc Natl Acad Sci 110:17107–17112 Available at: http://www.pnas.org/content/110/42/17107.short [Accessed August 21, 2014].

Chapter 4 | Peripheral Coding of Contact Events[3]

Manual interactions with objects require precise and rapid feedback about contact events. These tactile signals are integrated with motor plans throughout the neuraxis to achieve dexterous object manipulation. To better understand the role of peripheral afferents in interactions with objects, we simulated the responses of populations of afferents to skin indentations designed to mimic the initiation, maintenance, and termination of contact with an object. First, we find that the population responses of tactile afferents to contact onset and offset dwarf their responses to maintenance of contact. Second, we show that these responses rapidly and reliably encode features of the simulated contact events such as indentation rate and depth. Third, we demonstrate that the spatio-temporal dynamics of the population response in cortex (activity evoked in somatosensory cortex using chronically implanted arrays) mirror those of the population response in the nerves. We conclude that the responses of populations of tactile afferents are well suited to encode contact transients and are consistent with a role of somatosensory system in signaling transitions between task subgoals.

[3] This chapter is part of a publication: Callier, T.*, Suresh, A. K.*, & Bensmaia, S. J. (2018). Neural Coding of Contact Events in Somatosensory Cortex. Cerebral Cortex, 1–15.
*Contributed Equally

4.1 | Introduction

During manual interactions with an object, tactile signals provide precise and rapid feedback about the interface between hand and object. Several populations of mechanoreceptors in the skin convey detailed information about the timing, location, and nature of the contacts, and these signals are critical to our ability to dexterously manipulate objects (Augurelle et al. 2003; Witney et al. 2004; Johansson and Flanagan 2009).

Our goal was to understand how the onset and offset of contact – during which the object moves into or retracts from the skin – and its maintenance – during which contact is approximately static – are encoded in the response of populations of somatosensory afferents, and how indentation depth and indentation rate modulate neuronal responses to contact. We also investigated the degree to which the spatiotemporal dynamics of the population responses in cortex reflect their inputs from the periphery by examining the measured responses of populations of somatosensory cortical neurons to these same contact events.

4.2 | Results

4.2.1 Spatio-temporal dynamics of the response in the peripheral nerve

We simulated the responses, using TouchSim (Saal et al. 2017) to all afferents activated by an indentation with a punctate probe at different locations, to different depths, and at different indentation rates. We found that hundreds of afferents were activated, and that their aggregate response during the transients dwarfed that during the sustained portion of the stimulus, which was, again, remarkably weak (Figure 4.1A, also shown for measured responses, as a control, in Supplementary Figure S4.1A).

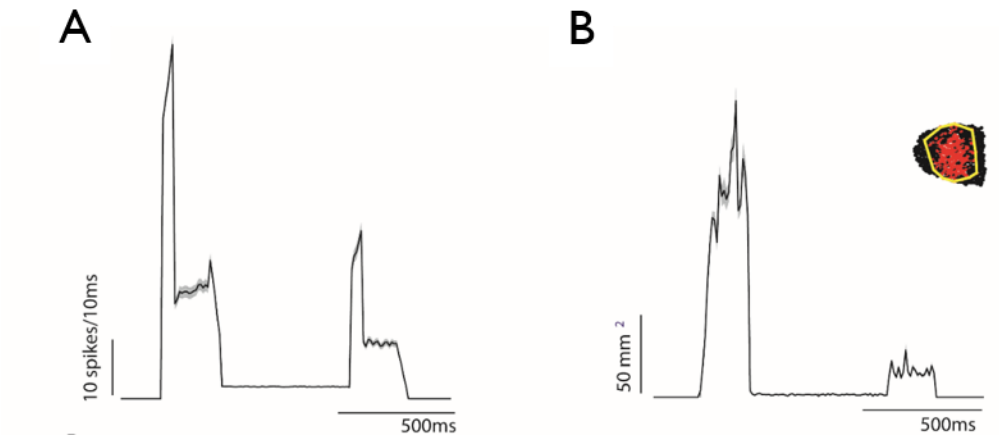

Figure 4.1 Spatiotemporal dynamics of peripheral responses to skin indentations

A | Simulated aggregate afferent responses (SA1, RA, and PC fibers) to a 2-mm, 10-mm/s indentation delivered to various locations on the hand, matched to those used in the cortical experiments (See Supplementary Figure S4.2). Spike count represents summed spikes over the afferent population, in 10-ms bins, averaged across locations (Supplementary Fig S4.2: mean= 2498 fibers, stdev=1369 fibers). Shaded area represents standard error of the mean over all locations (n=16). B| Dynamics of the spatial extent of simulated afferent activation for 20-ms bins. Area was set to 0 for time points where less than 3 afferents were recruited, inset shows an example diagram of the polygon-based area computation.

The dominance of the transient response is due to the fact that RA and PC fibers only respond to changes in skin indentation, leaving only SA1 fibers to respond to the sustained

indentation, and even these fibers respond more strongly to skin deflections (Knibestöl 1973, 1975). We also computed the transient-to-sustained-response ratio for aggregate peripheral responses to a probe with a diameter of 2 mm indented 2 mm into the skin at 10 mm/s, and found that transient responses were on average nearly 12 times (range 5.12-45.37, median 9.2, see Table 1) stronger at stimulus onset and more than 5 times stronger at stimulus offset than sustained responses.

Table 4.1. Transient/Sustained ratios for simulated afferent responses by stimulus location.

Metrics (mean, range, median) characterizing the distribution of onset/sustained and offset/sustained firing rate ratios for simulated afferents at the hand locations for which cortical data was collected. The stimulus was a 2-mm, 10-mm/s indentation. As is the case in cortical responses, responses are more transient in the palm than in the digits, reflecting differences in innervation patterns.

		Onset/sustained	Offset/sustained
ALL	Mean	11.76	5.47
	Range	5.12-45.37	2.15-19.4
	Median	9.2	4.2
DISTAL	Mean	9.96	5.42
	Range	8.70-12.33	3.90 – 8.0
	Median	8.86	4.37
PALM	Mean	17.90	7.69
	Range	8.16-45.37	3.96-19.4
	Median	11.66	5.21

These ratios tended to be larger for the palm than for the distal digits, reflecting differences in the relative proportions of slowly adapting and rapidly adapting nerve fibers terminating in the different hand regions.

We then examined how the spatial pattern of activation evoked in nerve fibers by a skin indentation evolved over time. To this end, we computed the area of a polygon that

contains all (simulated) SA1 and RA afferents activated by the stimulus as a function of time. We excluded PC fibers in this computation because their receptive fields are so large as to span most of the hand, and a given PC fiber is activated by touch almost anywhere on the hand. Afferent activation during stimulus transients was distributed across wide swaths of skin around the probe, while activation during the static phase was localized to a small patch of skin under the probe (Figure 4.1B).

4.2.2 Dependence of the peripheral response on contact parameters

Next, we examined the dependence of the nerve response on the features of the contact event. First, we investigated the dependence of transient responses on indentation rate. Restricting our analysis to the period of time when the probe is moving, we found that both the population firing response and the spatial extent of the activation increased monotonically with indentation rate (Figure 4.2).

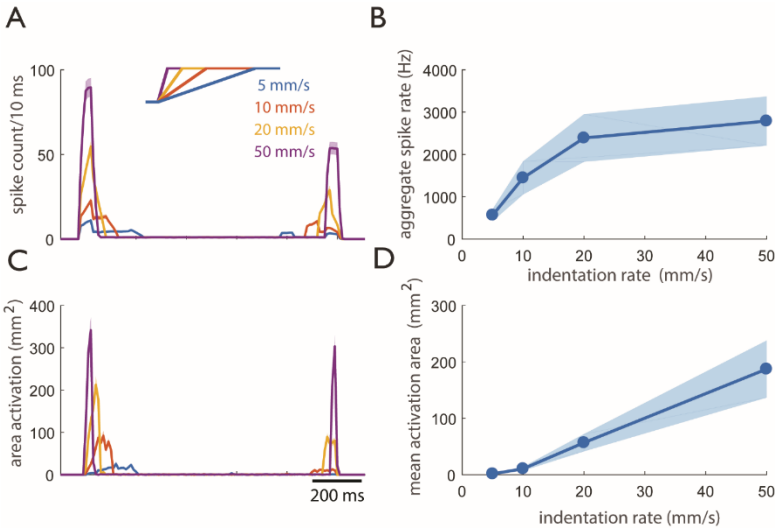

Figure 4.2 Effect of indentation rate on the afferent response.

A| Aggregate afferent response (spike count) to indentations at different rates (indentation depth = 1.0 mm). Transient responses scale with indentation rate. See timescale bar in panel C. B| Population firing rate during transient (first 20 ms) as a function of indentation rate. C| Area of activated afferents for different indentation rates. The area of activation during the transient response scales with indentation rate. D| Mean area of activation as a function

of indentation rate over the transient interval (first 20 ms). Shaded areas represent standard error of the mean over multiple skin locations (n=16, specified in Supplementary Figure S4.2).

Next, we examined the dependence of the response on indentation depth (Figure 4.3). During the transients, the modulation of firing rate and recruitment by indentation depth was weak compared to the modulation of firing rate and recruitment by indentation rate (Figure 4.3B,D). If anything, firing rate seems to decrease as amplitude increases because, as the ramp gets longer, the strong initial burst (possibly driven by an acceleration event) gets washed out and this effect counteracts the weak amplitude-dependent increase in firing rate.

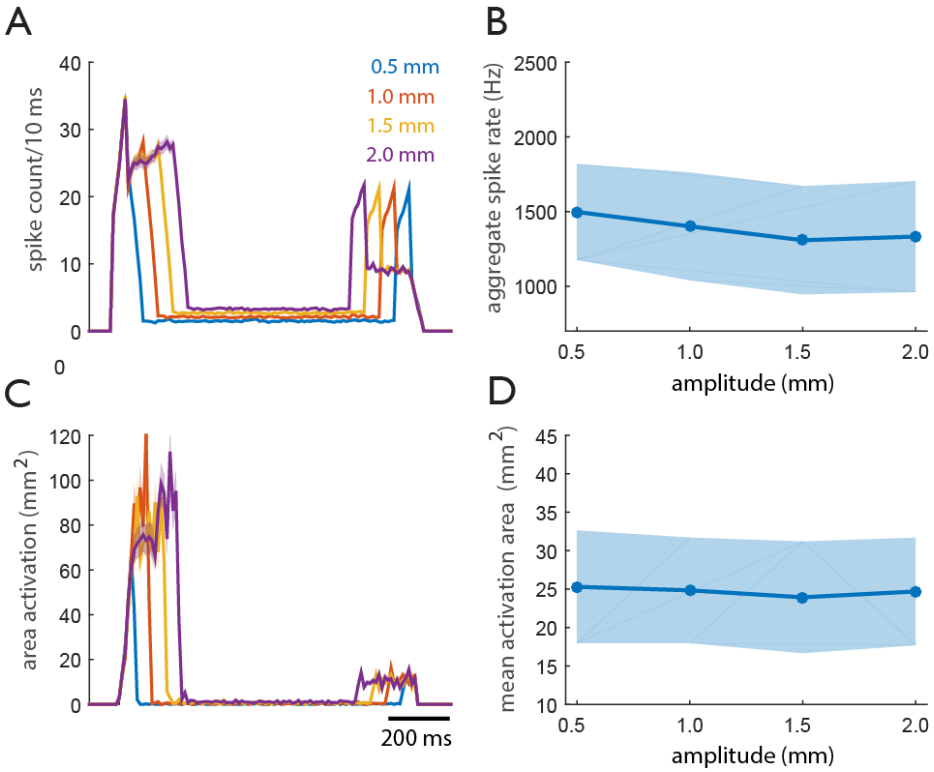

Figure 4.3 Effect of indentation depth on the sustained and transient responses in the nerve.

A| Time course of the simulated population response to indentations at 4 indentation depths: 0.5, 1.0, 1.5, and 2.0 mm with a fixed indentation rate of 10 mm/s. See timescale in C. B| Aggregate spike rate during transient phase (while the probe is moving) as a function of indentation depth. Firing rates are independent of amplitude during the transient phase

Figure 4.3, continued. (spike rate computed over respective ramp durations). C| Time course of the activated area for four indentation depths. D| Mean area of afferent activation as a function of indentation depth over the transient phase (mean area computed over respective ramp durations). Increases in amplitude have a negligible effect on recruitment. Shaded areas represent standard error of the mean over multiple skin locations (n=16, specified in Supplementary Figure 2).

Overall, we found that the strength and spatial extent of simulated afferent responses during the transient phase of the stimulus were only weakly modulated by indentation depth, whereas the afferent responses during the transient phase were strongly modulated by indentation rate.

4.2.2 Comparing peripheral and cortical population responses

Finally, we wished to assess the degree to which cortical responses[4] reflect their peripheral inputs. To this end, we recorded the multi-unit responses evoked across populations of neurons in area 1 when the palmar surface of the hand was indented with a punctate probe with the identical parameters as the ones described in the peripheral experiment. To quantify the similarity between peripheral and cortical responses, we computed the cross-correlation between peripheral and cortical PSTHs to the same stimuli and found these to be high (mean ± s.d.: 0.92 ± 0.03) (Figure 4.4). In conclusion, then, the spatio-temporal dynamics of cortical responses to simulated contact events are highly similar to their peripheral counterparts.

[4] For complete analysis of cortical data, please refer to: Callier, T.*, Suresh, A. K.*, & Bensmaia, S. J. (2018). Neural Coding of Contact Events in Somatosensory Cortex. Cerebral Cortex, 1–15. *Contributed Equally

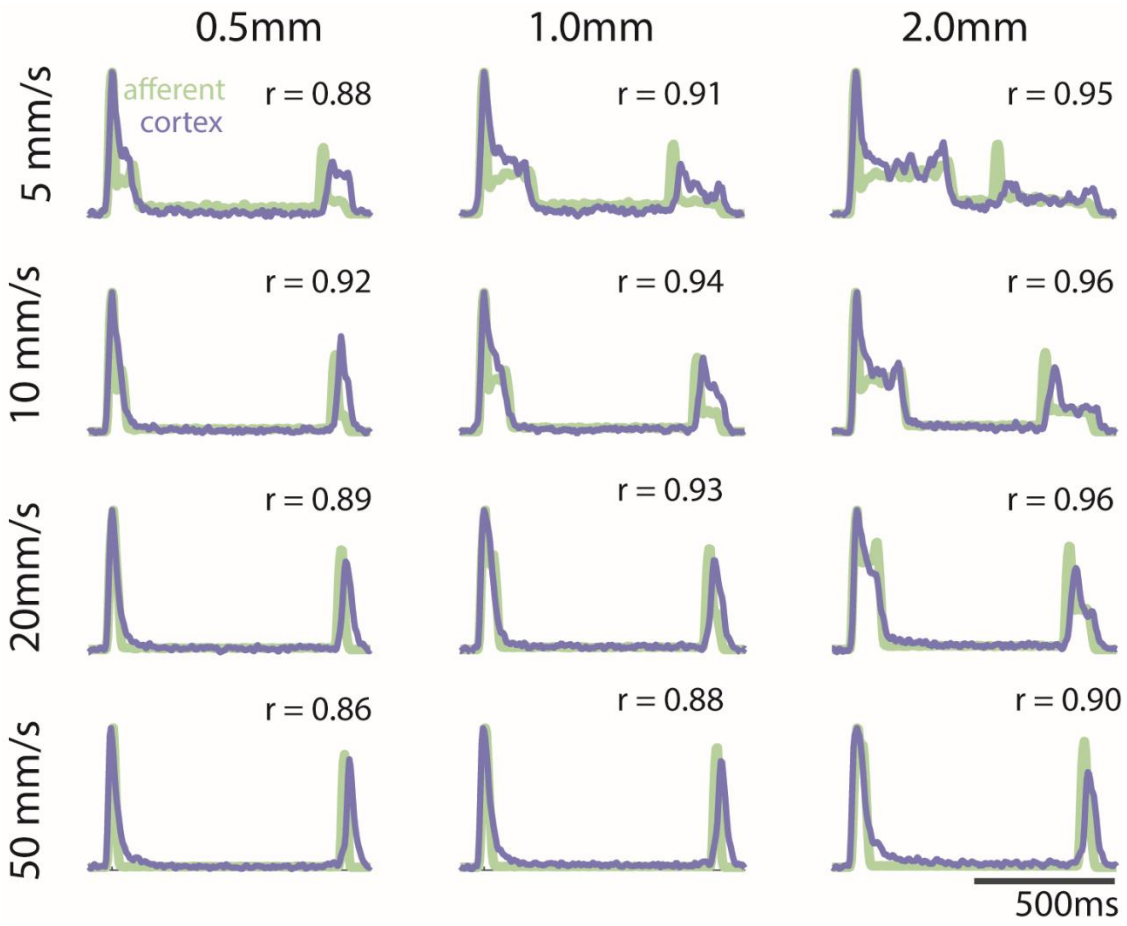

Figure 4.4: Correlation between afferent and cortical responses.

For each indentation rate/depth pair (12 total conditions), (simulated) afferent traces across 3 locations (distal fingerpad, proximal fingerpad, and palm) are shown in green, and (measured) cortical traces across the same 3 stimulation locations from monkey B's second array and monkey C (Supplementary Figure 4.2) are shown in blue. Traces were smoothed with a Gaussian kernel width of 20 ms, and aligned to correct for conduction latency. Mean correlation over all 12 conditions is 0.92, (s.d. = .033).

4.3| Discussion

In summary, then, we found that population responses during the initiation and termination of contact dwarf responses during static contact both in the nerve and in the cortex, so these responses primarily signal contact transients – *changes* in skin deformation – rather than tracking indentation depth. Furthermore, contact events are encoded in both the time-varying response of activated neurons as well as the time-varying size of the activated population. While responses to contact transients are strong and diffuse, responses to sustained contact are weak and highly localized. Finally, the spatiotemporal profile of the population response to contact in cortex mirrors its counterpart in the nerve.

Similarity of peripheral and cortical response dynamics

The aggregate response of cortical neurons to contact events is very similar to that of their peripheral inputs. First, the coarse temporal profiles of the spiking response are nearly identical to its cortical counterpart, featuring a prominent phasic response during contact transients and a weak tonic response during maintained contact. As alluded to above, a major source of the strong transient response in the nerve is the population of rapidly adapting afferents, including RA and PC fibers, which respond exclusively during the transients, and the stronger response of SA1 fibers during the indentation phase. Second, the dynamics of recruitment observed in cortex also seem to mirror those at the periphery. Indeed, phasic recruitment of nerve fibers originating from afferents close to but not under the probe is observed during the transient periods and only a small population of SA1 fibers with RFs just under the probe is activated during sustained contact. Not only are the relative strengths of the transient and sustained responses similar in periphery and cortex,

but their dependence on the locus of stimulation is also consistent (with weaker sustained responses from the palm). Finally, the dependence of the spatiotemporal dynamics of nerve responses on stimulus parameters – including indentation depth and indentation rate – largely mirrors its cortical counterpart.

That the aggregate response in cortex resembles that in the nerve does not imply that no information processing occurs between nerve and cortex. Indeed, individual cortical neurons have complex receptive fields with excitatory and inhibitory subfields (DiCarlo et al. 1998), often exhibit feature selectively (to edge orientation (Bensmaia et al. 2008) or direction of motion (Pei et al. 2010), e.g.), and integrate their inputs non-linearly (Chung et al. 2002; Katz et al. 2006; Thakur et al. 2006; Reed et al. 2010, 2011; Brouwer et al. 2015; Saal et al. 2015) to name a few properties that are largely absent in tactile nerve fibers. Interestingly, however, this processing is largely obscured when pooling responses to contact events across populations of neurons.

Active vs. passive touch

One might argue that the neuronal activity when stimuli are passively presented to the skin may not be representative of that evoked during active manipulation of objects. However, several lines of evidence suggest otherwise.

First, while the temporal profile of the indentations, following a trapezoidal trajectory, is highly contrived and may not match that of natural contact event, afferent responses to a natural indentation profile, corresponding to grasping and releasing a coffee cup, exhibit very similar spatio-temporal dynamics (Supplementary Figure 4.1B).

Second, tactile discrimination and pattern recognition are similar for active and passive touch (Lamotte and Whitehouse 1986; Vega-Bermudez et al. 1991), suggesting that the processing of cutaneous information is similar under these two conditions.

Third, studies explicitly comparing responses of somatosensory neurons to active and passive touch have found weak or no differences in firing rates, and any observed differences could be attributed to differences in the contact events themselves or in the attentional state of the animal (Chapman and Ageranioti-Belanger 1991; Jiang et al. 1991; Ageranioti-Bélanger and Chapman 1992; Williams and Chapman 2002). Regarding the former confound, comparing the neuronal responses to active and passive touch is challenging because it is impossible to exactly match how the skin is deformed in the two conditions and the sense of touch is exquisitely sensitive to any differences in skin deformation (down to the level of single-digit microns). Indeed, as discussed above, even under passive conditions, skin deflections produced by an identical stimulus are highly variable given the slights movements of the (restrained) hand, a challenge we circumvent by imposing a pre-indentation.

Fourth, while single-unit cortical responses evoked during grasping (Wannier et al. 1986, 1991; Gardner et al. 1999; Salimi et al. 1999; Ro et al. 2000; Debowy et al. 2001) are difficult to compare to aggregate cortical responses presented here, somatosensory neurons with receptive fields on the glabrous skin have been found to exhibit properties qualitatively consistent with those described here, often characterized by strong phasic responses at initiation and termination of contact and weak responses during maintenance of contact. Another component of active touch that may influence tactile responses in somatosensory

cortex is movement-gating, a phenomenon that has been documented for the balance sense, vision, and touch (Cullen et al. 2004). However, while cortical responses to touch on the proximal limb are suppressed during movement, the response dynamics seem to be preserved (Jiang et al. 1990, 1991). Moreover, the function of movement gating of touch on the proximal limb may be to reduce tactile signals produced by skin stretch during movement (Rincon-Gonzalez et al. 2011), which, in some cases, may be behaviorally irrelevant and distracting. In this view, it is unlikely that tactile responses on the glabrous skin would be suppressed during object manipulation as these signals are the ones critical to behavior.

In light of these considerations and previous findings, we expect that the cutaneous responses to object contact in somatosensory neurons are unlikely to be fundamentally altered under conditions of active touch and that passive stimulation reveals the main characteristics of the representation of contact events at this stage of processing along the somatosensory neuraxis.

Functional significance of the phasic response to contact transients

Object manipulation can be broken down into a sequence of action phases delimited by mechanical events associated with subgoals of the task. In reach and grasp, for example, contact with an object marks the end of the reach phase and signals the beginning of the grasp phase (Johansson and Flanagan 2009). Consistent with this view, disruption of somatosensory cortex with a pulse of transcranial magnetic stimulation (TMS) just before contact results in delayed initiation of the grasp (Lemon et al. 1995). Moreover, contact timing between object and fingers drives the online adaptation of grasp aperture during

active grasping movements (Säfström and Edin 2008). The prominence of contact transients in somatosensory signals is consistent with a role for tactile feedback in signaling transitions between task goals rather than providing continuous feedback about object interactions (Johansson and Edin 1993; Johansson and Flanagan 2009). We would therefore expect that these phasic transients are key components of sensorimotor integration during object manipulation.

This is not to say that sustained responses are not useful and informative. Indeed, stimulus features – local object shape, e.g. – may be most prominently encoded in cortical responses during sustained contact (see (Bensmaia et al. 2008; Yau et al. 2013)). However, this slower signal may be less important for online motor control and play a greater role in haptic perception (Yau et al. 2016).

4.4 | Supplementary Materials

4.4.1 Single unit recording from the nerve

To validate results from the nerve simulation (described in the main Methods), we analyzed data collected in a separate experiment in which we recorded the responses of individual afferents to half-spheres indented into the skin. Our neurophysiological data consists of a small sample of afferent fibers, while the simulation accounts for all afferents innervating the hand. Results from this analysis are shown in Supplementary Figure 4.2A.

Stimuli

Stimuli were delivered using the dense array tactile stimulator described above. Stimuli consisted of half spheres with a 2 mm diameter and an amplitude of 0.3 mm at their apex,

and a rate of 10 mm/s. The stimulus was presented for 100 ms, centered on the afferent's hotspot. Stimuli were presented 8 times.

Neurophysiology

All experimental protocols complied with the guidelines of The Johns Hopkins University Animal Care and Use Committee and the National Institutes of Health's Guide for the Care and Use of Laboratory Animals. We recorded single units from the median and ulnar nerves of four anaesthetized macaque monkeys using standard methods (Mountcastle et al. 1967; Talbot et al. 1968) as previously described in detail (Bensmaia et al. 2008). In brief, the forearm and hand were fixed by a clamp, and the ulnar or median nerve was exposed in the upper or lower arm. Next, a skin flap pool was formed, and a small bundle of axons was separated from the nerve trunk and wrapped around a silver electrode. Each animal contributed up to eight recording sessions – upper and lower sites on median and ulnar nerve – separated by two or more weeks.

A nerve fiber was classified as slowly adapting type 1 (SA1) if it had a small receptive field (RF) and produced a sustained response to a skin indentation, as rapidly adapting (RA) if it had a small RF and responded only at the onset and offset of the indentation, and as Pacinian (PC) if it had a large, diffuse RF and was activated by air blown gently over the hand. The point of maximum sensitivity (hotspot) was located using a handheld probe and the stimulus was centered on the hotspot. In these experiments, data were only collected from SA1 and RA fibers.

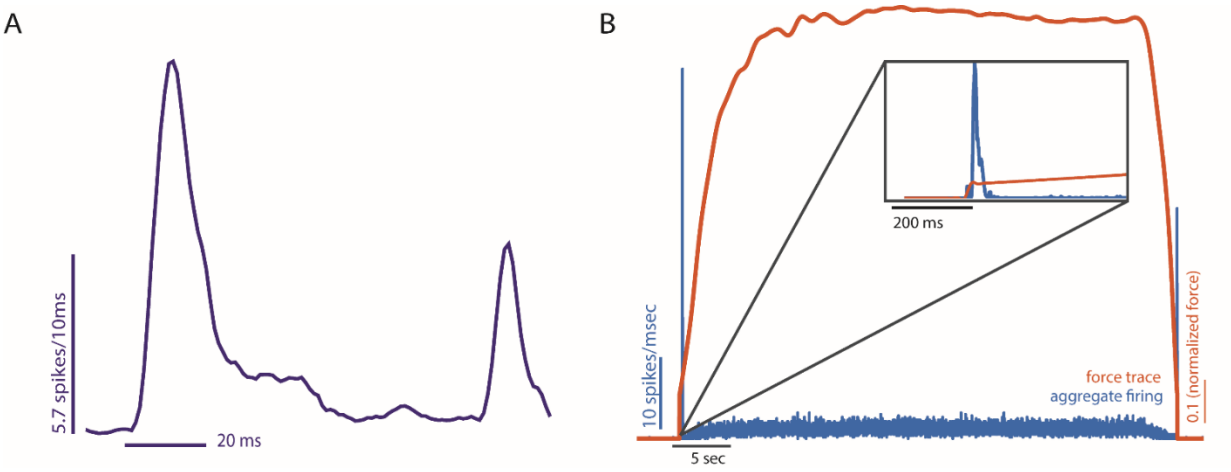

Supplementary Figure 4.1. Validation of nerve stimulation and of mechanical stimulation paradigm.

A| Aggregate spike count of (measured) SA1 and RA responses (n=6 and 10 respectively, group sizes were selected to match the ratio of innervation densities found at the fingertip) to a skin indentation (0.3 mm, 10 mm/s, 100 ms). Measured responses are analogous to simulated ones but the latter can be tailored to the stimuli used in the cortical experiments and can reconstruct the spatio-temporal response of the entire nerve. B| Aggregate afferent response to grasping and releasing a coffee cup. Orange trace represents load on the index finger as a coffee cup is grasped, lifted, and put down. The simulated population response is shown in blue (binned at 5 ms). Inset shows a close up of the initial transient response. Simulated afferent response to an actual contact event is similar to the response to a skin indentation.

4.4.2 Simulating the response of the nerve during a manual interaction with an object

To verify that the simulated and measured neural responses to the trapezoidal indentation were representative of those evoked during an object interaction, we simulated the responses to the pressure profile measured during the grasp, hold, and release of an object. Specifically, we used a sensorized glove (FingerTPS, PPS, Inc., Los Angeles, CA) with six pressure sensors – one on each fingertip and one on the palm – to measure pressure exerted when a coffee cup is grasped, lifted, then put down (for a detailed description, see (Kim et

al. 2011)). Given that indentation depth is approximately linear with contact pressure over a range, we converted the output of the index finger sensor into indentation depths by scaling the pressure trace to a maximum of 3 mm. The pressure trace exhibited a similar profile to the simple ramp indentations tested, but the trace extended over a much longer duration (~50 seconds). Finally, we rescaled the indentation output from 64 to 512 Hz, and input this trace into TouchSim to simulate the aggregate afferent response (Supplementary Figure 4.1B).

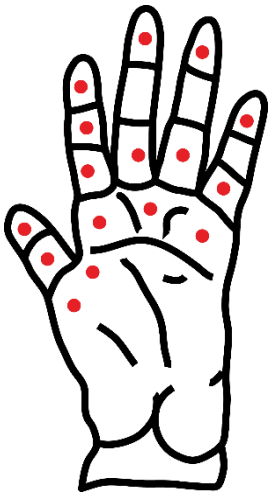

Supplementary Figure 4.2. Stimulation sites for peripheral model.

Every dot indicates a skin site that was stimulated. Blue dots indicate sites that were not included in any analyses because the associated hotzone was off the array.

4.5|Methods

4.5.1 Simulations of whole nerve responses

We wished to compare the responses to contact events in somatosensory cortex and in the somatosensory nerves. To this end, we reconstructed the responses of all tactile nerve fibers – slowly adapting type 1 (SA1), rapidly adapting (RA), and Pacinian corpuscle-associated

(PC) – that innervate the palmar surface of the hand to each of the stimuli presented in the cortical experiments. Specifically, we used a recently developed simulation of the nerve that can accurately reproduce afferent responses with near millisecond accuracy (Saal et al. 2017). In brief, the model first computes the skin's response to a time-varying stimulus impinging upon it, then generates the spiking response evoked in nerve fibers whose receptive fields (RFs) tile the skin at measured innervation densities. This simulation has been extensively validated using a variety of psychophysical and neurophysiological data sets (Goodman and Bensmaia 2017; Saal et al. 2017). Using this model, we simulated the nerve responses to the mechanical stimuli used in the cortical experiments, described above, and compared these simulated responses to their measured cortical counterparts. We delivered the simulated indentations at each location that was mechanically stimulated in the cortical experiments (See Supplementary Figure 4.2). For finger sites, we simulated responses over each respective finger, and for palm sites, we simulated responses over the entire palm (mean = 2498 fibers, stdev = 1369 fibers). For recruitment calculations, we only included SA1 and RA afferent responses. To validate the simulation, we compared simulated afferent responses to a skin indentation to their measured counterparts (see section entitled "*Single unit recordings from the nerve*" in the Supplementary Materials and Supplementary Figure 4.1).

To compare simulated responses of tactile nerve fibers to the measured responses of cortical neurons, we computed the cross correlation between their respective peri-stimulus time histograms (PSTHs) using an average for each stimulus across locations (distal finger, proximal finger, and palm; see Supplementary Figure 4.2). Specifically, for each stimulus

condition (12 pairs varying in indentation depth and indentation rate), we smoothed the responses, starting 500 ms before stimulus onset to 500 ms after stimulus offset, with a 20 ms Gaussian kernel and computed the correlation coefficient at the optimal lag.

To verify that the indentations were ethologically valid, we simulated the response to a time-varying indentation that resembles the skin deflection produced when an object is grasped, lifted up, and released (*see section entitled "*Simulating the response of the nerve during a manual interaction with an object" in the Supplementary Methods*).* We then compared the simulated responses of tactile nerve fibers to this naturalistic stimulus and to the trapezoidal indentations.

4.5.2 Cortical Data

Animals

Three male Rhesus macaques (Macaca mulatta), 7-9 years old and weighing 9-10 Kg, participated in this study. Animal care and handling conformed to the procedures approved by the University of Chicago Animal Care and Use Committee.

Implants

Each animal was implanted with one Utah electrode array at a time (UEA, Blackrock Microsystems, Inc., Salt Lake City, UT) in the hand representation of area 1. Monkeys A and C were implanted with one array each, whereas monkey B was implanted with a second array after the first one failed. Each UEA consists of 96 electrodes, each 1.5 mm long, with tips coated with iridium oxide, spaced 400 μm apart, and spanning 4 mm x 4 mm of the cortical surface. The hand representation in area 1 was targeted based on anatomical

landmarks. Given that the arrays were contiguous to the central sulcus and area 1 spans approximately 3-5 mm of cortical surface from the sulcus (Pons et al. 1985), few if any electrodes were located in area 2. Given the length of the electrodes, their tips terminated in the infragranular layers of somatosensory cortex, as we have previously shown in postmortem histological analysis with other animals instrumented with identical arrays (Rajan et al. 2015).

Stimuli

Mechanical stimuli consisted of one-second long trapezoidal indentations delivered to the palmar surface of the hand using a high-precision custom-made tactile stimulator (similar to the one described in detail in (Tabot et al. 2013)). Initially, we delivered the stimuli by measuring the position of the hand along the vertical axis using a high-precision range finder (Accurange 200–25; Acuity Lasers, Portland, OR) and having the indenting probe traverse this distance before it followed the desired indentation trajectory. Because the monkey's hand does not remain perfectly still, however, the position of the hand relative to the indenting stimulator changed over time in unpredictable ways by tens or hundreds of microns. These gradual shifts in hand position thus made it impossible to deliver indentations at a precisely controlled depth and resulted in fluctuations in the time at which the probe made contact with the skin.

To achieve well controlled skin deflections, then, we elected to pre-indent the stimulator tip 500 μm into the skin throughout the duration of each experimental session, and the indentation trajectory was delivered beyond this pre-indentation. This experimental decision is predicated on the fact that afferent responses to the pre-indentation decay away

within 10-20 seconds, as does the resulting sensation, and afferent responses to indentations of the skin beyond the pre-indentation are identical to those with no pre-indentation (Vega-Bermudez and Johnson 1999). We compared cortical responses to actual contact events (from no contact to contact, with the probe starting position 0.5 to 1 mm above the finger) to the cortical responses to simulated contact (with the pre-indentation) and found that, while the strength and timing of the latter was more variable than that of the former, the response profiles were otherwise virtually identical (See the section entitled "***Pre-indentation vs actual contact" in the Supplementary Methods*** of the cited paper for details). Indentation depths ranged from 150 to 2000 μm, indentation rates from 5 to 50 mm/s, and probe diameter was 2 mm. All stimuli were reliably detectable for the animals (Callier et al. 2015), and were presented in pseudorandom order.

Electrophysiology recording

We simultaneously recorded from all 96 electrodes of the UEAs using a Cerebus system (Blackrock Microsystems, Salt Lake City, UT), passed the continuous voltage signal from each electrode, sampled at 30 kHz, through a 100-Hz high-pass filter to reduce background noise, and recorded the timing of threshold-crossing events in each channel. Because we were interested in population responses, we analyzed multi-unit (rather than single-unit) activity.

Standardizing neuronal responses

Multiunit activity varies widely from electrode to electrode, both at baseline when no stimulus is applied, and in response to a stimulus, as might be expected given that different

electrodes acquire signals from neuron groups that vary in size, sensitivity, and spontaneous firing rate. Counting spikes is therefore an inadequate gauge of evoked activity if one wishes to compare across electrodes. If the objective is to build an activation map across the cortical surface, it is necessary to correct for this source of variability. To this end, we standardized the evoked response according to the baseline activity (i.e., converted it to a z-score):

$$R_S(t) = \frac{(R(t)-\mu_b)}{\sigma_b}$$

where $R(t)$ is the spike count in time bin t (whose width differed across analyses and ranged from 1 to 1200 ms), μ_b is the mean spike count per bin during baseline, and σ_b is the standard deviation of the spike count per bin during baseline. Baseline spike count distributions were estimated from the response in the 500-ms time window preceding the first stimulus of each trial. Baseline levels were computed for each electrode and experimental block separately. Thus, $R_s(t)$= 3 indicates a spike rate at time t that is 3 standard deviations above the mean baseline spike rate for that electrode on that experimental block. We quantified the spatial extent of cortical activation by tracking the area of the array over which the neuronal activity exceeded a threshold (2 s.d. above baseline unless otherwise specified).

Ageranioti-Bélanger SA, Chapman CE. 1992. Discharge properties of neurones in the hand area of primary somatosensory cortex in monkeys in relation to the performance of an active tactile discrimination task. II. Area 2 as compared to areas 3b and 1. Exp brain Res. 91:207–228.

Augurelle A-S, Smith AM, Lejeune T, Thonnard J-L. 2003. Importance of cutaneous feedback in maintaining a secure grip during manipulation of hand-held objects. J Neurophysiol. 89:665–671.

Bensmaia SJ. 2015. Biological and bionic hands: Natural neural coding and artificial perception. Philos Trans R Soc B Biol Sci. 370.

Bensmaia SJ, Denchev PV, Dammann III JF, Craig JC, Hsiao SS. 2008. The representation of stimulus orientation in the early stages of somatosensory processing. J Neurosci. 28.

Britten KH, Shadlen MN, Newsome WT, Movshon JA. 1992. The analysis of visual motion: a comparison of neuronal and psychophysical performance. J Neurosci. 12:4745–4765.

Brochier T, Boudreau MJ, Paré M, Smith AM. 1999. The effects of muscimol inactivation of small regions of motor and somatosensory cortex on independent finger movements and force control in the precision grip. Exp brain Res. 128:31–40.

Brouwer GJ, Arnedo V, Offen S, Heeger DJ, Grant AC. 2015. Normalization in human somatosensory cortex. J Neurophysiol. 114:2588–2599.

Callier T, Schluter EW, Tabot GA, Miller LE, Tenore F V, Bensmaia SJ. 2015. Long-term stability of sensitivity to intracortical microstimulation of somatosensory cortex. J Neural Eng. 12:056010.

Carlson M. 1981. Characteristics of sensory deficits following lesions of Brodmann's areas 1 and 2 in the postcentral gyrus of Mococo mulatto. Brain Res. 204:424–430.

Chapman CE, Ageranioti-Belanger A. 1991. Experimental Brain Research Discharge properties of neurones in the hand area of primary somatosensory cortex in monkeys in relation to the performance of an active tactile discrimination task I. Areas 3b and 1. Exp Brain Res. 87:31–339.

Chung S, Li X, Nelson SB. 2002. Short-term depression at thalamocortical synapses contributes to rapid adaptation of cortical sensory responses in vivo. Neuron. 34:437–446.

Cohen R, Vierck C. 1993. Population estimates for responses of cutaneous mechanoreceptors to a vertically indenting probe on the glabrous skin of monkeys. Exp Brain Res. 94:105–119.

Cullen KE, Anderson ME, Kiehn O. 2004. Sensory signals during active versus passive movement This review comes from a themed issue on Motor systems Edited Abbreviations fMRI function magnetic resonance imaging. Curr Opin Neurobiol. 14:698–706.

Debowy DJ, Ghosh S, Gardner EP, Ro JY. 2001. Comparison of neuronal firing rates in somatosensory and posterior parietal cortex during prehension. Exp Brain Res. 137:269–291.

Delhaye BP, Saal HP, Bensmaia SJ. 2016. Key considerations in designing a somatosensory neuroprosthesis. J Physiol. 1–7.

DiCarlo JJ, Johnson KO, Hsiao SS. 1998. Structure of receptive fields in area 3b of primary somatosensory cortex in the alert monkey. J Neurosci. 18:2626–2645.

Dong Y, Mihalas S, Kim SS, Yoshioka T, Bensmaia S, Niebur E. 2013. A simple model of mechanotransduction in primate glabrous skin. J Neurophysiol. 109.

Duque J, Thonnard J, Vandermeeren Y, Sébire G, Cosnard G, Olivier E. 2003. Correlation between impaired dexterity and corticospinal tract dysgenesis in congenital hemiplegia. Brain. 126:732–747.

Flesher SN, Collinger JL, Foldes ST, Weiss JM, Downey JE, Tyler-Kabara EC, Bensmaia SJ, Schwartz AB, Boninger ML, Gaunt RA. 2016. Intracortical microstimulation of human somatosensory cortex. Sci Transl Med. 8:361ra141.

Gardner EP, Ro JY, Debowy D, Ghosh S. 1999. Facilitation of neuronal activity in somatosensory and posterior parietal cortex during prehension. Exp Brain Res. 127:329–354.

Gibson GO, Craig JC. 2006. The effect of force and conformance on tactile intensive and spatial sensitivity. Exp Brain Res. 170:172–181.

Goodman JM, Bensmaia SJ. 2017. A Variation Code Accounts for the Perceived Roughness of Coarsely Textured Surfaces. Sci Rep. 7:46699.

Hikosaka O, Tanaka M, Sakamoto M, Iwamura Y. 1985. Deficits in manipulative behaviors induced by local injections of muscimol in the first somatosensory cortex of the conscious monkey. Brain Res. 325:375–380.

Hiramatsu Y, Kimura D, Kadota K, Ito T, Kinoshita H. 2015. Control of Precision Grip Force in Lifting and Holding of Low-Mass Objects. PLoS One. 10:e0138506.

Iwamura Y, Tanaka M, Sakamoto M, Hikosaka O. 1983. Converging patterns of finger representation and complex response properties of neurons in area 1 of the first somatosensory cortex of the conscious monkey. Exp Brain Res. 51.

Jiang W, Chapman CE, Lamarre Y. 1990. Modulation of somatosensory evoked responses in the primary somatosensory cortex produced by intracortical microstimulation of the motor cortex in the monkey. Exp brain Res. 80:333–344.

Jiang W, Chapman CE, Lamarre Y. 1991. Modulation of the cutaneous responsiveness of neurones in the primary somatosensory cortex during conditioned arm movements in the monkey. Exp Brain Res. 84:342–354.

Johansson RS, Edin BB. 1993. Predictive feed - forward sensory control during grasping and manipulation in man. Biomed Res. 14:95–106.

Johansson RS, Flanagan JR. 2009. Coding and use of tactile signals from the fingertips in object manipulation tasks. Nat Rev Neurosci. 10:345–359.

Johansson RS, Vallbo AB. 1979. Tactile sensibility in the human hand: relative and absolute densities of four types of mechanoreceptive units in glabrous skin. J Physiol. 286:283–300.

Johnson KO. 1974. Reconstruction of population response to a vibratory stimulus in quickly adapting mechanoreceptive afferent fiber population innervating glabrous skin of the monkey. J Neurophysiol. 37:48–72.

Johnson KO, Phillips JR. 1981. Tactile spatial resolution. I. Two-point discrimination, gap detection, grating resolution, and letter recognition. J Neurophysiol. 46:1177–1192.

Kaas JH. 1983. What, if anything, is SI? Organization of first somatosensory area of cortex. Physiol Rev. 63:206–231.

Katz Y, Heiss JE, Lampl I. 2006. Cross-Whisker Adaptation of Neurons in the Rat Barrel Cortex. J Neurosci. 26:13363–13372.

Kim SS, Mihalas S, Russell A, Dong Y, Bensmaia SJ. 2011. Does Afferent Heterogeneity Matter in Conveying Tactile Feedback Through Peripheral Nerve Stimulation? IEEE Trans Neural Syst Rehabil Eng. 19:514–520.

Knibestöl M. 1973. Stimulus-response functions of rapidly adapting mechanoreceptors in the human glabrous skin area. J Physiol. 232:427–452.

Knibestöl M. 1975. Stimulus-response functions of slowly adapting mechanoreceptors in the human glabrous skin area. J Physiol. 245:63–80.

Lamotte RH, Whitehouse J. 1986. Tactile Detection of a Dot on a Smooth Surface: Peripheral Neural Events. J Neurophysiol. Printed in USA. 56.

Lemon RN, Johansson RS, Westling G. 1995. Corticospinal control during reach, grasp, and precision lift in man. J Neurosci. 15:6145–6156.

Mathis MW, Mathis A, Uchida N. 2017. Somatosensory Cortex Plays an Essential Role in Forelimb Motor Adaptation in Mice. Neuron. 93:1493–1503.e6.

Muniak MA, Ray S, Hsiao SS, Dammann JF, Bensmaia SJ. 2008. The neural coding of stimulus of mechanoreceptive afferents with psychophysical behavior (vol 27, pg 11687, 2007). J Neurosci. 28.

Okorokova L., He Q, Bensmaia SJ. 2018. Biomimetic encoding model for restoring touch in bionic hands through a nerve interface. J Neural Eng.

Ostry DJ, Darainy M, Mattar AAG, Wong J, Gribble PL. 2010. Somatosensory plasticity and motor learning. J Neurosci. 30:5384–5393.

Pei Y-C, Hsiao SS, Craig JC, Bensmaia SJ. 2010. Shape invariant coding of motion direction in somatosensory cortex. PLoS Biol. 8:e1000305.

Penfield W, Brain EB-, 1937 U. 1937. Somatic motor and sensory representation in the cerebral cortex of man as studied by electrical stimulation. Brain.

Pons TP, Garraghty PE, Cusick CG, Kaas JH. 1985. A sequential representation of the occiput, arm, forearm and hand across the rostrocaudal dimension of areas 1, 2 and 5 in macaque monkeys. Brain Res. 335:350–353.

Poulos DA, Mei J, Horch KW, Tuckett RP, Wei JY, Cornwall MC, Burgess PR, Evans B, Fisher J, Frederickson G, Skelton V, Reeves C. 1984. The neural signal for the intensity of a tactile stimulus. J Neurosci. 4:2016–2024.

Pubols BH, Pubols LM. 1976. Coding of mechanical stimulus velocity and indentation depth by squirrel monkey and raccoon glabrous skin mechanoreceptors. J Neurophysiol. 39:773–787.

Rajan AT, Boback JL, Dammann JF, Tenore F V, Wester BA, Otto KJ, Gaunt RA, Bensmaia SJ. 2015. The effects of chronic intracortical microstimulation on neural tissue and fine motor behavior. J Neural Eng. 12:066018.

Reed JL, Pouget P, Qi H-X, Zhou Z, Bernard MR, Burish MJ, Haitas J, Bonds AB, Kaas JH. 2008. Widespread spatial integration in primary somatosensory cortex. Proc Natl Acad Sci U S A. 105:10233–10237.

Reed JL, Qi H-X, Kaas JH. 2011. Spatiotemporal properties of neuron response suppression in owl monkey primary somatosensory cortex when stimuli are presented to both hands. J Neurosci. 31:3589–3601.

Reed JL, Qi H-X, Zhou Z, Bernard MR, Burish MJ, Bonds AB, Kaas JH. 2010. Response Properties of Neurons in Primary Somatosensory Cortex of Owl Monkeys Reflect Widespread Spatiotemporal Integration. J Neurophysiol. 103:2139–2157.

Rincon-Gonzalez L, Warren JP, Meller DM, Helms Tillery S. 2011. Haptic Interaction of Touch and Proprioception: Implications for Neuroprosthetics. IEEE Trans Neural Syst Rehabil Eng. 19:490–500.

Ro JY, Debowy D, Ghosh S, Gardner EP. 2000. Depression of neuronal firing rates in somatosensory and posterior parietal cortex during object acquisition in a prehension task. Exp Brain Res. 135:1–11.

Saal HP, Delhaye BP, Rayhaun BC, Bensmaia SJ. 2017. Simulating tactile signals from the whole hand with millisecond precision. Proc Natl Acad Sci U S A. 114:E5693–E5702.

Saal HP, Harvey MA, Bensmaia SJ. 2015. Rate and timing of cortical responses driven by separate sensory channels. Elife. 4:e10450.

Säfström D, Edin BB. 2008. Prediction of object contact during grasping. Exp Brain Res. 190:265–277.

Salimi I, Brochier T, Smith AM. 1999. Neuronal Activity in Somatosensory Cortex of Monkeys Using a Precision Grip. I. Receptive Fields and Discharge Patterns. J Neurophysiol. 81:825–834.

Schabrun SM, Ridding MC, Miles TS. 2008. Role of the primary motor and sensory cortex in precision grasping: a transcranial magnetic stimulation study. Eur J Neurosci. 27:750–756.

Simons SB, Tannan V, Chiu J, Favorov O V, Whitsel BL, Tommerdahl M. 2005. Amplitude-dependency of response of SI cortex to flutter stimulation. BMC Neurosci. 6:43.

Sripati AP, Yoshioka T, Denchev P, Hsiao SS, Johnson KO. 2006. Spatiotemporal Receptive Fields of Peripheral Afferents and Cortical Area 3b and 1 Neurons in the Primate Somatosensory System. J Neurosci. 26:2101–2114.

Sur M, Wall JT, Kaas JH. 1981. Modular Segregation of Functional Cell Classes within the Postcentral Somatosensory Cortex of Monkeys. Science (80).

Tabot GA, Dammann JF, Berg JA, Tenore F V, Boback JL, Vogelstein RJ, Bensmaia SJ. 2013. Restoring the sense of touch with a prosthetic hand through a brain interface. Proc Natl Acad Sci U S A. 110:18279–18284.

Tanan V, Whitsel BL, tommerdahl M. 2006. Vibrotactile adaptation enhances spatial localization. Brain Res. 1102:109–116.

Thakur PH, Fitzgerald PJ, Lane JW, Hsiao SS. 2006. Receptive field properties of the macaque second somatosensory cortex: nonlinear mechanisms underlying the representation of orientation within a finger pad. J Neurosci. 26:13567–13575.

Vega-Bermudez F, Johnson KO. 1999. Surround suppression in the responses of primate SA1 and RA mechanoreceptive afferents mapped with a probe array. J Neurophysiol. 81:2711–2719.

Vega-Bermudez F, Johnson KO, Hsiao SS. 1991. Human tactile pattern recognition: active versus passive touch, velocity effects, and patterns of confusion. J Neurophysiol. 65:531–546.

Wannier TM, Maier MA, Hepp-Reymond MC. 1991. Contrasting properties of monkey somatosensory and motor cortex neurons activated during the control of force in precision grip. J Neurophysiol. 65:572–589.

Wannier TMJ, Töltl M, Hepp-Reymond M-C. 1986. Neuronal activity in the postcentral cortex related to force regulation during a precision grip task. Brain Res. 382:427–432.

Williams SR, Chapman CE. 2002. Time Course and Magnitude of Movement-Related Gating of Tactile Detection in Humans. III. Effect of Motor Tasks. J Neurophysiol. 88:1968–1979.

Witney AG, Wing A, Thonnard J-L, Smith AM. 2004. The cutaneous contribution to adaptive precision grip. Trends Neurosci. 27:637–643.

Xerri C, Merzenich MM, Peterson BE, Jenkins W. 1998. Plasticity of primary somatosensory cortex paralleling sensorimotor skill recovery from stroke in adult monkeys. J Neurophysiol. 79:2119–2148.

Yau JM, Connor CE, Hsiao SS. 2013. Representation of tactile curvature in macaque somatosensory area 2. J Neurophysiol. 109:2999–3012.

Yau JM, Kim SS, Thakur PH, Bensmaia SJ. 2016. Feeling form: the neural basis of haptic shape perception. J Neurophysiol. 115:631–642.

Chapter 5 | Methodological Considerations for a Chronic Neural Interface with the Cuneate Nucleus of Macaques[5]

While the response properties of neurons in the somatosensory nerves and anterior parietal cortex have been extensively studied, little is known about the encoding of tactile and proprioceptive information in the cuneate nucleus (CN) or external cuneate nucleus (ECN), the first recipients of upper limb somatosensory afferent signals. The major challenge in characterizing neural coding in CN/ECN has been to record from these tiny, difficult to access brainstem structures. Most previous investigations of CN response properties have been carried out in decerebrate or anesthetized animals, thereby eliminating the well-documented top-down signals from cortex, which likely exert a strong influence on CN responses. Seeking to fill this gap in our understanding of somatosensory processing, we describe an approach to chronically implant arrays of electrodes in the upper limb representation in the brain stem in primates. First, we describe the topography of CN/ECN in Rhesus macaques, including its somatotopic organization and the layout of its submodalities (touch and proprioception). Second, we describe the design of electrode arrays and the implantation strategy to obtain stable recordings. Third, we show sample responses of CN/ECN neurons in brainstem obtained from awake, behaving monkeys. With this method, we are in a position to characterize, for the first time, somatosensory representations in CN and ECN of primates.

[5] This chapter is part of a publication: Suresh AK, Winberry JE, Versteeg C, Chowdhury R, Tomlinson T, Rosenow JM, Miller LE, Bensmaia SJ. 2017. Methodological considerations for a chronic neural interface with the cuneate nucleus of macaques. Journal of Neurophysiology 118:3271–3281

5.1 | Introduction

A central question in neuroscience is how sensory representations are transformed as they ascend the neuraxis. In primates, the coding of tactile and proprioceptive information has been extensively studied in the nerve and in anterior parietal cortex (APC), which encompasses Brodmann's areas 3a, 3b, 1 and 2. Sensory representations in APC differ from those at the periphery in several important ways. First, while cutaneous and proprioceptive nerve fibers can be classified into a small number of submodalities, each responding to a different aspect of skin or muscle/tendon stimulation, individual APC neurons integrate sensory signals from multiple submodalities (Prud'homme and Kalaska 1994; Saal and Bensmaia 2014a). Second, APC responses tend to respond selectively to behaviorally relevant stimulus features, while their peripheral counterparts are more ambiguous (Bensmaia et al. 2008; Harvey et al. 2013b). In the context of proprioceptive responses, cortical neurons convey complex information about limb state compared to peripheral afferents (Costanzo and Gardner 1981; Gardner and Costanzo 1981; London et al. 2011; London and Miller 2013). Little is known about the coding of upper limb tactile and proprioceptive information in brainstem nuclei and the ventroposterior nucleus of the thalamus. Here, we discuss methodological issues associated with recording from the cuneate nucleus (CN) and external cuneate nucleus (ECN) of awake primates using chronically implanted electrode arrays (see also Richardson et al. 2015, 2016) and discuss preliminary results on the response properties of CN/ECN neurons in awake primates.

Recording from the CN/ECN of awake primates may offer key insights into sensorimotor representations of the upper limb. First, while CN responses are modulated by descending

cortical input (Andersen et al. 1962, 1964a), the properties of CN neurons have been almost exclusively studied in anesthetized or decerebrate cats (Andersen et al. 1964b; Andersen et al. 1964; Jabbur and Banna 1968; O'Neal and Westrum 1973; Canedo et al. 2000; Hayward et al. 2014; Jörntell et al. 2014) whose descending input is thus abolished. To the extent that the sensory response properties of CN neurons are shaped by this descending input, then, studies of these properties without this input may be misleading.

Second, it is unclear to what extent neural coding in cat CN/ECN will resemble its primate counterpart because cats and primates use their upper limbs in different ways, especially their paws/hands. In fact, the morphological organization and mechanisms of synaptic processing differ between primates and cats (Harris et al. 1965; Biedenbach et al. 1971; Molinari et al. 1996), highlighting the need to repeat in non-human primates studies conducted in cats to understand the organization, response properties, and circuitry in primates. Furthermore, while ECN of cats projects solely to the cerebellum, ECN of primates also projects to the ventral posterolateral nucleus of the thalamus (Boivie and Boman 1981). The functional implications of this divergence have yet to be determined.

In the present study, we first established the somatotopic and submodality (cutaneous vs. proprioceptive) topography of CN/ECN in anesthetized Rhesus macaques using a standard electrode microdrive. Although anatomical tracing studies have been carried out in various non-human primates (*Otolemur garnetti, Aotus trivirgatus, Saimiri sciureus*, *Macaca radiate, Macaca mulatta)* (Hummelsheim and Wiesendanger 1985; Florence et al. 1988; Qi and Kaas 2006), somatotopic electrophysiological mapping has not been reported and the precise location and extent of the nuclei, necessary for a chronic implant, were not

provided. Second, we developed and deployed an approach to chronically implant electrode arrays in CN/ECN, which allowed us to record the responses of CN/ECN neurons in awake, behaving macaques. Third, we characterized the stability of the neuronal signals measured through the electrode arrays and the stability of the receptive fields (RFs). These results build a foundation towards exploring, for the first time, tactile and proprioceptive coding in the CN and ECN of intact, awake, and behaving animals.

5.2 | Results

We characterized the topographical organization of somatosensory brainstem nuclei (cuneate/external cuneate, gracile and trigeminal) in acute experiments and estimated the coordinates for chronic array implantation targeting the cutaneous or proprioceptive representations of the upper limb. Without histological confirmation, we could not distinguish between CN and ECN as neurons in both nuclei exhibit similar proprioceptive responses, though ECN has been shown to contain a preponderance of proprioceptive neurons (Hummelsheim and Wiesendanger 1985; Hummelsheim et al. 1985; Witham and Baker 2011; Niu et al. 2013). In parallel, we modified the design of electrode arrays and the implantation approach to improve their stability and longevity.

5.2.1 Location and topographic organization of the cuneate nucleus

During acute recordings, we monitored multiunit activity from 90 distinct sites in CN/ECN, 13 in gracile nucleus, and 9 in trigeminal nucleus. Proprioceptive and, especially, tactile responses were most discernable when electrode impedance was greater than 1 MΩ. Our main goal was to characterize the topography of the upper limb representation in CN/ECN. Data used to generate the response maps were pooled across the left and right brainstems

of two animals (two sides from one animal, one from the other). While we strived for a consistent coordinate system across experiments, differences in surface curvature, electrode angle, and neck flexion angle may have caused some distortion in the resulting maps of the brainstem.

5.2.2 Borders of the observed brainstem nuclei

Our first goal was to determine the medio-lateral extent of the CN/ECN by finding the medial border with the gracile nucleus and the lateral border with the trigeminal nucleus relative to midline. Figure 5.1A illustrates the position of upper limb (CN/ECN), lower limb (gracile), or face units (trigeminal). The gracile nucleus spans the first 1.25-1.5 mm lateral to midline, the CN/ECN the following 1.5-1.75 mm, and the trigeminal nucleus spans the remaining 1 mm. The medio-lateral extent of these structures remains fairly constant along the rostro-caudal axis (within a range of ±3mm from obex) as well as in depth. These findings are consistent with previous anatomical studies of primate brainstem nuclei (Figure 5.1C illustrates the relative positioning of these nuclei in lower brainstem, see also Mai and Paxinos 2011).

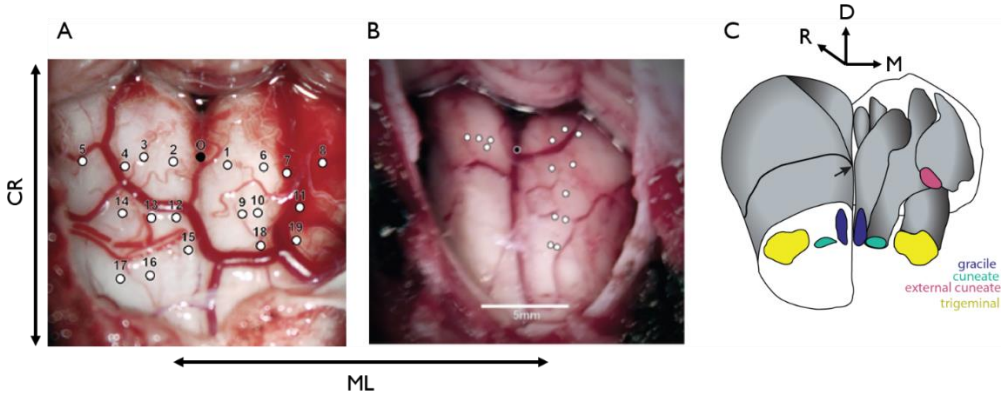

Figure 5.1. Surgical Exposure for two acute procedures.

Figure 5.1, continued. Each white circle represents a penetration site: CR (caudal-rostral), ML (medio-lateral), D (dorsal) A| First acute experiment, using low impedance (0.5 MOhms) electrodes, whose goal was to determine the boundaries of gracile, cuneate, and trigeminal nuclei. B| Second acute experiment using higher impedance electrodes (1-4MOhms), in which we targeted primarily the right hemisphere to understand submodality organization and somatotopy. Black circle denotes the obex. Cerebellar tonsils are located at the top in both images. C| A reconstructed 3D view of the lower brainstem, and relative positioning of the gracile nucleus (dark blue), cuneate nucleus (light blue), external cuneate nucleus (pink), and trigeminal nucleus (yellow). The black arrow is pointing towards obex.

5.2.3 Response modality

Next, we aimed to characterize the organization of proprioceptive and cutaneous inputs to CN/ECN and estimate the location of the boundary between the two nuclei. We found that proprioceptive units tended to be more superficial than cutaneous ones, and more frequently caudal to obex (Figure 5.2B,C). Additionally, proprioceptive units tended to be more lateral (mean distance from obex: 2.2mm, range: 1mm-3.3mm) than their tactile counterparts (mean: 2.1, range: 1mm-2.7mm), in part because the ECN is dominated by proprioceptive responses and is located more laterally.

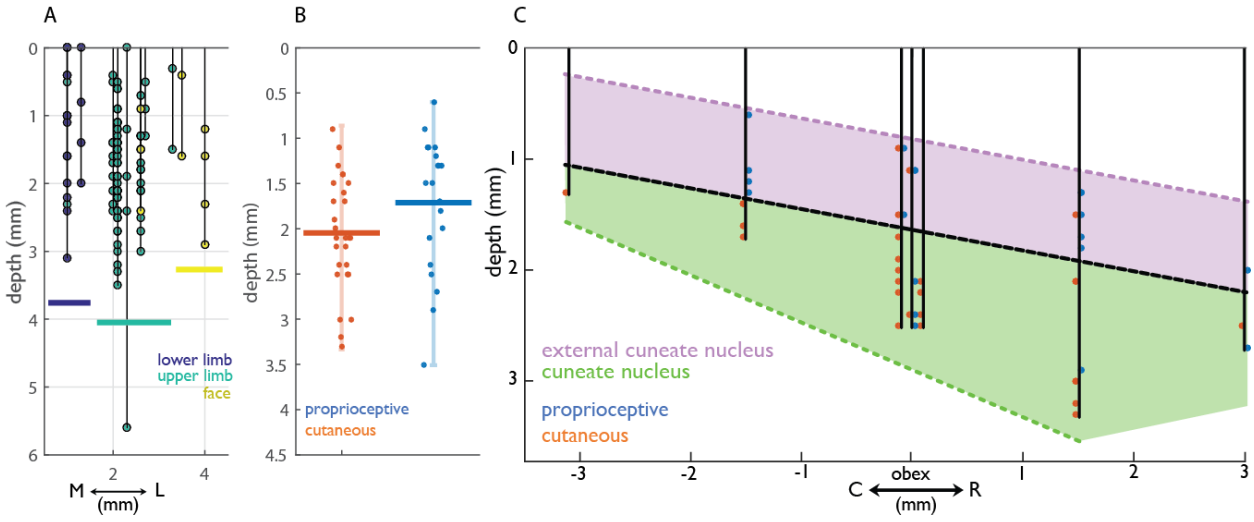

Figure 5.2| Topography of the observed brainstem nuclei.

Figure 5.2, continued. A| RF as a function of depth and medio-lateral position of the electrode tip. RFs on the lower limb (gracile) are coded in dark blue, upper limb (cuneate/external cuneate) in light blue, and face (trigeminal) in yellow. The medial and lateral borders of the upper limb units are about 1.5 and 3 mm from the midline respectively. B| Distribution of distances from the neural tissue surface for cutaneous and proprioceptive units of cuneate and external cuneate neurons. Cutaneous units tended to be deeper than proprioceptive ones. Vertical bars span the range of observed depths and horizontal bars their mean. C| Diagram of several electrode penetrations made along the rostro-caudal and dorsal-ventral (depth) axis. Black dotted line represents estimated boundary between ECN and CN, with ECN shaded in purple (proprioceptive) and CN shaded in green (majority cutaneous).

We estimated the boundary between the ECN (majority proprioceptive) and CN (both cutaneous and proprioceptive) along the dorsal-ventral and rostro-caudal axis (Figure 5.2C). We also estimated the lateral boundary between CN and ECN to be located at ~2.7 mm, since no tactile units were observed beyond this point. These findings are consistent with previous studies in macaques and other primates (Figure 5.1C) showing that ECN is located dorsal to CN, and extends ~2mm from obex in each direction along the rostro-caudal axis (Hummelsheim and Wiesendanger 1985; Hummelsheim et al. 1985; Florence et al. 1988; Qi and Kaas 2006).

In summary, then, gradients of submodality composition (tactile vs. proprioceptive) were most pronounced along the rostro-caudal axis and the dorsal-ventral axis (depth), as might be expected given that these define the boundary between CN and ECN (Figure 5.2C). Tactile units were most frequently observed ~2mm lateral to obex at a depth of 2mm or greater. Proprioceptive units were observed relatively uniformly across the rostro-caudal axis (±2mm to obex), but most frequently observed superficially.

5.2.4 Somatotopic organization of proprioceptive and cuneate units

Units with proximal cutaneous RFs tended to be located more superficially than those with distal ones (Figure 5.3A,B,C). The mean depth of units with RFs proximal to the elbow was approximately 1.5 mm (range of 0.6 - 2.9 mm) whereas that of units with RFs distal to the elbow was 2.4 mm (range of 1.2 - 3.5mm), consistent with previous findings in other primates (Florence et al. 1988; Qi and Kaas 2006). A topographic progression was also observed along the rostro-caudal axis: units with distal RFs tended to be more rostral to the obex (with a mean location of -0.6 mm and a range of -3.0 to 1.5 mm) while units with proximal RFs tended to be caudal (0.6 mm with a range of -1.5 to 3.0mm) (Figure 5.3D,E,F). Somatotopic organization was similar for tactile and proprioceptive units both in depth and along the rostro-caudal axis.

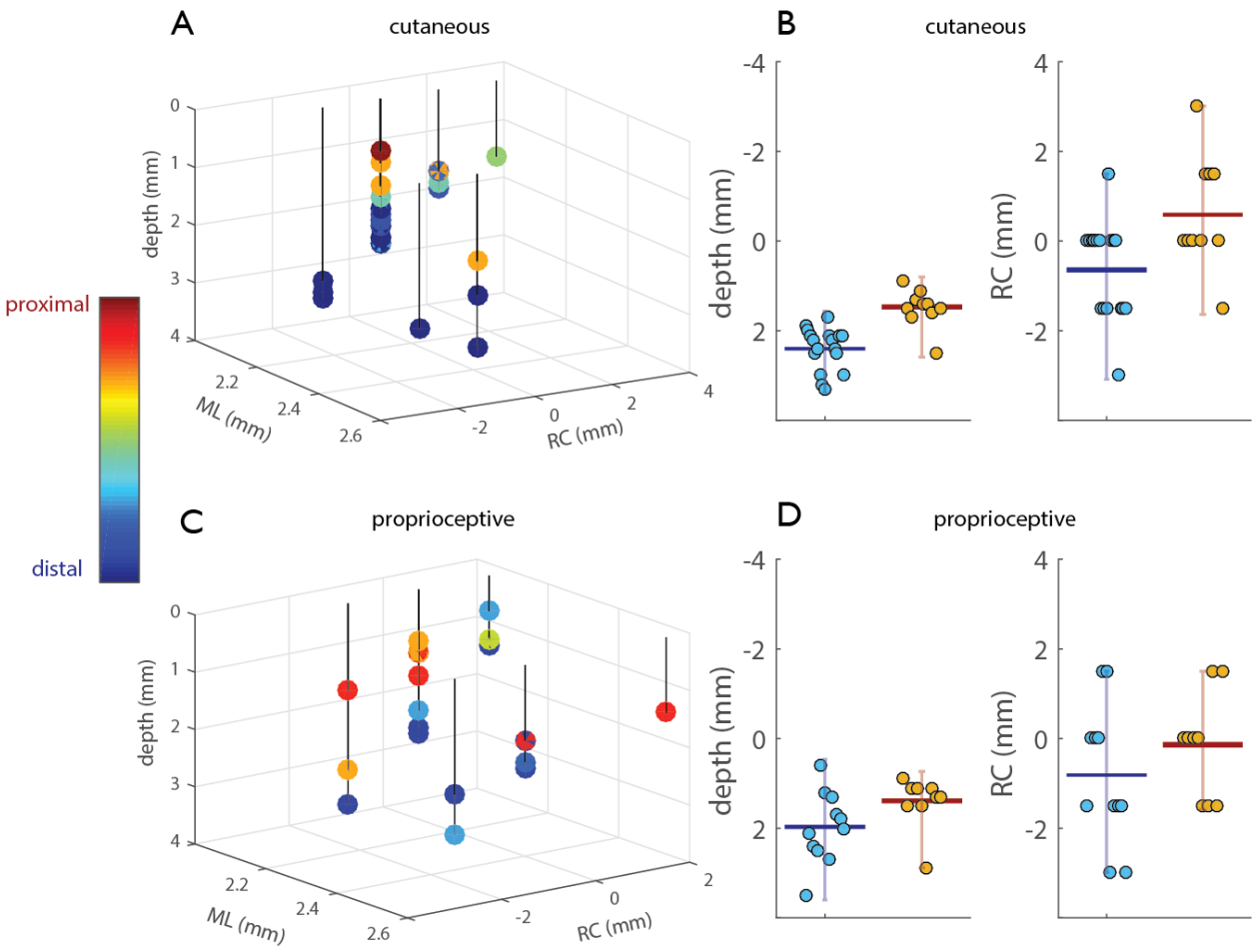

Figure 5.3. Somatotopic organization of CN.

A|3D diagram of penetrations with cutaneous RFs plotted with respect to obex and the surface. Color bar indicates the RF location. ML: medio-lateral, RC: rostro-caudal. B|Summary of cutaneous results: (Left) distal units tend to be deeper than proximal ones. Horizontal bar represents mean values, and vertical bars span the range of values. (Right) distal units tend be more cranial (negative along the RC dimension) than proximal ones. The forearm served as the boundary between distal and proximal units in the bar plots. C| 3D diagram of penetrations with proprioceptive responses with respect to obex and the surface. Color bar indicates RF location. D|Summary of proprioceptive results: (Left) distal units tend to be deeper than proximal ones. (Right) Distal units tend to be anterior to their proximal counterparts. Overall, both proprioceptive and cutaneous modalities exhibited similar somatotopic trends: proximal units were located more superficially and more posterior to the obex than distal ones.

5.2.5 Array performance

In total, we placed 13 arrays (4 UEAs and 9 FMAs) into the brainstem nuclei of 11 macaques (two monkeys were implanted bilaterally in separate surgeries). The design of the arrays and the implantation procedure evolved over time and the success rate improved progressively. Four arrays (2 UEAs and 2 FMAs) yielded strong single-unit signals, which allowed us to collect information about the stability of RF locations over the course of the arrays' lifespans. Of the remaining arrays, four FMAs and one UEA yielded signals that were either limited to a few electrodes, of poor quality, and/or of short lifespan. We were not able to record any signals from the remaining arrays due to health complications (3/9) or complete array failure (1/9). Figure 5.4C shows the approximate locations of each array on the brainstem.

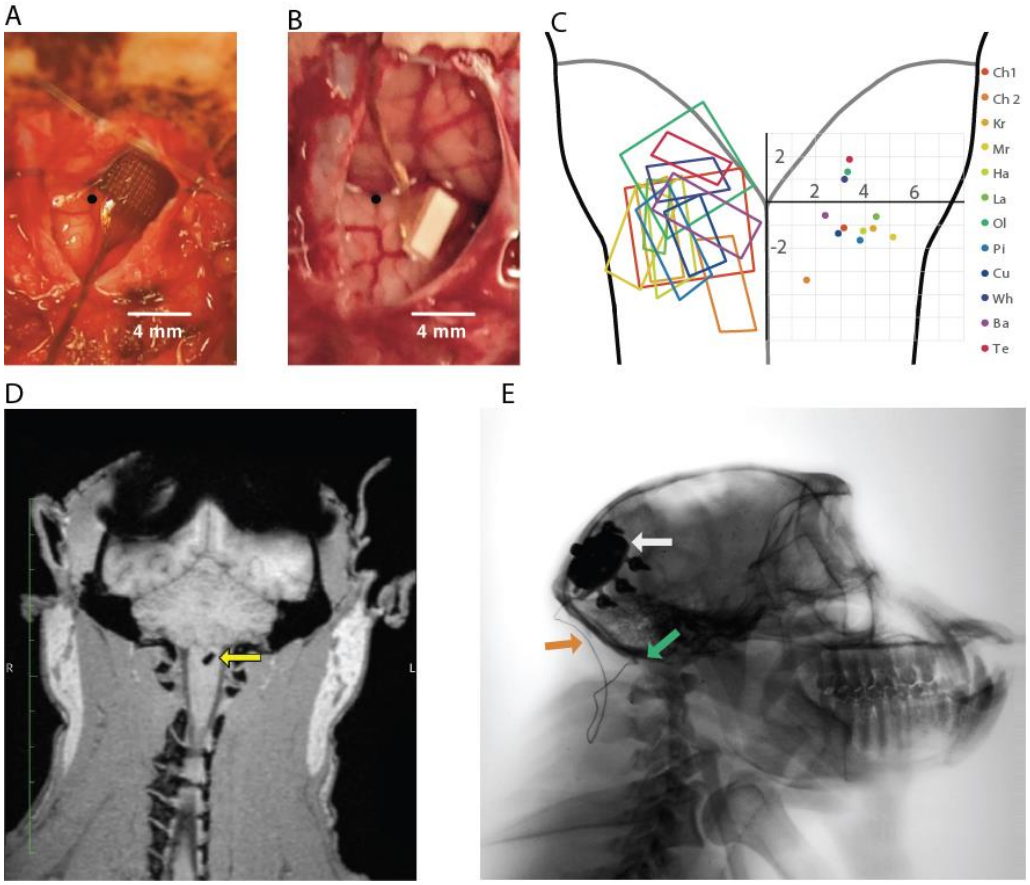

Figure 5.4 | Chronic Implants

A,B| Examples of an implanted UEA (A, animal Ol) and FMA (B, animal Pi). Obex is indicated by the black circle. C| Left: Approximate location of each array implant shown on a diagram of the brainstem. Right: Coordinates of the center of each array. Array locations are all shown on the same hemisphere for visualization purposes. D| 3D MRI scan 5 weeks post-implantation shows the FMA array (yellow arrow) in the brainstem of animal Ba. E| Sagittal X-ray of animal Cu shows the pedestal (white arrow), leads (orange arrow), and FMA array (green arrow) 6 weeks post-implant.

5.2.6 FMA Design

An advantage of FMAs is that the electrode length, material, and configuration, as well as the lead length and pedestal shape can be specified on an array-by-array basis. We found that arrays whose leads were manufactured with steel (rather than the standard gold) and reinforced with a thin silicone coating around the wire bundle exhibited longer lifespans. Only TE received an array with steel wires and silicone cable reinforcements, and this array

had a signal longevity of 6 months, while all other FMAs lasted 8 weeks or less. Unlike implantation in cortex, for which movement between pedestal and array is relatively limited, brainstem implants move substantially relative to the pedestal, thereby stressing the leads (Fuchs and Luschei 1970; Hoffman et al. 1981; Buford and Davidson 2004). Moreover, the lead traverses neck muscles that are constantly flexing and extending, creating additional stress. Lead breakage was the most likely failure mode for many of our initial FMA implants.

We found that lengths of 7-9 cm were optimal for the leads in that sufficient slack was provided for movement, but not so much excess lead to adhere to muscle and other tissue (assuming that the more foreign material is implanted in the tissue, the more opportunity for adhesion). We began our studies with longer leads (up to 14 cm), and initially shortened the leads to facilitate implantation of the array during surgery. During vacuum insertion, longer cables impose more torque on the array while lowering electrodes into neural tissue, ultimately destabilizing the array during implantation. Shortening the cable not only led to easier insertion but also improved signal longevity (monkeys WH, BA, LA1, HA). After several iterations, we converged onto specifications that yielded long lasting arrays in brainstem: shorter, silicone reinforced cables made of steel wire. TE received an array with all three design features, and signal longevity on this array substantially improved compared to all other FMA implants (Table 1). Although we did not have the same design options available with the UEAs, these arrays seem to be less susceptible to lead breakage, perhaps because of the greater number of individual leads, which results in a stronger aggregate cable.

Table 5-1: Array specifications for each animal.

Monkey ID	Array Type	Size (mm)	Electrode lengths	Manufacturing Impedance	Array Signal Longevity	Likely failure mode
WH	FMA HD	1.6 x 2.95	2.0-2.5 mm	0.5-0.9 MOhms	6 weeks	Wire bundle failure
TE	FMA HD	1.6 x 2.95	2.0-2.5 mm	0.3-1.1 MOhms	6 months	Wire bundle failure
PI	FMA SD	1.8 x 4	1.5-2.0 mm	0.4-0.7 MOhms	6 weeks	Wire bundle failure
BA	FMA SD	1.8 x 4	2.0-2.5mm	0.7-1.1 MOhms	3 weeks	Wire bundle failure
CU	FMA HD	1.6 x 2.95	2.0-2.5mm	0.4-1.0 MOhms	N/A	Fluid leakage
CH2	FMA SD	1.6x 2.8	1.5-3.0 mm	0.08-1.5 MOhms	<1 week	Array manufacturing defect
KR	FMA SD	1.8x 4.0	1.0-2.0 mm	0.3- 1 MOhms	2 weeks	Array came out
MR	FMA HD	1.6x 2.8	1.25- 2.5 mm	0.6- 1.3 MOhms	N/A	Array did not insert
HA	FMA SD	1.8x 4.0	1.0-2.25 mm	0.5-1.0 MOhms	6 weeks	Wire bundle failure
LA1	FMA HD	1.6x 2.8	1.0-2.5 mm	0.5-1.0 MOhms	2 months	Wire bundle failure
OL	Utah	4.0x 4.0	1.5 mm	0.3-0.8 MOhms	1 day	Meningoencephalitis
LA2	Utah	4.0x4.0	1.5 mm	0.1-0.8 MOhms	>6 months	N/A
CH1	Utah	4.0 x 4.0	1.3 mm	0.2-0.8 MOhms	<1 week	Array came out

5.2.7 RF stability and array longevity

First, we characterized the location of each electrode's RF in each of two FMAs over the lifetime of the arrays. Specifically, we counted the number of days over which each channel was activated by the same skin location or same joints (Figure 5.6A). The majority of upper limb units remained stable for only 1 or 2 days suggesting significant turnover of neuronal units from day to day. Qualitative assessment of the stability of the longest lasting UEA suggests that RFs may be more stable in these arrays. Note, however, that proximal RFs are larger than their distal counterparts so differences in RF location – indicative of different units – may be more difficult to identify for proximal than for distal representations.

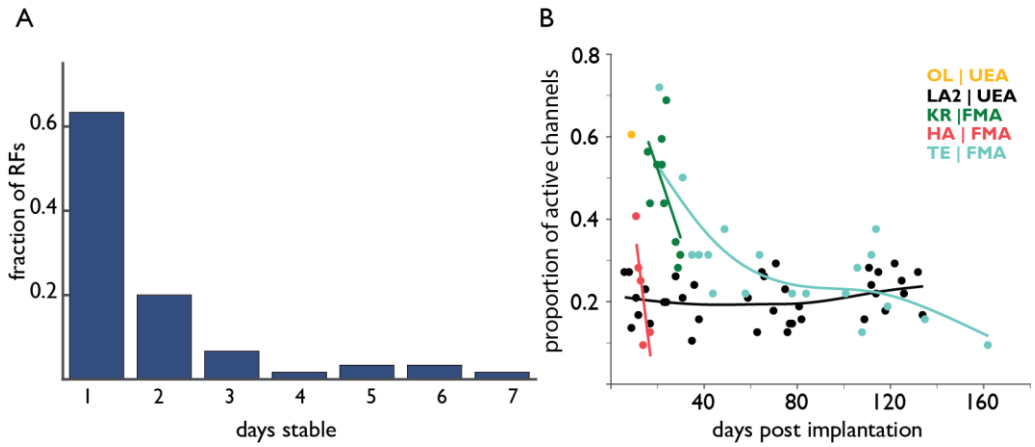

Figure 5.5| Electrode and receptive field stability.

A| Number of consecutive days that observed RFs remained stable for each array. Channel RFs tended to remain stable for 1 or 2 days, with a maximum of 7 days. These data were collected over 20 sessions across two monkeys (WH and TE), whose distributions were very similar. B| Array Longevity for five electrode arrays. Points represent number of sorted neurons recorded after array implantation. Early implants (KR, HA) degraded rapidly after initial implantation. Longevity of LA(2), TE improved, as measured by number of units. One subject, OL (yellow), developed a fatal case of acute meningoencephalitis.

Second, we characterized the number of channels that yielded discernible units over the lifetime of each array as a gauge of signal stability and array longevity. By this measure,

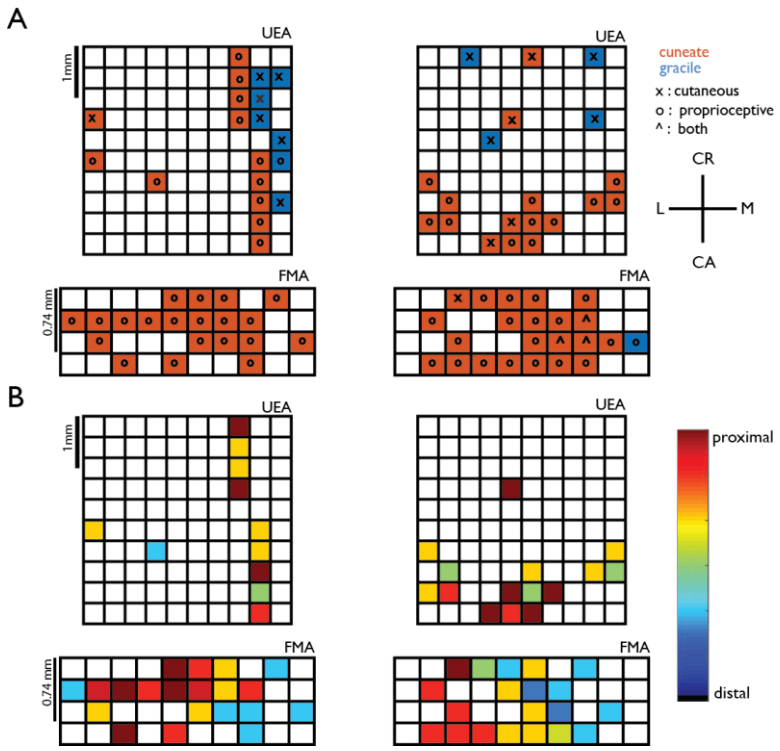

Figure 5.6 | Topographical organization of the brainstem inferred from array recordings.

A| Receptive field locations (M medial, L lateral, CR cranial, CA caudal) of electrodes in 2 UEAs and 2 FMAs, identified by anatomical location and modality. Most units had RFs on the upper limb (as expected since we targeted CN) and responded to proprioceptive stimulation. B| Somatotopy of upper limb proprioceptive units observed on each array. Utah arrays do not show a somatotopic trend, while FMAs show a medio-lateral trend. Distal units are observed medially, while proximal units are observed laterally. Overall, chronic arrays are able to capture proprioceptive cuneate nucleus responses (ECN), but due to the depth and/or insertion of these electrodes, relatively few cutaneous responses (CN) were observed.

modifications to the arrays and to the insertion procedure led to significantly improved longevity (5.5B). The more recent implants yielded units for up to 6 months whereas early arrays failed within days or weeks (5.5B). The improved longevity can be attributed to

improvements in FMA design as described above, and to modifications to the surgical procedure to include an adhesive that prevented arrays from being expelled from the brainstem. For both UEAs and FMAs, we found that applying Vetbond yielded more stable arrays than did Tisseel. TE (FMA), and LA1 (UEA) had Vetbond applied to the array post-insertion, and these arrays were functional for the longest period of time (Table 1).

5.2.8 Single unit responses

Figure 5.6 shows the topography of the brainstem inferred from the chronically implanted electrode arrays. Observed topographies were broadly consistent with those in the acute experiments. Figure 5.7 shows the responses of a cutaneous unit in CN to vibratory stimuli that varied in frequency and amplitude. This unit exhibits phase locking – i.e., produces a spike or a burst of spikes within a restricted portion of each stimulus cycle – as has been shown in both tactile nerve fibers (Talbot et al. 1968) and S1 neurons (Harvey et al. 2013a). The frequency response profile of this unit suggests that it receives input from Pacinian afferents. Indeed, it peaks in sensitivity at around 250-300 Hz, as do Pacinian fibers. Interestingly, however, this unit also exhibits a sustained response to a skin indentation, a property that is only observed in slowly adapting type 1 fibers. This combination of response properties suggests that signals from multiple submodalities converge onto individual neurons in CN (see Saal and Bensmaia 2014b for a review).

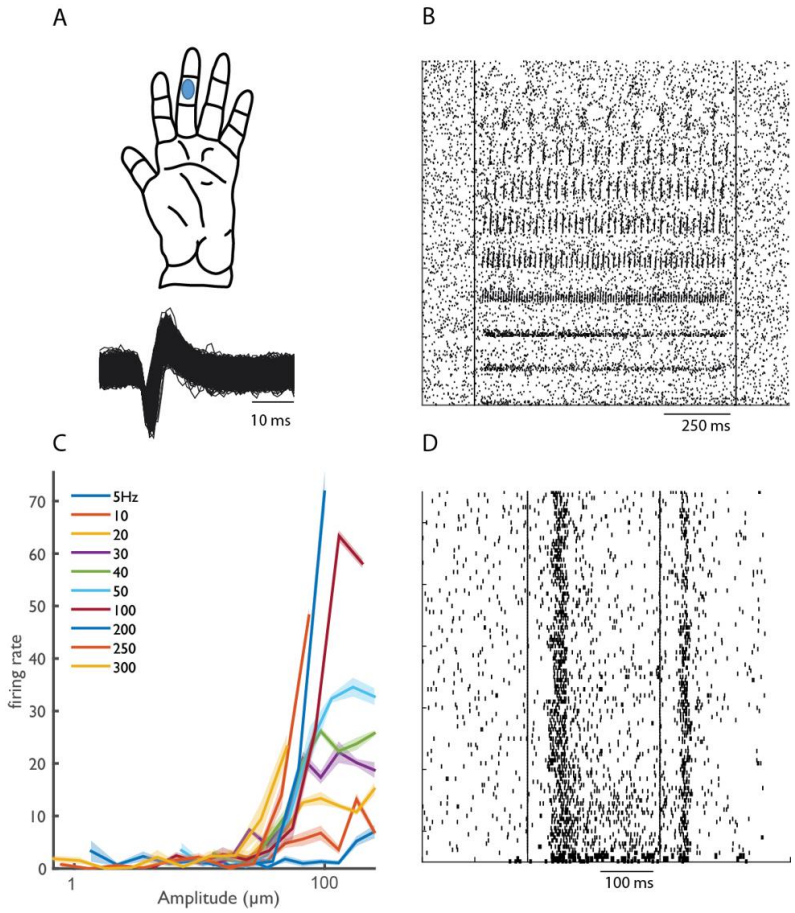

Figure 5.7 | Responses of a cutaneous unit in CN.

A|(Top) Receptive field center. (Bottom) Waveforms of identified action potentials. B| Responses of a CN neuron to vibrations delivered to the RF. C| Rate-intensity relationship demonstrates that this neuron's responses are frequency-dependent and peak in sensitivity at around 300 Hz, similarly to PC fibers. D| Responses of the same neuron to indentations delivered to different locations on the index fingerpad. Responses comprise both a sustained component and a strong off component: the sustained response indicates input from slowly adapting fibers and the off response indicates input from rapidly adapting fibers.

5.3 | Discussion

Topography of the Somatosensory Brainstem Nuclei

While the organization of the somatosensory brainstem nuclei in primates has been documented in previous studies (Florence et al. 1988; Qi and Kaas 2006), our study is the

first to characterize the topographical organization of these nuclei in rhesus macaques. We find that proprioceptive units tend to be more superficial than cutaneous ones and that the CN/ECN exhibit a somatotopy both in depth and along the rostro-caudal axis: units with RFs on the proximal limb tend to be more superficial and caudal than those with distal RFs. The dorsal-ventral trends observed in rhesus macaques with regards to somatotopy and submodality distribution match those reported for other macaque species (Florence et al. 1989; Qi and Kaas 2006), with the additional observation of somatotopic trends along the rostro-caudal or medio-lateral axes.

In the FMA recordings, we noticed a distal to proximal trend of RFs along the medio-lateral axis. That is, units with distal RFs tended to be located medially while units with proximal RFs were predominantly located laterally. This somatotopy was observed neither in the anesthetized acute experiments, nor in the UEA RF maps, and may be attributed to the curvature of the brainstem, which caused medial electrodes to penetrate deeper than others.

Implications of the topography for chronic implants

To record from digit-related units in CN is challenging due to their depth and their location rostral to the obex, which can be partially obstructed by the cerebellum. Electrode arrays must include long (>2mm) electrodes yet still allow insertion in a far rostral position along the brainstem. Unfortunately, the angle for this insertion is often hindered by the occipital bone, even after a wide suboccipital craniectomy that extends to the transverse sinuses. Proprioceptive units with proximal RFs are more easily accessible given their superficiality and caudal location.

The boundary between CN and ECN is difficult to establish conclusively based on electrophysiological response properties because both nuclei exhibit similar proprioceptive responses (Hummelsheim et al. 1985; Witham and Baker 2011). Any implant is likely to impinge on the two nuclei given their small size, and histology will almost certainly be necessary to distinguish them post hoc.

Array design considerations

The primary failure mode for FMAs was likely lead breakage. Indeed, the manner in which signals decayed and subsequently failed over time suggest that lead breakage, as opposed to electrode or pedestal/connector breakage, primarily contributed to array failure.

UEAs offer the advantage of greater coverage, more and more closely spaced electrodes, and strong leads. However, targeting cutaneous units requires longer electrodes than are currently commercially available with UEAs. Furthermore, the insertion technique for FMAs, which involves a narrow vacuum probe, facilitates rostral positioning relative to its UEA counterpart, as the pneumatic inserter required for the latter has a wider footprint. Given the rostral position of cutaneous digit, this further favors FMAs over UEAs for studies involving the cutaneous representations of the digits.

Stability of cutaneous receptive fields

That the location of RFs turn over at a relatively rapid rate for the FMA implants (every other day approximately) suggests movement of the array within the tissue. The great stability of our most recent UEA implants is difficult to explain, unless the much greater number and density of electrodes helped to stabilize the array within the tissue. While cortical implants with either FMAs or UEAs also exhibit some neuronal turn over, its rate

is much slower, with some units remaining stable for weeks or even months (Vaidya et al. 2014). The poor stability of CN implants can be attributed to the much greater mobility of the brain stem, which flexes during neck movements, a degree of freedom not present in cranial implants (Fuchs and Luschei 1970; Hoffman et al. 1981; Buford and Davidson 2004).

Conclusions

We have developed a strategy to record stably for single sessions from the somatosensory brainstem nuclei using chronically implanted electrode arrays. We have characterized the somatotopic and functional topography of neurons in the CN/ECN using electrophysiology, and illustrated the firing rate characteristics of several neurons in response to passive RF manipulation. Although stereotaxic coordinates cannot offer well-defined boundaries between somatosensory brainstem nuclei due to various confounding factors, the observed topographical trends will inform future array placement and design. Vibratory responses have been extensively characterized in the periphery and cortex of rhesus macaques (Mountcastle et al. 1967; Johnson and Lamb 1981; Muniak et al. 2008; Harvey et al. 2013b), as have responses to passive and active limb movements. The ability to collect single unit data from the CN of awake behaving primates will provide us with an opportunity to understand how these limb state representations are transformed as they ascend the neuraxis. We may also begin to understand the nature and function of the top-down modulation CN receives from cortex.

5.4 | Methods

5.4.1 Surgical approach for acute mapping procedures

All experimental protocols complied with the guidelines of the University of Chicago Animal Care and Use Committee, the Northwestern University Animal Care and Use Committee, and the National Institutes of Health Guide for the Care and Use of Laboratory Animals. Surgical anesthesia was induced with ketamine HCl (3 mg/kg, i.m.) and dexmedetomidine (75 μg/kg), and maintained with Isoflurane (1%). The animal's head was held in a stereotaxic frame, and positioned such that its neck was flexed approximately 75 degrees relative to the trunk. First, we made a midline incision from the occipital bone to approximately segment C3. Using cautery, we divided the posterior cervical muscles along the midline raphe and removed them from the occipital bone and the posterior ring of segment C1 in a subperiosteal plane. Next, we exposed the foramen magnum and the occipitocervical dura between C1 and the foramen using a combination of gentle monopolar cautery and sharp dissection. Excess soft tissues were removed to expose clean dura. We enlarged the foramen magnum cranially and laterally using Kerrison rongeurs and excised the dura to provide access to the brain stem both cranially and caudally relative to the obex. We made single electrode penetrations at various depths within the exposed brainstem (Digure 5.1).

5.4.2 Surgical approach for chronic array implants

We followed a similar procedure for the chronic array implants as for the acute experiments, with a few exceptions. First, prior to the skin incision, we determined the optimal location for the array pedestal, taking into account skin healing and vulnerability to damage. We also considered the routing of the array lead between pedestal and brain

stem, allowing for 1-2 cm of slack for neck movement after the animal woke up. Second, while exposure was similar to that in the acute experiments, the dura over the posterior fossa was opened with a midline linear incision, with the leaves tented back with 6-0 Prolene suture (Ethicon, Somerville, New Jersey). Third, before opening the dura, the pedestal was secured to the skull with bone screws, rostral to the occiput.

We implanted Utah Electrode Arrays (UEAs, Blackrock Microsystems Inc., Salt Lake City, UT), and Floating Microelectrode arrays (FMA, Microprobes for Life Science, Gaithersburg, MD) into the brainstem of 11 monkeys.

Table **5-1** describes the type of array and design specifications for each implanted array. The FMAs, with electrodes of customized length, allowed us to access neurons with distal cutaneous RFs in the deeper aspects of the nucleus, while UEA electrodes with 1.5-mm long electrodes were well suited to the location of proprioceptive neurons with RFs on the proximal limb (see below).

The insertion technique varied depending on the array: UEAs were implanted with the standard Blackrock pneumatic inserter and FMAs were inserted slowly with a stereotaxic instrument while being held by a vacuum wand (Rousche and Normann 1998; Musallam et al. 2007). Array insertion was often complicated by brain stem vascularization. Indeed, as a sizeable artery often courses along the dorsal brain stem across the desired location of the implant (Figure 5.1A), we were occasionally forced to implant the array on the contralateral side to avoid vascular injury.

After array insertion, a thin layer of Tisseel fibrin dural sealant (Baxter Healthcare, Deerfield, IL) or Vetbond n-butyl cyanoacrylate (3M, St. Paul, MN) was placed over the array to stabilize it. Indeed, early implants that were not fixed with an adhesive appeared to be expelled from the brainstem shortly after implantation (Table 1; KR and CH1). The dura was closed with interrupted 6-0 Prolene sutures, taking care to cinch it around the wire bundle as tightly as possible. Due to the high risk of CSF leakage with posterior fossa procedures, and the fragile nature of the animals' dura, a layer of Duragen Plus (Integra, Plainsboro, NJ) followed by a layer of Tisseel was placed over the closed dura to further reduce the chance of a CSF fistula. Finally, muscle and skin were closed. Figure 5.1A and 5.2B show the surgical exposure after insertion of each type of array.

5.4.3 Data acquisition

In the acute experiments, neural signals were recorded using resin-coated tungsten or glass-coated platinum-iridium electrodes (FHC, Bowdoin ME) with impedances varying from 0.5 to 4 MΩ. These signals were amplified by a DAM50 amplifier (World Precision Instruments, Sarasota FL) and simultaneously played through audio speakers and displayed on an oscilloscope. Single unit and multi-unit activity from chronically implanted electrode arrays were recorded using a Cerebus system (Blackrock Microsystems, Inc., Salt Lake City, Utah). Spikes were sorted offline using standard software (Plexon Inc., Dallas, Texas).

5.4.4 Receptive field mapping

While listening to the neural activity, we manipulated the animals' joints, squeezed muscles, and gently brushed the surface of the skin to determine whether the neuronal

activity was driven by proprioceptive or tactile stimulation. The RFs of cutaneous units were drawn on a body diagram for later analysis. To characterize RF position of both cutaneous and proprioceptive units along the proximal-distal axis of the upper limb, we used a numeric system that defines RF location along this axis: 1- distal digits; 2- proximal digits; 3- wrist; 4-forearm; 5-elbow; 6-upper arm; 7-shoulder.

5.4.5 Vibrotactile stimulation

We delivered tactile stimuli to the distal pads of the digits using a stainless steel probe with a 1 mm tip diameter, driven by a custom shaker motor (Westling et al. 1976). We delivered sinusoidal stimuli – each 1 second long and separated by a 1-second inter-stimulus interval – at 5, 10, 20, 30, 40, 50, 100, 200, 250, and 300 Hz. Amplitudes were spaced in 10 equal logarithmic steps spanning the following ranges at each frequency: 13-250 μm for 5-50 Hz, 4–200 μm at 100 Hz, 1-100 μm at 200 Hz, 1.3 - 75 μm at 250 Hz, and 0.7-50 μm at 300 Hz. The shaker motor was calibrated before each experimental run and stimuli were presented in pseudorandom order.

5.4.6 Anatomical Imaging

To confirm the position of arrays and leads after weeks of recovery, we performed x-ray on 3 animals and 3D magnetic resonance imaging on 1 animal 5-8 weeks post-implantation (Figure 5.4D and Figure 5.4E). X-ray images in the sagittal plane offer the clearest view of the full implant, including the pedestal, leads and array.

Andersen P, Eccles JC, Oshima T, Schmidt RF. Mechanisms of synaptic transmission in the cuneate nucleus [Online]. *J Neurophysiol* 27: 1096–1116, 1964a. http://jn.physiology.org/content/27/6/1096.2.abstract [14 Feb. 2015].

ANDERSEN P, ECCLES JC, SCHMIDT RF, YOKOTA T. IDENTIFICATION OF RELAY CELLS AND INTERNEURONS IN THE CUNEATE NUCLEUS. [Online]. *J Neurophysiol* 27: 1080–95, 1964. http://www.ncbi.nlm.nih.gov/pubmed/14223971 [29 Jul. 2016].

Andersen P, Eccles JC, Schmidt RF, Yokota T. Identification of relay cells and interneurons in the cuneate nucleus [Online]. *J Neurophysiol* 27: 1080–1095, 1964b. http://jn.physiology.org/content/27/6/1080.2.abstract [14 Feb. 2015].

Andersen P, Eccles JC, Schmidt RF. Presynaptic Inhibitory Actions: Presynaptic Inhibition in the Cuneate Nucleus. *Nature* 194: 741–743, 1962.

Bensmaia SJ, Denchev P V., Dammann JF, Craig JC, Hsiao SS. The representation of stimulus orientation in the early stages of somatosensory processing. *J Neurosci* 28: 776–786, 2008.

Biedenbach MA, Jabbur SJ, Towe AL. Afferent inhibition in the cuneate nucleus of the rhesus monkey. 1971.

Boivie J, Boman K. Termination of a separate (proprioceptive?) cuneothalamic tract from external cuneate nucleus in monkey. *Brain Res* 224: 235–246, 1981.

Buford J, Davidson A. Movement-related and preparatory activity in the reticulospinal system of the monkey [Online]. *Exp. brain Res.* http://link.springer.com/article/10.1007/s00221-004-1956-4 [24 May 2017].

Canedo A, Mariño J, Aguilar J. Lemniscal recurrent and transcortical influences on cuneate neurons. *Neuroscience* 97: 317–334, 2000.

Costanzo RM, Gardner EP. Multiple-joint neurons in somatosensory cortex of awake monkeys. *Brain Res* 214: 321–333, 1981.

Florence SL, Wall JT, Kaas JH. The somatotopic pattern of afferent projections from the digits to the spinal cord and cuneate nucleus in macaque monkeys [Online]. *Brain Res* 452: 388–392, 1988. http://www.sciencedirect.com/science/article/pii/0006899388900455 [20 Aug. 2014].

Florence SL, Wall JT, Kaas JH. Somatotopic organization of inputs from the hand to the spinal gray and cuneate nucleus of monkeys with observations on the cuneate nucleus of humans. *J Comp Neurol* 286: 48–70, 1989.

Fuchs A, Luschei E. Firing patterns of abducens neurons of alert monkeys in relationship to horizontal eye movement. [Online]. *J. Neurophysiol.* http://psycnet.apa.org/psycinfo/1970-18062-001 [24 May 2017].

Gardner EP, Costanzo RM. Properties of kinesthetic neurons in somatosensory cortex of

awake monkeys. *Brain Res* 214: 301–319, 1981.

HARRIS F, JABBUR SJ, MORSE RW, TOWE AL. Influence of the Cerebral Cortex on the Cuneate Nucleus of the Monkey. *Nature* 208: 1215–1216, 1965.

Harvey MA, Saal HP, Dammann 3rd JF, Bensmaia SJ. Multiplexing stimulus information through rate and temporal codes in primate somatosensory cortex. *PLoS Biol* 11: e1001558, 2013a.

Harvey MA, Saal HP, Dammann III JF, Bensmaia SJ, Iii JFD, Bensmaia SJ. Multiplexing Stimulus Information through Rate and Temporal Codes in Primate Somatosensory Cortex. *PLoS Biol* 11: e1001558, 2013b.

Hayward V, Terekhov A V., Wong S-C, Geborek P, Bengtsson F, Jörntell H. Spatio-temporal skin strain distributions evoke low variability spike responses in cuneate neurons. *J R Soc Interface* 11: 20131015, 2014.

Hoffman D, Dubner R, Hayes R. Neuronal activity in medullary dorsal horn of awake monkeys trained in a thermal discrimination task. I. Responses to innocuous and noxious thermal [Online]. *J.* http://jn.physiology.org/content/46/3/409.short [24 May 2017].

Hummelsheim H, Wiesendanger M. Neuronal responses of medullary relay cells to controlled stretches of forearm muscles in the monkey [Online]. *Neuroscience*. http://www.sciencedirect.com/science/article/pii/0306452285901113 [27 Jul. 2017].

Hummelsheim H, Wiesendanger R, Wiesendanger M. The projection of low-threshold muscle afferents of the forelimb to the main and external cuneate nuclei of the monkey [Online]. *Neuroscience*. http://www.sciencedirect.com/science/article/pii/0306452285901101 [27 Jul. 2017].

Jabbur SJ, Banna NR. Presynaptic inhibition of cuneate transmission by widespread cutaneous inputs. *Brain Res* 10: 273–276, 1968.

Johnson KO, Lamb GD. Neural mechanisms of spatial tactile discrimination: neural patterns evoked by braille-like dot patterns in the monkey. [Online]. *J Physiol* 310: 117–144, 1981. http://www.ncbi.nlm.nih.gov/pmc/articles/PMC1274731/ [17 Jun. 2016].

Jörntell H, Bengtsson F, Geborek P, Spanne A, Terekhov AV, Hayward V. Segregation of Tactile Input Features in Neurons of the Cuneate Nucleus. *Neuron* 83: 1444–1452, 2014.

London BM, Miller LE. Responses of somatosensory area 2 neurons to actively and passively generated limb movements. *J Neurophysiol* 109: 1505–1513, 2013.

London BM, Torres RR, Slutzky MW, Miller LE. Designing stimulation patterns for an afferent BMI: representation of kinetics in somatosensory cortex. *Conf Proc . Annu Int Conf IEEE Eng Med Biol Soc IEEE Eng Med Biol Soc Annu Conf* 2011: 7521–4, 2011.

Mai J, Paxinos G. Somatosensory System: The human nervous system.

Molinari HH, Schultze KE, Strominger NL. Gracile, cuneate, and spinal trigeminal

projections to inferior olive in rat and monkey. *J Comp Neurol* 375: 467–480, 1996.

Mountcastle VB, Talbot WH, Darian-Smith I, Kornhuber HH. Neural basis of the sense of flutter-vibration. *Science (80-)* 155: 597–600, 1967.

Muniak MA, Ray S, Hsiao SS, Dammann JF, Bensmaia SJ. The neural coding of stimulus of mechanoreceptive afferents with psychophysical behavior (vol 27, pg 11687, 2007). *J Neurosci* 28, 2008.

Musallam S, Bak MJ, Troyk PR, Andersen RA. A floating metal microelectrode array for chronic implantation. *J Neurosci Methods* 160: 122–127, 2007.

Niu J, Ding L, Li J, Kim H, Liu J, Li H. Modality-based organization of ascending somatosensory axons in the direct dorsal column pathway [Online]. *J.* http://www.jneurosci.org/content/33/45/17691.short [5 Jan. 2017].

O'Neal JT, Westrum LE. The fine structural synaptic organization of the cat lateral cuneate nucleus. A study of sequential alterations in degeneration. *Brain Res* 51: 97–124, 1973.

Prud'homme MJ, Kalaska JF. Proprioceptive activity in primate primary somatosensory cortex during active arm reaching movements. *J Neurophysiol* 72, 1994.

Qi H-X, Kaas JH. Organization of primary afferent projections to the gracile nucleus of the dorsal column system of primates. *J Comp Neurol* 499: 183–217, 2006.

Richardson AG, Weigand PK, Sritharan SY, Lucas TH. Somatosensory encoding with cuneate nucleus microstimulation: Effects on downstream cortical activity. , p. 695–698.

Richardson AG, Weigand PK, Sritharan SY, Lucas TH. A chronic neural interface to the macaque dorsal column nuclei [Online]. *J Neurophysiol* 115, 2016. http://jn.physiology.org/content/115/5/2255 [12 Jun. 2017].

Rousche PJ, Normann RA. Chronic recording capability of the Utah Intracortical Electrode Array in cat sensory cortex. *J Neurosci Methods* 82: 1–15, 1998.

Saal HP, Bensmaia SJ. Touch is a team effort: interplay of submodalities in cutaneous sensibility. *Trends Neurosci* 37: 689–697, 2014a.

Saal HP, Bensmaia SJ. Touch is a team effort: interplay of submodalities in cutaneous sensibility. *Trends Neurosci* 37: 689–697, 2014b.

Talbot WH, Darian-Smith I, Kornhuber HH, Mountcastle VB. The sense of flutter-vibration: comparison of the human capacity with response patterns of mechanoreceptive afferents from the monkey hand. *J Neurophysiol* 31: 301–34, 1968.

Vaidya M, Dickey A, Best MD, Coles J, Balasubramanian K, Suminski AJ, Hatsopoulos NG. Ultra-long term stability of single units using chronically implanted multielectrode arrays. In: *2014 36th Annual International Conference of the IEEE Engineering in Medicine and Biology Society*. IEEE, 2014, p. 4872–4875.

Westling G, Johansson RS, Vallbo O. Method for mechanical stimulation of skin receptors.

In: *Functions of the Skin in Primates*, edited by Zotterman Y. Oxford: Pergamon Press, 1976, p. 151–158.

Witham CL, Baker SN. Modulation and transmission of peripheral inputs in monkey cuneate and external cuneate nuclei. *J Neurophysiol* 106: 2764–75, 2011.

Chapter 6 | Tactile Coding in the Cuneate Nucleus

6.1 Introduction

The coding of tactile information has been extensively studied in the nerves and in the primary somatosensory cortex (S1) – area 3b – of non-human primates. One of the themes to emerge from this work is that sensory representations in S1 differ from those at the periphery in two important ways. First, while cutaneous nerve fibers can be classified into a small number of submodalities, each responding to a different aspect of skin stimulation, individual S1 neurons integrate sensory signals from multiple submodalities and exhibit a wide range of response properties (Prud'homme and Kalaska 1994; Pei et al. 2009; Saal and Bensmaia 2014a; Lieber and Bensmaia 2019a). Second, the responses of cortical neurons reflect computations on their inputs – temporal and spatial differentiation – which lead to give rise to explicit representations of behaviorally relevant stimulus features, such as edge orientation or motion direction (Bensmaia et al. 2008; Pei et al. 2010; Harvey et al. 2013a). The degree to which these properties of S1 responses begin to emerge in the two intervening structures along the medial lemniscal pathway, namely the cuneate nucleus (CN) and the ventroposterior nucleus of the thalamus, is unknown.

The objective of the present study was to begin to fill this gap by first assessing the degree to which individual CN neurons receive convergent input from multiple afferent classes. To this end, we measured the responses of CN neurons in anesthetized macaques to step indentations and vibrotactile stimuli, two classes of stimuli that have been used extensively to probe the response properties in the nerve and in cortex. We then compare CN responses to their counterparts in the nerve and in S1. Next, we assess whether CN neurons exhibit

response properties that imply some computation beyond submodality convergence. For example, one of the canonical response properties of neurons in S1 is of spatial and temporal differentiation. We also examine differences in the population level representations of stimulus features, in this case the frequency and amplitude of skin vibrations.

Convergence of Afferent Modalities

Three types of cutaneous afferents innervate the glabrous skin of the hand, and play complementary but overlapping roles in tactile perception (Saal and Bensmaia 2014a). One of the canonical differences between afferent classes is in their responses to step indentations: SA1 afferents produce sustained responses throughout the stimulus whereas RA and PC afferents respond only at its onset and offset (top two rasters in Figure 6.1). Another key property of afferents is that, while all nerve fibers produce highly patterned responses to skin vibrations, the different afferent classes exhibit different frequency sensitivity profiles (Talbot et al. 1968; Muniak et al. 2008). SA1 fibers are most sensitive at the low frequencies (< 10 Hz), PC fibers are most sensitive at the high frequencies (> 200 Hz), and RA fibers exhibit intermediate frequency preference.

Traditionally, tactile submodalities were thought to play specific and non-overlapping functional roles in touch (Johnson 2001; Saal and Bensmaia 2014a). For example, PC fibers were thought to solely mediate vibration perception, while SA1s were thought to mediate shape and texture perception. Accordingly, signals from the different submodalities were thought to remain largely segregated as they ascend the neuraxis. Cortical neurons were thus classified as being SA1-like, RA-like, or PC-like. Re-examination of this phenomenon, however, has yielded a fundamentally different perspective (Saal and Bensmaia 2014b). Indeed, while some cortical neurons exhibit responses to responses to step indentations that are SA1-like or RA-1-like (third and fourth raster plots of Figure 6.1), most exhibit both

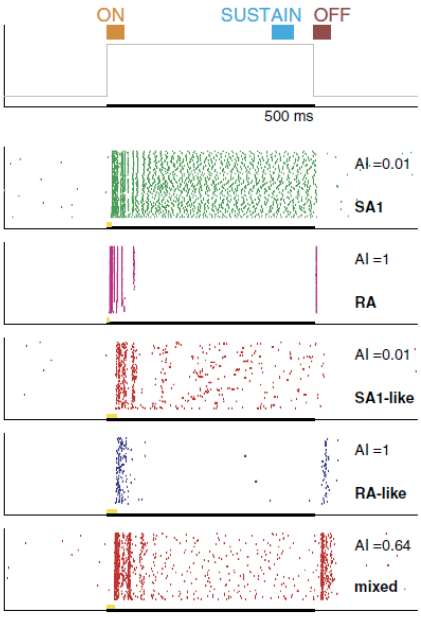

Figure 6.1.Responses of one SA1 afferent, one RA afferent, and three S1 neurons to sixty repeated presentations of a step indentation (along with the corresponding adaptation index, or AI; see text for explanation). SA1 afferents respond throughout the indentation, RA (as well as PC) afferents respond only at its onset and offset. In contrast, the majority of S1 n eurons exhibit responses that reflect convergent input from both afferent types (bottom raster). Reproduced from Pei et al. 2009

a sustained, emblematic of SA1 input, and an off response, symptomatic of RA or PC input (see bottom raster of Figure 6.1)(Pei et al. 2009). Furthermore, S1 neurons tend to respond to a broader range of vibratory frequencies than do individual afferents (Harvey et al. 2013). These results and others suggest that individual S1 neurons receive convergent input from multiple tactile submodalities. The textbook understanding of CN is that no convergence takes place there: the responses of individual CN neurons have been reported to be very similar to those of individual tactile afferents, and CN functions as a relay of sensory signals (Kandel 2012).

6.2 | Results

To investigate tactile representations in CN, we measured the responses of individual CN neurons to step indentations (n=47) and to skin vibrations (n=59) at various frequencies and amplitudes. First, we sought to determine whether individual CN neurons receive convergent input from more than one type of tactile nerve fiber. The presence of afferent convergence onto single CN cells would challenge the textbook notion that CN is a simple relay of afferent information (Dykes et al. 1982) and would rather suggest that this structure plays an active role in tactile processing.

To compare CN responses to their peripheral counterparts, we simulated the responses of 210 afferents with TouchSim (Saal et al. 2017b) using the same amplitude-frequency conditions that were used in the CN recordings. To compare CN responses to their cortical counterparts, we analyzed previously collected cortical (S1) data (Harvey et al. 2013a),

focusing on the responses obtained under similar stimulus conditions (a total of 20 amplitude-frequency pairs ranging from 50Hz to 300Hz).

6.2.1 Adaptation properties in individual CN neurons reveal afferent submodality convergence

First, we investigated CN responses to step indentations, which provided a first test of whether individual neurons exhibit distinct SA-1-like or RA/PC-like responses, or whether they reflect a mixture of these response classes. Specifically, responses during the sustained

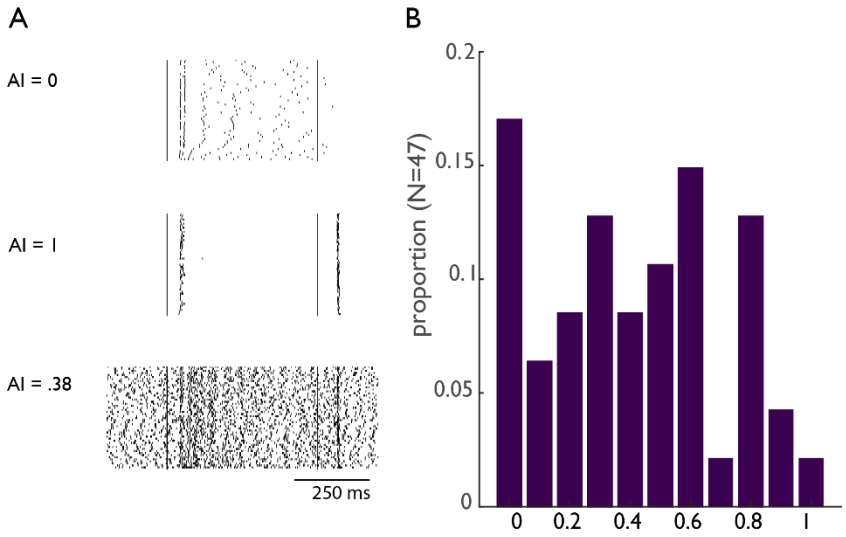

Figure 6.2. Adaptation Index of CN neurons.

A| Example rasters from individual CN neurons illustrate the range of response properties observed. Top, AI=0; Middle, AI=1; Bottom, AI=0.38 B| AI index population results for cuneate neurons reveal submodality convergence in individual CN neurons.

component of the stimulus reflect SA1 input, as only this class is active during this stimulus epoch; a strong phasic response during the offset of the indentation is indicative of RA or PC input as only these two classes of nerve fibers exhibit on OFF-response. Co-occurrence of these two response properties is thus indicative of convergent input.

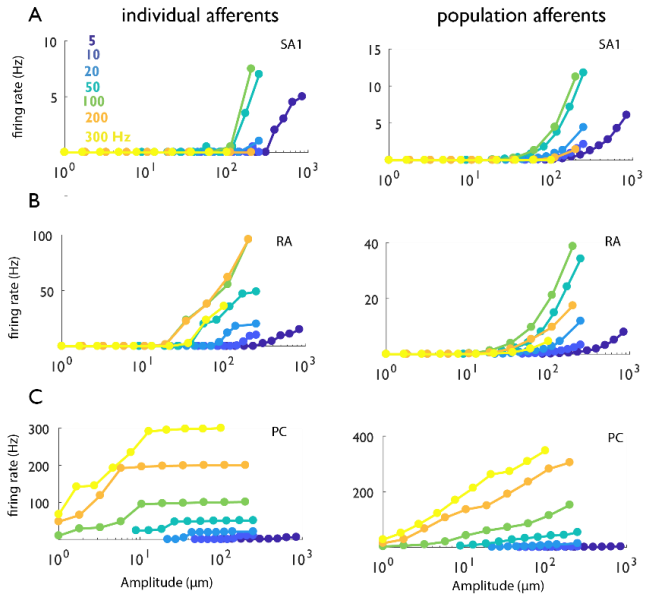

Figure 6.3. Peripheral Rate-Intensity Functions.

A| Example SA1 afferent responses to vibrotactile stimuli. Left shows individual afferent responses, right shows population averaged responses. B| Example RA afferent response to vibrotactile stimuli. Left shows individual afferent responses, right shows population averaged responses. C| Example PC response to vibrotactile stimuli. Left shows individual afferent responses, right shows population averaged responses.

A previously developed 'adaptation index' (Pei et al. 2009) gauges the degree to which individual neurons receive convergent input from multiple cutaneous submodalities. This index takes on a value of 1 when responses are RA-like (only an off-response, no sustained response), 0 when responses are SA-like (only a sustained response, no off response), and an intermediate value when responses reflect convergent input (mixture of sustained and off response). We found that individual cuneate neurons exhibit response properties indicative of convergent input from multiple submodalities (Figure 6.2). The relatively uniform distribution of the adaptation index between 0 and 1 suggests that convergence is the rule rather than the exception and that the strength of the SA and RA input varies widely across CN neurons.

6.2.2 Vibrotactile Responses in CN exhibit submodality convergence

Next, we examined the responses of CN neurons to skin vibrations varying in amplitude and frequency. Indeed, as discussed above, different afferent classes exhibit different frequency sensitivity profiles. By examining the frequency response characteristic of individual CN neurons, we can assess whether it resembles that of any one class of tactile nerve fiber, or rather reflects convergent input from multiple fiber types.

Figure 6.3 shows the simulated responses to skin vibrations of individual nerve fibers of each type: As has been previously shown (Muniak et al. 2008), SA1 afferents respond

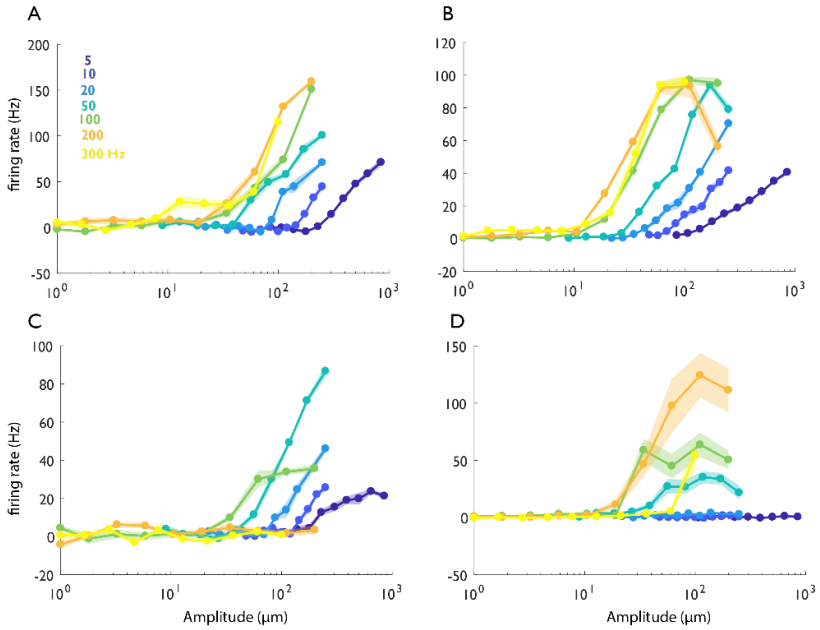

Figure 6.4 CN Rate-Intensity Functions.

A| Example CN response to vibrotactile stimuli. This unit robustly responds to frequencies across the whole range (5-300Hz), which suggests that it may receive input from all afferent classes B| Example CN response to vibrotactile stimuli. This unit also robustly responds to a broad range of frequencies, but exhibits a plateau at higher frequencies (200-300Hz), suggesting there may be a mixing of several SA1 and RA afferents with a single PC afferent. C| Example CN response to vibrotactile stimuli. This unit responds exclusively to frequencies below 50Hz, which suggests that it may receive input from primarily SA1 afferents. D| Example CN response to vibrotactile stimuli. This unit responds exclusively to higher frequencies (50 and above), which suggests it may have primarily PC input. Shaded area represents standard deviation of firing rates (over 5 trials)

exclusively to low frequencies (5-50Hz), RA afferents respond over a broad bandwidth (5 - 300 Hz), and PC afferents are very sensitive to high frequencies (>200 Hz). The responses of individual nerve fibers often exhibit plateaus in their rate-intensity functions (Figure 6.3C, left). That is, the firing rate remains constant as amplitude increases. These plateaus are not observed in the responses of afferent populations, however, because they occur at different amplitude levels for different nerve fibers and average out in the aggregate response. Individual CN neurons often respond to a range of frequencies, the width of which is uncharacteristic of any single afferent population (Figure 6.4). For example, some CN neurons respond robustly to the entire range of frequencies stimulated (see Figure 6.4A), indicative of input from multiple afferent classes. Other units respond primarily or exclusively to frequencies above 50Hz, which suggests that they receive little SA1 input. Notably, some CN neurons exhibit plateaus, while others do not, suggesting that some CN neurons receive input from relatively few afferents whereas others receive input from a sufficient number to obscure the plateaus. In summary, then, CN responses to vibrations are qualitatively consistent with the hypothesis that most receive convergent input from multiple tactile submodalities.

Notably, a few of the CN neurons exhibited inhibitory responses under some stimulation conditions, a phenomenon that is never observed at the periphery. Some CN neurons were always inhibited by vibrations (Figure 6.5, panel A,B) whereas others were excited by some vibrations and inhibited by others. Inhibitory responses in CN constitute a step towards the differentiation (in time and space) that is observed in S1. Indeed, S1 neurons can be described as spatial filters – comprising excitatory and inhibitory lobes – or temporal filters,

differentiating their inputs in time (DiCarlo et al. 1998)(Saal et al. 2015). These differentiation computations play an important role in giving rise to neuronal representations in which sensory information is multiplexed such that different stimulus features can be read out linearly (Lieber and Bensmaia 2019b). The presence of inhibitory and responses is consistent with the hypothesis that CN plays an active role in these computations.

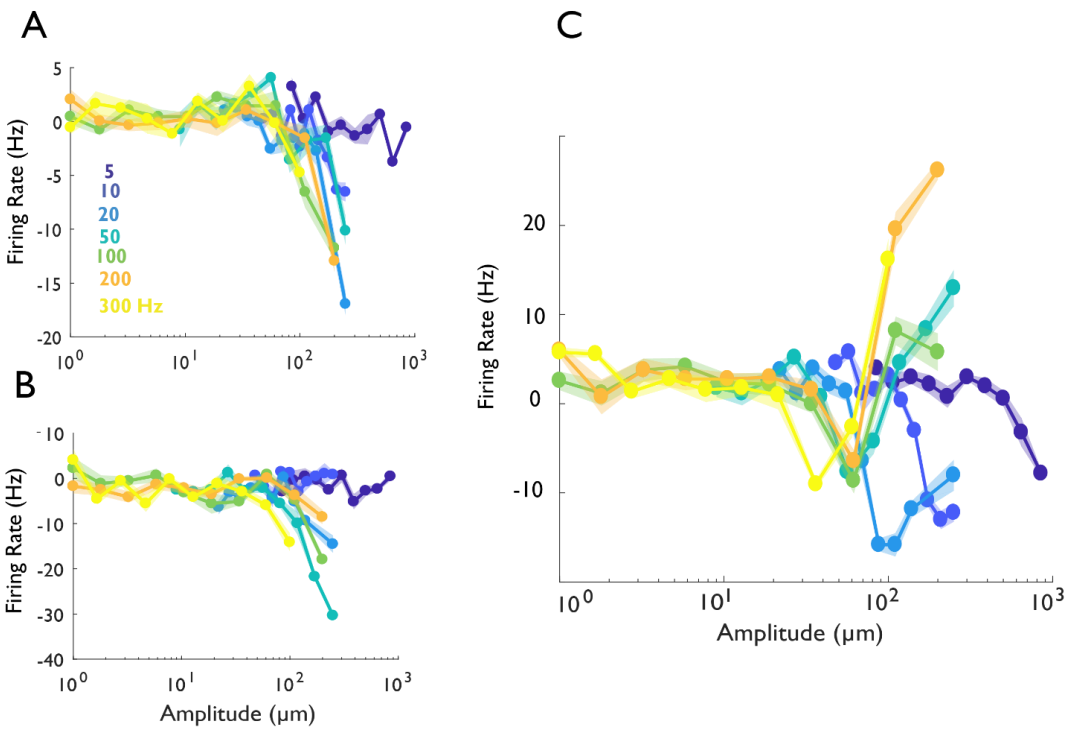

Figure 6.5. CN Rate Intensity Functions exhibiting Inhibitory Behavior.

A| Example CN response to vibrotactile stimuli, exhibiting an inhibitory (or suppressed) response to frequencies > 5 Hz. B| Example CN response to vibrotactile stimuli. Here, inhibitory responses begin after 10 Hz. C| Example CN response to vibrotactile stimuli. Responses demonstrate excitatory behavior for higher frequencies (>50Hz), and inhibitory behavior for lower frequencies (5-20Hz). To understand how inhibitory behavior contributes towards tactile processing in CN, we will collect more data.

6.2.3 Comparing Vibrotactile responses in CN to afferents and S1 neurons

To quantitatively assess the contributions of different afferent classes to the responses of individual CN neurons, we regressed the trial-averaged firing rates of individual CN neurons evoked by 70 vibratory stimuli varied in frequency and amplitude onto the (simulated) responses of afferents from all three classes to the same stimuli (Figure 6.6A). For comparison, we regressed the responses of individual afferents onto the responses of all three classes to verify that this analysis would correctly identify a lack of convergence in this case. We found that the responses of most CN neurons could be well accounted for

with a linear combination of SA1, RA, and PC responses (mean R^2=0.67), though not as well as could the responses of individual afferents, as expected (R^2=0.81). Next, we assessed whether CN responses were better accounted for by multiple inputs than by one. To this

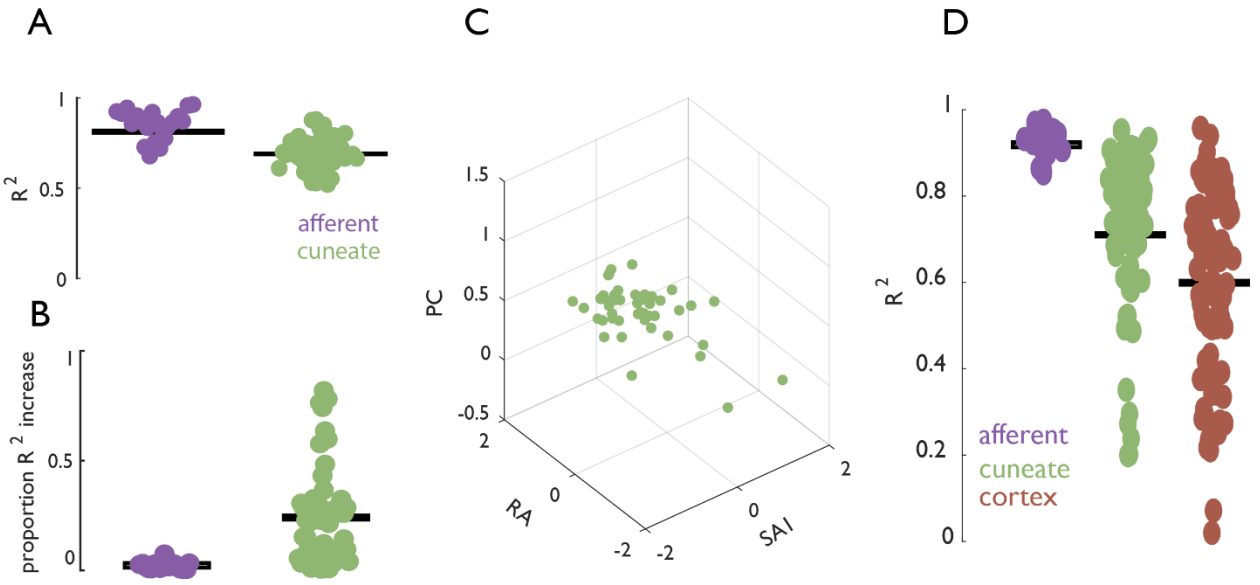

Figure 6.6 Quantitatively assessing submodality convergence using regression models.

A| Firing rates of individual neurons regressed against the population rates computed for SA1, RA, and PC afferents. Each point denotes an individual afferent (purple) or individual CN neuron (green). B| Proportion R^2 increase for the full model compared to the best single-predictor model. The model fit does not improve for afferents (as expected) but does for CN neurons. C| Regression weights for individual CN cells. Weights do not cluster and exhibit mixing of afferent channels. D| Firing rates of individual neurons regressed against population rates computed for SA1, RA, and PC afferents for a set of conditions that is common across the three experiments. Each point denotes an individual afferent (purple), individual CN neuron (green), or individual SCx (area 3b,red).

end, we compared the linear fits (R^2) obtained with the best single afferent population as a regressor to those obtained with all three populations. As expected, the fit did not improve when predicting afferent responses from multiple afferent populations. However, the fit increased substantially for most CN neurons with the inclusion of all inputs (Figure 6.6).

In conclusion, then, the responses of individual CN neurons to vibrations reflect input from multiple classes of nerve fibers.

Next, we wished to examine whether CN neurons cluster into categories depending on their afferent input. To this end, we examined the regression weights obtained for CN units that yielded satisfactory fits (R^2>0.5, and a p-value of <.05). Having verified that the regression weights obtained for afferents clustered, we found that single CN units yielded regression weights that varied smoothly over the range (Figure 6.5C). Thus, CN neurons receive input from the different modalities in a highly idiosyncratic way with no discernible structure or clusters.

We then compared submodality convergence in CN and S1 by repeating the regression analysis on (nearly) matched amplitude-frequency conditions. We found that, as expected, R^2 values for CN neurons were on average higher (R^2 = 0.72) than cortical neurons (R^2 = 0.61), reflecting a greater degree of non-linearity in the responses as one ascends the neuraxis (see Saal et al. 2015). Furthermore, cortical responses were better accounted for with multiple afferent inputs, as was found in CN. Finally, cortical neurons did not exhibit any clustering, as was found in CN. We conclude that much of the convergence that is observed in cortex is already present in CN.

Finally, for the four neurons that exhibited inhibitory responses to vibrotactile stimulation (Figure 6.5), we found that model fit was significantly reduced when regression weights were constrained to be positive (mean 22% decrease), consistent with the qualitative observation that they have an inhibitory component in their response. These CN neurons

do seem to reflect a computation, though they are far rarer than their purely excitatory counterparts.

6.2.4 Population Level Representation of Vibrotactile Stimulus Features

Having shown that CN neurons receive convergent input from multiple submodalities and can exhibit hallmarks of neuronal computations beyond simply integrating different types of input signals, we wished to examine population-level sensory representations in CN and contrast them to their peripheral and cortical counterparts.

To this end, we first examined the structure of the response of populations of afferents, CN neurons, and S1 neurons. First, we performed a principal components analysis (PCA) on the trial-averaged spike counts (0-100ms post stimulus presentation) for all units in each area (periphery N=200, cuneate N=59, cortex N=33) to matched vibratory stimuli. As has been previously shown, the firing rates of afferent populations occupied a lower dimensional space than did their cortical counterparts (Lieber and Bensmaia 2019a), as reflected by a much steeper relationship between cumulative variance explained and number of principal components (PCs) for afferents than for cortical neurons (Figure 6.7A). We found that the structure of the response space of CN was more similar to that of S1 than that of the nerve, consistent with the hypothesis that CN neurons reflect a computation and are not just relays for sensory signals.

Next, we investigated how stimulus features were encoded in neural subspaces by examining how the two stimulus parameters – amplitude and frequency – mapped onto the first two principal components of the population responses. For all areas, the first

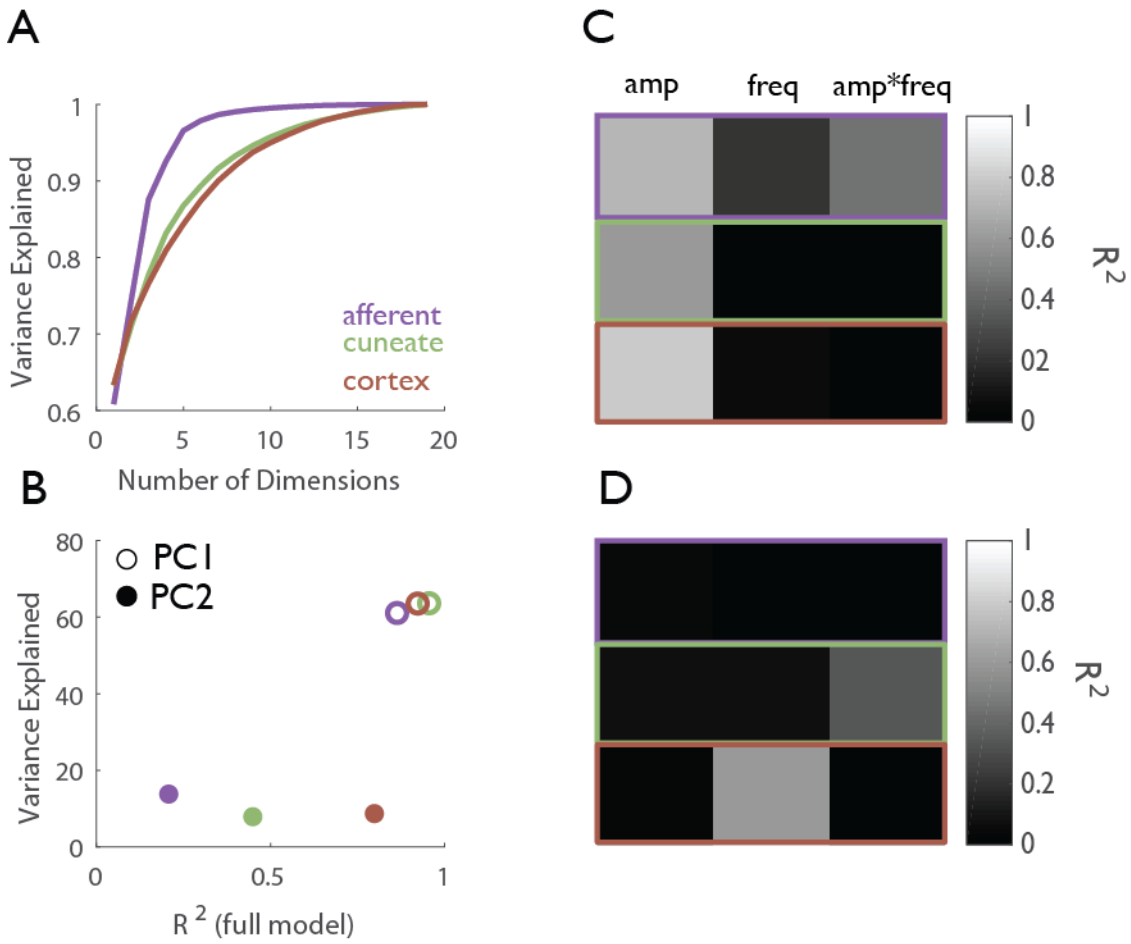

Figure 6.7 Population coding of stimulus features.

A| Cumulative variance explained as a function of the number of principal components for the afferent, cuneate, and cortical populations. B| Fraction of variance explained as a function of R^2 (full model: amplitude, frequency, and amplitude*frequency) for the first and second principal component. C| R^2 values for PC1 regressed against individual features: amplitude, frequency, and amplitude*frequency. D| R^2 values for PC2 regressed against individual features: amplitude, frequency, and amplitude*frequency

principal component – the mean population firing rate – accounted for ~60% variance. Regression analysis revealed a strong linear association between this parameter and the stimulus features for all three populations S1 (R^2 ~ 0.95). However, examination individual

models revealed that, in the nerve, PC1 reflected a mixed selectivity for amplitude, frequency, and their interaction whereas PC1 was only associated with amplitude in CN and S1 (Figure 6.7C). The association between PC1 and amplitude was strongest in cortex. These results suggest that the population firing rate conveys information about amplitude in an increasingly unambiguous way as one ascends the somatosensory neuraxis, consistent with previous findings (Harvey et al. 2013b), and that CN constitutes an intermediate step in this computation (Figure 6.7C).

The association between the second axis of neuronal variance, PC2, and stimulus parameters is much weaker for the nerve than it is for S1 (R^2 = 0.23 and 0.81, respectively). In the latter, PC2 is strongly related to stimulus frequency at the expense of amplitude. In CN, this axis of neuronal variance encodes an interaction between amplitude and frequency and may thus constitute a step towards the frequency specificity of this axis in cortex (Figure 6.7D).

We conclude that, at the population level, representations are intermediate between those observed in the nerve, and those observed in S1.

6.3 Discussion

This study constitutes the first characterization of the tactile response properties in the CN of primates. First, we found that individual CN neurons receive convergent input from multiple afferent classes. Second, we observed that CN responses exhibit inhibitory responses, which is not observed at the periphery. Third, we found that the population-level sensory representations in CN constitute an intermediary between their peripheral

and cortical counterparts. Together, these findings suggest that the CN is not a simple relay station for tactile signals but rather plays an active role in processing.

Next, we will carry out an additional series of experiments designed to characterize receptive field structure and to explore how behaviorally relevant stimulus features – edges and texture, e.g. – are encoded in the responses of individual CN neurons and of neuronal populations, as briefly summarized below.

RF Structure

While SA1 and RA afferents tend to have small, well-defined excitatory RFs and PCs have large diffuse ones, S1 neurons have complex RFs often encompassing multiple digits. S1 RFs also typically comprise an excitatory region flanked by one or more inhibitory regions. The RF structure of S1 neurons accounts in part for some of their response properties, for example edge orientation, which exhibits much more robust tuning than its counterpart at the periphery. In brief, the structure of RFs changes systematically as one ascends the somatosensory neuraxis, and differences in RF structure account in part for differences in neuronal response properties. We plan to apply random dot stimuli to characterize the fine RF structure of CN neurons. Applying random dot stimuli will allow us to determine RF size, and also whether inhibitory subfields emerge in the brainstem. We expect to find an RF structure that is intermediate between that of afferents and that of cortical neurons.

Feature Coding in the CN

As detailed above, the response properties of mechanoreceptive afferents and S1 neurons have been probed using a wide variety of complex stimuli, such as scanned textures, and

oriented lines. These stimuli are more ecologically significant than are punctate indentations or sinusoidal vibrations, and probe neuronal selectivity for behaviorally relevant stimulus features. The responses of individual S1 neurons to such complex stimuli have been shown to convey more explicit information about stimulus features than do their peripheral counterparts. We intend to record activity of single CN neurons and determine the extent to which CN neurons are tuned to behaviorally relevant features, as are cortical neurons.

Sensory representations in other sub-cortical structures

After characterizing how behaviorally relevant features are encoded in CN, we can compare these findings with response properties of sub-cortical structures in visual and auditory systems. All sensory signals converge onto the thalamus prior to diverging towards dedicated cortical areas, so we aim to understand the extent to which subcortical sensory modality representations are similar between auditory, visual, and somatosensory systems. We hypothesize that similar computations, and analogous elementary feature representations will be found in the brainstem component of tactile processing ganglion cells in the visual system, and in the cochlea nucleus of the auditory system.

6.4 Methods

Cuneate Nucleus Neurophysiology

Surgical Approach:

The monkey was positioned in the stereotaxic frame with the neck flexed 60-70 degrees to provide access to the dorsal brainstem. We exposed and enlarged the foramen magnum. The caudal edge of the cerebellar tonsils were retracted as necessary to expose the implant

site, including both the main and external CN, extending about 2 mm rostral and caudal to the obex. All surgical and behavioral procedures will be approved and monitored by the Institutional Animal Care and Use Committee at the University of Chicago, and are consistent with federal guidelines. A total of 3 monkeys were used towards this experiment, and 106 units were recorded.

Neurophysiological Recordings

Recordings were performed using a 16-channel linear probe (Plexon Inc., Dallas TX). The electrode was positioned above the brainstem using a stereotaxic manipulator. Neural data was acquired using a Cerebus system (Blackrock Microsystems, Inc., Salt Late City, Utah). We identified threshold crossings (six times the root-mean square noise) on each of the recording channels and record the time of each threshold crossing along with a waveform snippet surrounding it. We then sorted the resulting waveforms using Offline Sorter (Plexon, Inc, Dallas, TX) to isolate the responses of single neurons. Neurons were included only if they have an SNR of greater than 3, and a negligible number of short ISIs (fewer than 0.19% of spikes with an ISI of less than 1.7 msec) to enforce a refractory period. All other responses will be considered stemming from multiple neurons (i.e., multi-unit activity).

Stimuli

We delivered tactile stimuli to the distal pads of the digits using a stainless steel probe with a 1mm tip diameter, driven by a custom shaker motor ((Westling et al. 1976). We delivered sinusoidal stimuli – each 1 second long and separate by a 1 second inter-stimulus interval at 5, 10, 20, 30, 40, 50, 100, 200, 250, and 300 Hz. Amplitudes were spaced in 10 equal

logarithmic steps spanning the following ranges at each frequency: 13-250 μm for 5-50 Hz, 4–200 μm at 100 Hz, 1-100 μm at 200 Hz, 1.3 - 75 μm at 250 Hz, and 0.7-50 μm at 300 Hz. Stimuli were presented in pseudorandom order.

Step indent stimuli were delivered using the same probe, with a 1mm amplitude. For one monkey, the indentation profile involved a 25 ms ramp with a 500 ms hold period. For the other monkey, the indentation profile involved a 5ms ramp and a 75ms hold period.

Simulations of whole nerve responses

We wished to compare vibrotactile responses in CN to those observed at the periphery. To this end, we reconstructed the responses of 210 tactile nerve fibers – slowly adapting type 1 (SA1), rapidly adapting (RA), and Pacinian Corpuscle-associated (PC) – that innervate the palmar surface of the distal finger pad (second digit). Specifically, we used simulation of nerve responses that can accurately reproduce afferent responses with near millisecond accuracy (Saal et al. 2017a). In brief, the model first computes the skin's response to a time-varying stimulus impinging upon it, then generates the spiking response evoked in nerve fibers whose receptive fields tile the skin at measured innervation densities. This stimulation has been extensively validated using a variety of psychophysical and neurophysiological data sets (Goodman and Bensmaia 2017; Saal et al. 2017a). Using this model, we simulated the nerve responses to the vibrotactile simuli and compared these to their measured CN counterparts.

Cortical Data

Experimental procedures have been previously described and published (Harvey et al. 2013a). Briefly, individual extracellular recordings were made in the postcentral gyri in four hemispheres of two awake, behaving Rhesus macaques. In total, recordings were obtained from 33 area 3b neurons.

The vibrotactile stimuli have been previously described (Harvey et al. 2013a). Briefly, tactile stimuli were delivered to the distal pads of the digits using a stainless steel probe driven by a shaker motor. The shaker motor was calibrated before each experimental run such that stimuli were highly accurate and repeatable. For this study, only the sinuisoidal stimuli were used. Of the 70 sinusoidal amplitude-frequency conditions, 20 amplitude-frequency conditions ranging from 50-300Hz were used to match with those used for the CN experiments.

Data Analysis

Step Indent: Adaptation Index

The adaptation index was modified slightly from a previously published metric (Pei et al. 2009). RA afferents exclusively respond during the transient portions of a step indentation (onset and offset), whereas SA1 afferents respond during the sustained portion, and do not exhibit a distinct off response. We computed an adaptation index that gauges the degree of the "off" response relative to that of the "sustained" response. Due to the different step indentation stimulus paradigms for monkey 1 and monkey 2, different epochs were used. For monkey 1 (75ms hold period), the "off" response (R_{off}) was defined as 25 ms after

stimulus offset, and the sustained response ($R_{sustain}$) was defined as 25 ms beginning 50ms before the offset of the stimulus. For monkey 2 (500ms hold period), R_{off} was defined as 65ms after stimulus offset, and the sustained response was defined as 65 ms beginning 100 ms before the offset of the stimulus. These intervals were adjusted for response latency, and epochs were baseline firing corrected. The adaptation index was defined as:

$$AI = \frac{R_{Off}}{R_{off} + R_{sustained}}$$

If a CN neuron exhibited solely RA-like behavior, AI would be 1, since there would be an absence of a sustained response. If a CN exhibited solely SA1-like behavior, AI would be 0, since there would be an absence of an "off" response.

Vibrotactile: Afferent Contribution Regression Model

To investigate the relative contributions of the three defined population of tactile fibers towards individual afferents, individual CN neurons, and individual cortical neurons, we used a multiple regression model. Specifically, we standardized (z-scored) trial-averaged firing rates for each individual afferent, CN, or cortical neuron across each amplitude-frequency condition. We also standardized mean firing rates across simulated SA1, RA, and PC afferent populations to the same amplitude-frequency conditions. We used these normalized regression weights as measures of the relative strength of SA1, RA, and PC afferent input into each neuron.

Vibrotactile: Population Coding of Stimulus Features

To better understand how population feature coding evolves throughout the neuraxis, we used a subset of amplitude-frequency conditions matched amongst the CN and cortical

datasets. Neuronal responses were aligned to the onset of simulation, and the first 100ms of spiking activity were used. Firing rates for individual neurons were z-scored across condition. We then applied principal component analysis (PCA) to reduce the dimensionality of the population response.

To understand how neuronal subspaces relate to stimulus features, we regressed the first two principal components against their respective sinusoidal stimulation parameters: amplitude, frequency, and the interaction between amplitude and frequency (amplitude * frequency). Stimulus parameters were standardized by z-scores as well.

6.5 References

Bensmaia SJ, Denchev P V., Dammann JF, Craig JC, Hsiao SS. The representation of stimulus orientation in the early stages of somatosensory processing. *J Neurosci* 28: 776–786, 2008.

DiCarlo JJ, Johnson KO, Hsiao SS. Structure of receptive fields in area 3b of primary somatosensory cortex in the alert monkey. *J Neurosci* 18: 2626–45, 1998.

Dykes RW, Rasmusson DD, Sretavan D, Rehman NB. Submodality segregation and receptive-field sequences in cuneate, gracile, and external cuneate nuclei of the cat. [Online]. *J Neurophysiol* 47: 389–416, 1982. http://jn.physiology.org/content/jn/47/3/389.full.pdf [20 Aug. 2014].

Goodman JM, Bensmaia SJ. A Variation Code Accounts for the Perceived Roughness of Coarsely Textured Surfaces. *Sci Rep* 7: 46699, 2017.

Harvey MA, Saal HP, Dammann 3rd JF, Bensmaia SJ. Multiplexing stimulus information through rate and temporal codes in primate somatosensory cortex. *PLoS Biol* 11: e1001558, 2013a.

Harvey MA, Saal HP, Dammann III JF, Bensmaia SJ, Iii JFD, Bensmaia SJ. Multiplexing Stimulus Information through Rate and Temporal Codes in Primate Somatosensory Cortex. *PLoS Biol* 11: e1001558, 2013b.

Johnson KO. The roles and functions of cutaneous mechanoreceptors. *Curr Opin Neurobiol* 11: 455–461, 2001.

Kandel ER. *Principles of neural science*. 2012.

Lieber JD, Bensmaia SJ. High-dimensional representation of texture in somatosensory

cortex of primates. *Proc Natl Acad Sci U S A* 116: 3268–3277, 2019a.

Lieber JD, Bensmaia SJ. Emergence of an invariant representation of texture in primate somatosensory cortex. *bioRxiv* (May 24, 2019b). doi: 10.1101/646042.

Muniak MA, Ray S, Hsiao SS, Dammann JF, Bensmaia SJ. The neural coding of stimulus of mechanoreceptive afferents with psychophysical behavior (vol 27, pg 11687, 2007). *J Neurosci* 28, 2008.

Pei Y-C, Denchev P V., Hsiao SS, Craig JC, Bensmaia SJ. Convergence of submodality-specific input onto neurons in primary somatosensory cortex [Online]. *J Neurophysiol* 102: 1843–1853, 2009. http://jn.physiology.org/content/102/3/1843.short [21 Aug. 2014].

Pei Y-C, Hsiao SS, Craig JC, Bensmaia SJ. Shape invariant coding of motion direction in somatosensory cortex [Online]. *PLoS Biol* 8: e1000305, 2010. http://dx.plos.org/10.1371/journal.pbio.1000305 [21 Aug. 2014].

Prud'homme MJ, Kalaska JF. Proprioceptive activity in primate primary somatosensory cortex during active arm reaching movements. *J Neurophysiol* 72, 1994.

Saal H, Delhaye BR-P of the, 2017 U. Simulating tactile signals from the whole hand with millisecond precision [Online]. *Natl. Acad Sci.* http://www.pnas.org/content/114/28/E5693.short [6 Aug. 2018a].

Saal HP, Bensmaia SJ. Touch is a team effort: interplay of submodalities in cutaneous sensibility. *Trends Neurosci* 37: 689–697, 2014a.

Saal HP, Bensmaia SJ. Touch is a team effort: interplay of submodalities in cutaneous sensibility. *Trends Neurosci* 37: 689–697, 2014b.

Saal HP, Delhaye BP, Rayhaun BC, Bensmaia SJ. Simulating tactile signals from the whole hand with millisecond precision. *Proc Natl Acad Sci U S A* 114: E5693–E5702, 2017b.

Saal HP, Harvey MA, Bensmaia SJ. Rate and timing of cortical responses driven by separate sensory channels. *Elife* 4: e10450, 2015.

Talbot WH, Darian-Smith I, Kornhuber HH, Mountcastle VB. The sense of flutter-vibration: comparison of the human capacity with response patterns of mechanoreceptive afferents from the monkey hand. [Online]. *J Neurophysiol* 31: 301–34, 1968. http://www.ncbi.nlm.nih.gov/pubmed/4972033 [11 Oct. 2017].

Westling G, Johansson RS, Vallbo O. Method for mechanical stimulation of skin receptors. In: *Functions of the Skin in Primates*, edited by Zotterman Y. Oxford: Pergamon Press, 1976, p. 151–158.

Chapter 7 | Neural Population Dynamics in Motor Cortex are Different for Reach and Grasp[6]

Rotational dynamics are observed in neuronal population activity in primary motor cortex (M1) when monkeys make reaching movements. This population-level behavior is consistent with a role for M1 as an autonomous pattern generator that drives muscles to produce movement. Here, we show that M1 does not exhibit smooth dynamics during grasping movements, suggesting a more input-driven circuit.

[6] This manuscript is under revision.

Neural Population Dynamics in Motor Cortex are Different for Reach and Grasp

Aneesha K. Suresh*, James M. Goodman*, Elizaveta V. Okorokova, Matthew T. Kaufman, Nicholas G. Hatsopoulos, Sliman J. Bensmaia
bioRxiv 667196; doi: https://doi.org/10.1101/667196
*These authors contributed equally

7.1 | Results

Populations of neurons in primary motor cortex (M1) exhibit smooth dynamics in their responses when animals make reaching or cycling movements (Churchland et al. 2012; Shenoy et al. 2013; Lara et al. 2018; Russo et al. 2018). One interpretation of this population-level behavior is that M1 acts a pattern generator that drives muscles to give rise to movement. A major question is whether smooth population dynamics reflect a general principle of M1 function, or whether they underlie some behaviors but not others. To address this question, we examined the degree to which M1 exhibits smooth rotational dynamics during grasping movements, which involve a plant with a different function, more joints, and different mechanical properties than the arm, and which is subserved by a different portion of M1.

To this end, we recorded the neural activity in M1 and somatosensory cortex (SCx) using chronically implanted electrode arrays as monkeys performed a grasping task, restricting our analysis to responses before object contact (Figure S7.1). Animals were required to hold their arms still at the elbow and shoulder joints as a robotic arm presented each object to their contralateral hand. This task limits proximal limb movements and isolates grasping movements. For comparison, we also examined the responses of M1 populations during a center-out reaching task (Hatsopoulos et al. 2007).

First, we characterized the population dynamics in M1 during reaching and grasping movements (Figure 7.1). We used jPCA to search for rotational dynamics in a low-dimensional manifold of M1 population activity (Churchland et al. 2012). Replicating

previous findings, reaching evoked multiphasic activity in single M1 neurons (Figure 7.1A) and strong rotational dynamics in the population (Figure 7.1C). During grasp, individual M1 neurons again exhibited strong, multiphasic modulation (Figure 7.1B), but rotational dynamics were weak or absent (Figure 7.1D,E).

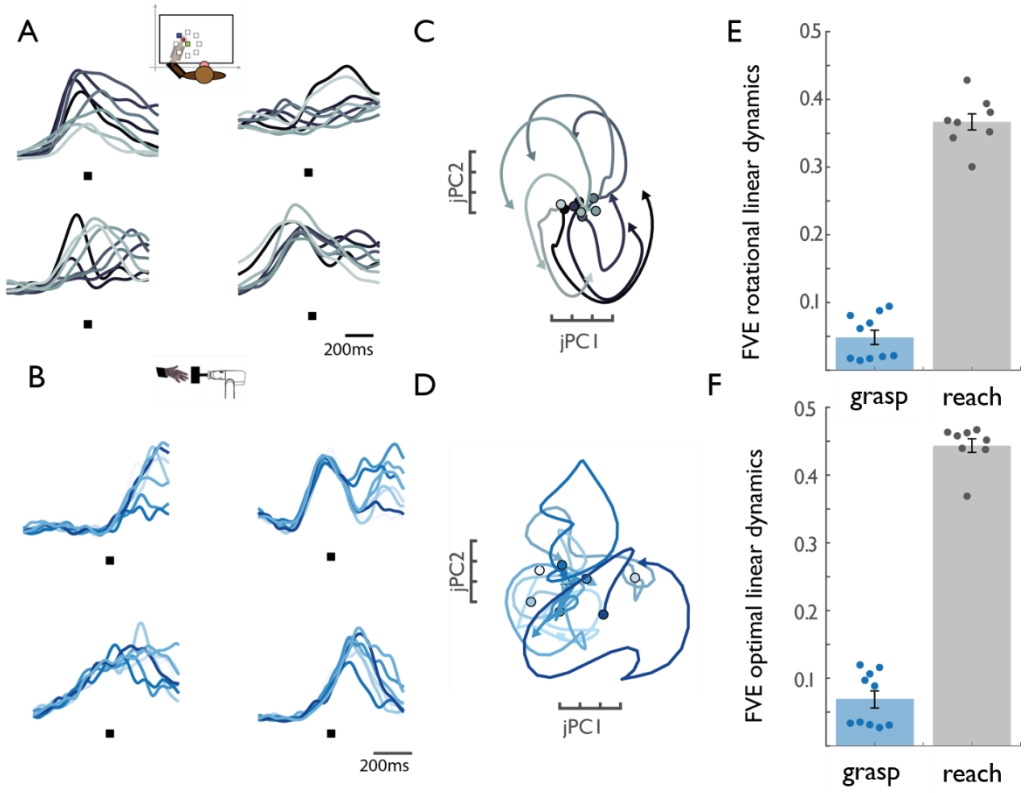

Figure 7.1 | M1 rotational dynamics during reaching and grasping.

A| Normalized peri-event histograms aligned to movement onset (black square) for 4 representative neurons during the reaching task. Each shade of gray indicates a different reach direction. **B|** Normalized peri-event histograms aligned to maximum aperture (black square) for 4 representative neurons during the grasping task. Each shade of blue indicates a different object group (see supplementary materials). **C|** Rotational dynamics in the population response during reaching along the first jPCA plane. Different shades of gray denote different reach directions. **D|** M1 rotational dynamics during grasping. Different shades of blue indicate different object groups. **E|** FVE (fraction of variance explained) in the rate of change of neural PCs (dx/dt) explained by the optimal rotational dynamical system. Difference is significant (two-sample two-sided equal-variance t-test, $t(16) = -19.44$, $p=4.67e-13$). Error bars denote standard error of the mean, and data points represent cross-

Figure 7.1, continued. validated results for 2 monkeys. **F**| FVE in the rate of change of neural PCs (d*x*/dt) explained by the optimal linear dynamical system. Difference is significant (two-sample two-sided equal-variance t-test, t(16) = -21.37 p=1.57e-14). Error bars denote standard error of the mean, and data points represent cross-validated results for 2 monkeys.

Given the poor fit of rotational dynamics to neural activity during grasp, we assessed whether activity could be described by a linear dynamical system of any kind. To test for linear dynamics, we fit a regression model using the first 10 principal components of the M1 population activity ($x(t)$) to predict their rates of change (dx/dt). We found $x(t)$ to be far less predictive of dx/dt in grasp than in reach, suggesting much weaker linear dynamics in the neural representation of grasp than reach (Figure 7.1F). We verified that these results were not an artifact of data alignment, analysis interval, peak firing rate, or population size (Figure S7.2).

The possibility remains that dynamics are present in M1 during grasp, but that they are higher-dimensional than during reach, or that they are nonlinear. Indeed, previous work analyzing neural state spaces in M1 during a reach-grasp-manipulate task found that neural activity is higher-dimensional than that observed during reach movements alone (Rouse and Schieber 2018). As a first test of these possibilities, we examined the relationship between movement and neural activity from the standpoint of decoding. We used a powerful recent technique, latent factor analysis via dynamical systems (LFADS), which infers and exploits latent dynamics to improve estimation of single-trial firing rates. Naturally, this benefit is only realized if the neural population acts like a dynamical system. Importantly, such dynamics are minimally constrained and can, in principle, be arbitrarily

high dimensional and/or highly nonlinear. We then used a standard Kalman filter to decode joint angle kinematics from the inferred latent factors (Figure 7.2).

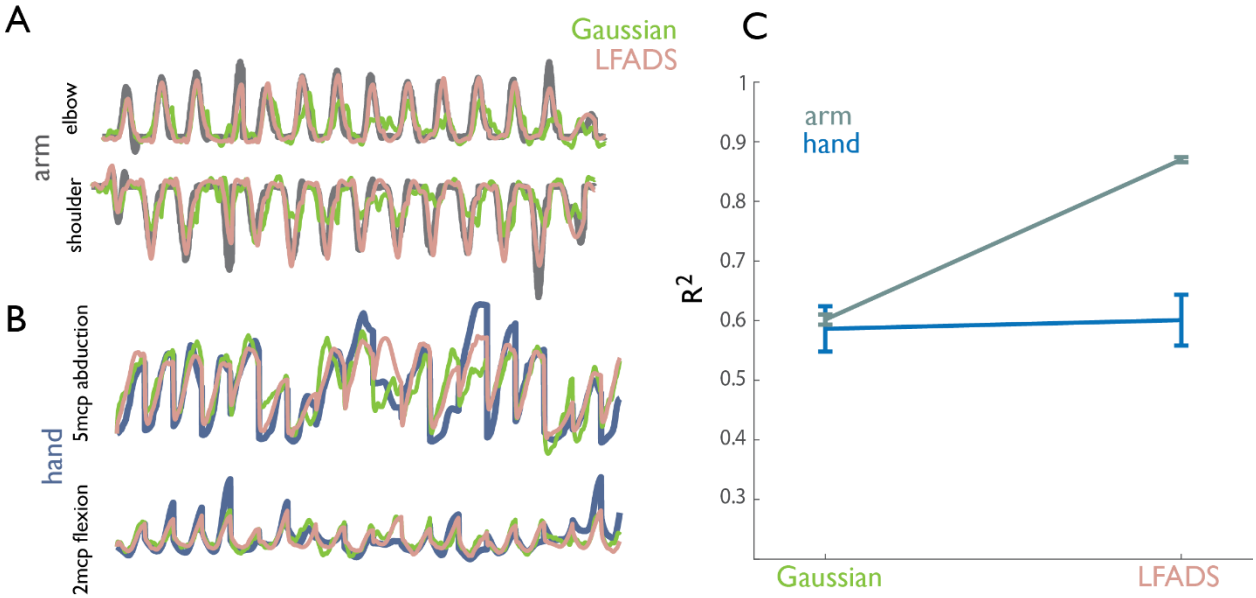

Figure 7.2 | Accuracy of Kalman filter decoders of kinematics using neural data pre-processed with Gaussian smoothing or with the assumption of underlying latent dynamics (LFADS).

A,B| Example kinematic traces reconstructed with and without the assumption of dynamics. **A|** Angles of arm joints (gray) along with angles decoded when neuronal responses are preprocessed with Gaussian kernel (green) and with LFADS (pink). **B|** Angles of hand joints (blue) along with their decoded counterparts (Gaussian smooth in green, LFADS in pink). **C|** Mean performance of decoders for the arm (2 DoF) and the hand (22 DoF), 10-fold cross-validated using a population of 44 neurons. Individual joint data shown in Supplementary Figure 7.3. LFADS leads to substantial improvements over typical pre-processing of neural data (Gaussian smoothing) for decoding reaching but not hand kinematics.

If latent dynamics are present in the system, LFADS should substantially improve kinematic decoding relative to simple Gaussian-smoothed spike trains. Replicating previous results, decoding accuracy was substantially improved for reaching when inferring firing rates using LFADS (Figure 7.2A,C). However, LFADS offered no accuracy improvement when decoding grasping kinematics (Figure 7.2B,C), even though grasp was

decoded just as well as reach under Gaussian smoothing of spike trains. These effects were consistent across all 30 degrees of freedom of the hand (Figure S7.3). These decoding results demonstrate that the strong dynamical structure seen in M1 population activity during reaching is not observed during grasp, even when dimensionality and linearity constraints are lifted.

As a separate way to gauge the presence of nonlinear dynamics in grasping responses, we computed a neural 'tangling' metric, which assesses the degree to which network dynamics are governed by a smooth and consistent flow field (Russo et al. 2018). In a smooth, autonomous dynamical system, neural trajectories passing through nearby points in state space have similar derivatives. The tangling metric (Q) assesses the degree to which this is the case over a specified (reduced) number of dimensions (Figure S7.4). During reaching, muscle activity and movement kinematics have been shown to exhibit more tangling than does M1 activity, presumably because the neural system acts as a pattern generator while muscles are input-driven (Russo et al. 2018). We replicated these results for reaching: neural activity (reduced to 15 dimensions) was much less tangled than the corresponding arm kinematics (position, velocity, and acceleration of joint angles)(Figure 7.3A). For grasp, however, M1 activity was somewhat *more* tangled than were the corresponding hand kinematics (Figure 7.3B).

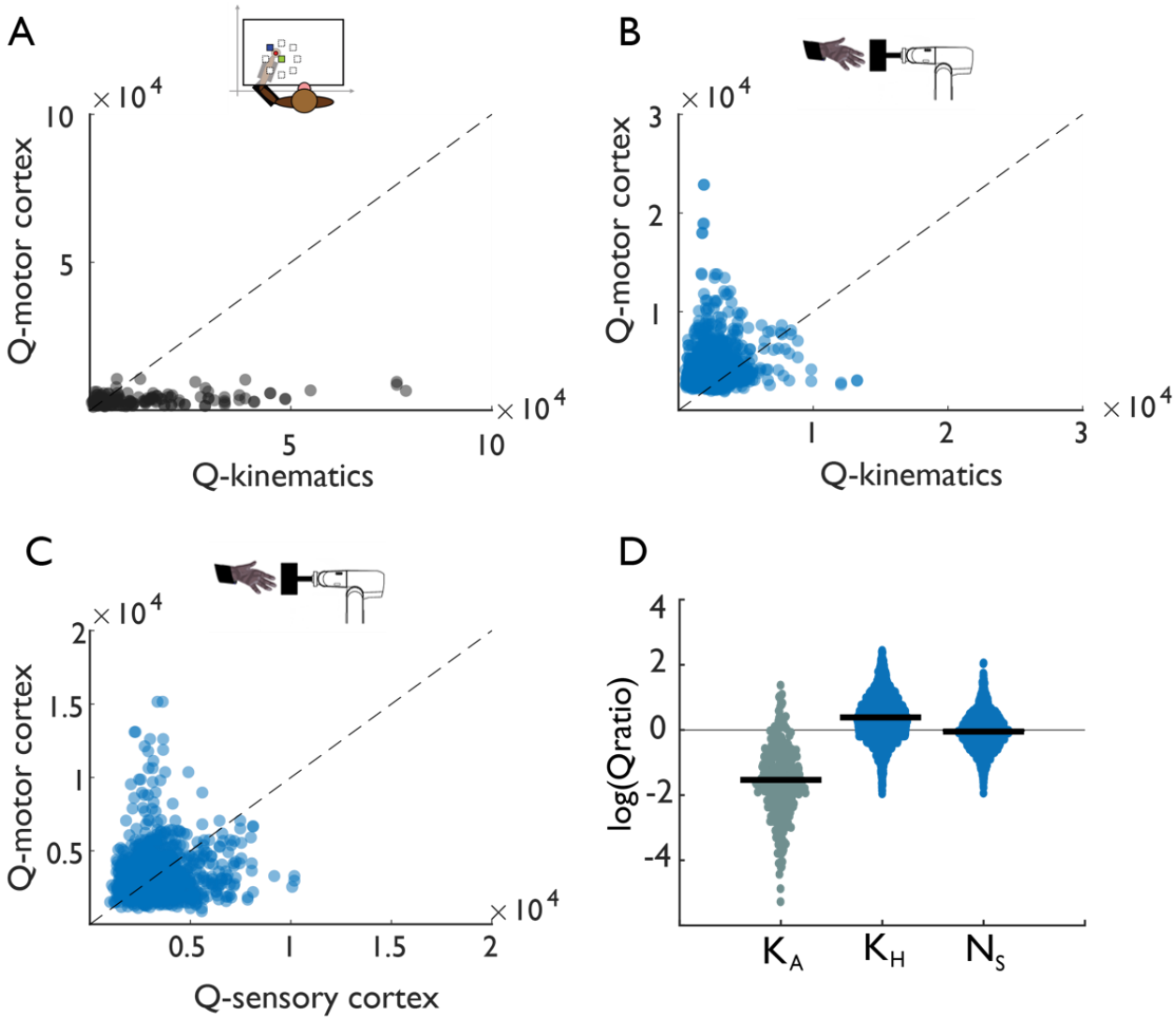

Figure 7.3 Tangling in reach and grasp.

A| Tangling metric (Q) for population responses in motor cortex during reaching vs. Q for reaching kinematics. Kinematic tangling is higher than neural tangling, consistent with motor cortex acting as a pattern generation during reach. **B**| Q-M1 population vs. Q-kinematics for grasping. Neural tangling is higher than kinematic tangling, which argues against pattern generation as the dominant drive during grasp. **C**| Q-M1 population vs. Q-SCx population. Neural tangling is similar in M1 and SCx, suggesting that M1 is as input driven as a sensory area. **D**| Summary results for two monkeys: Log of Q-motor/Q-kinematics of the arm during reach (K_A), Q-motor/Q-kinematics of the hand during grasp (K_H), and Q-motor/Q-sensory during grasp (N_s). Black bars denote mean. Differences are significant to reaching (two-sample two-sided equal-variance t-test: K_H | t(2978)=-43, p=1.03e-130 ; N_s |t(2978)=-39 p=1.87e-121).

Next, we compared tangling in M1 to tangling in SCx, which, as a sensory area, is expected to exhibit tangled activity (Russo et al. 2018). Surprisingly, M1 and SCx activity was similarly tangled during grasp (Figure 7.3C). In summary, then, M1 responses during grasp do not exhibit the properties of an autonomous dynamical system but rather resemble more input-driven responses (Figure 7.3D).

We speculate that the similar level of tangling observed in SCx and M1 may increased input activity in M1 during grasp than during proximal limb movements. Indeed, sensory feedback can obscure the intrinsic dynamics in neuronal circuits (Remington et al. 2018) and sensory representations are highly tangled (Russo et al. 2018). Furthermore, orderly dynamics have been observed during a single-finger pointing task in human subjects with ALS (Pandarinath et al. 2015), a condition wherein neuronal loss characterizes both M1 and SCx (Mochizuki et al. 2011). Finally, projections between primate somatosensory and motor cortices support communication between the two (Jones,' et al. 1978; Huerta and Pons 1990; Huffman and Krubitzer 2001), demonstrating a pathway by which M1 and SCx dynamics might be directly linked rather than driven by parallel inputs. While this pathway is not unique to the hand, it may be more engaged during grasp than reach.

In conclusion, we show that the lawful dynamics observed in M1 during reaching are not observed during grasping, and propose that this difference may be due to increased interplay between somatosensory and motor cortices during grasp.

7.2 | Methods

7.2.1 Behavior and neurophysiology for grasping task

We recorded single- and multi-unit responses in both the primary motor and somatosensory cortices (M1 and SCx) of two monkeys (Macaca mulatta) (M1: $N_1 = 53$, $N_2 = 58$ | SCx: $N_1 = 28$ $N_2 = 26$), and from M1 of a third monkey (M1: $N_3 = 80$), as they grasped each of 35 different objects an average of 10 times. We only used neural responses from Monkey 3 in the decoding analysis (from M1 responses) because we did not obtain enough data from this animal's SCx to use towards the tangling analysis. Neural recordings were obtained using semi-chronic electrode arrays (SC96 arrays, Gray Matter Research, Bozeman, MT) (Dotson et al. 2017) across six and nine sessions for Monkeys 1 and 2, respectively. Electrodes were moved to different depths on different sessions to capture new units. Units from Monkey 3 were recorded across two sessions from Utah electrode arrays (UEAs, Blackrock Microsystems, Inc., Salt Lake City, UT) and floating microelectrode arrays (FMAs, Microprobes for Life Science, Gaithersburg, MD) targeting rostral and caudal subdivisions of the hand representation of M1, respectively. Single units from all sessions (treated as distinct units) were extracted manually using Offline Sorter (Plexon Inc., Dallas TX). Units were identified based on inter-spike interval distribution and waveform shape and size.

Hand joint kinematics, namely the angles and angular velocities about all motile axes of rotation in the joints of the wrist and digits, were tracked at a rate of 100 Hz by means of a 14-camera motion tracking system (MX-T series, VICON, Los Angeles, CA). The VICON system tracked the three-dimensional positions of the markers, and joint angle kinematics were computed using inverse kinematics based on a musculoskeletal model of the human

arm (https://simtk.org/projects/ulb_project) (Dempster and Gaughran 1967; Yamaguchi and Zajac 1989; Delp et al. 1990; de Leva 1996; Anderson and Pandy 1999, 2001; Holzbaur et al. 2005) implemented in Opensim (https://simtk.org/frs/index.php?group_id=91) (Delp et al. 2007) with segments scaled to the sizes of those in a monkey limb. Task and kinematic recording methods are similar to previously reported ones (Saleh et al. 2010), but with a greater number of objects (35) and more detailed kinematic reconstructions (30 joints) (Goodman et al. 2019).

All surgical, behavioral, and experimental procedures conformed to the guidelines of the National Institutes of Health and were approved by the University of Chicago Institutional Animal Care and Use Committee.

7.2.2 Behavior and neurophysiology for reaching task

To compare grasp to reach, we analyzed previously-published single- and multi-unit responses from M1 of two additional monkeys (Macaca mulatta) (number of neurons from M1: $N_4 = 76$, , $N_5 = 107$) operantly trained to move a cursor in a variable-delay center-out reaching task (Hatsopoulos et al. 2007). The monkey's arm rested on cushioned arm troughs secured to links of a two-joint exoskeletal robotic arm (KINARM system; BKIN Technologies, Kingston, Ontario, Canada) underneath a projection surface. The shoulder and elbow joint angles were sampled at 500 Hz by the motor encoders of the robotic arm, and the *x* and *y* positions of the hand were computed using the forward kinematic equations. The center-out task involved movements from a center target to one of eight peripherally positioned targets (5 to 7 cm away). Targets full 360 degree rotation about the central target in 45 degree increments. Each trial comprised two epochs: first, an

instruction period lasting 1 to 1.5 s, during which the monkey held its hand over the center target to make the peripheral target appear; second, a "go" period, cued by blinking of the peripheral target, which indicated to the monkey that it could begin to move toward the target. Single- and multi-unit activity from each monkey was recorded from a UEA implanted into the upper limb representation of contralateral M1.

All surgical, behavioral, and experimental procedures conformed to the guidelines of the National Institutes of Health and were approved by the University of Chicago Institutional Animal Care and Use Committee.

7.2.3 Dynamics Data Analysis

Rotational Dynamics

Data pre-processing

For both the reach and grasp datasets, neuronal responses were aligned to the start of movement, resampled at 100 Hz so that reach and grasp data were at the same time resolution, averaged across trials, then smoothed by convolution with a Gaussian (20 ms S.D.). We then followed the same data pre-processing steps as outlined in Churchland et al. 2012: normalization of individual neuronal firing rates, subtraction of the cross-condition mean peri-event time histogram (PETH) from each neuron's response in each condition, and applying principal component analysis (PCA) to reduce the dimensionality of the population response. We used 10 dimensions instead of six (cf. Churchland et al. 2012) as a compromise between the lower-dimensional reach data kinematics and the higher-dimensional grasp data kinematics.

jPCA

We then applied to the population data (reduced to 10 dimensions by PCA) a published dimensionality reduction method, jPCA (Churchland et al. 2012), which finds orthonormal basis projections that capture rotational structure in the data. Specifically, the neural state is compared with its derivative and the strictly rotational dynamical system that explains the largest fraction of variance in that derivative is identified. The delay periods between the presentation/go-cue for the datasets varied, along with the reaction times, so we analyzed over time intervals (~500 ms) that maximized rotational variance for each dataset. For the reach data, data were aligned to the start of movement and the analysis window was centered on this event, whereas for the grasp data, data were aligned to maximum hand aperture, and we analyzed the interval centered on this event. These events were chosen for alignment as they were associated with both the largest peak firing rates and the strongest rotational dynamics. In some cases, the center of this 500-ms window was shifted between -250 ms to +250 ms relative to the alignment event to obtain an estimate of how rotational dynamics change over the course of the trial (e.g., Figure S7.2). Other alignment events were also tested, to validate robustness (Figure S7.2B).

Object clustering

Each of the 35 objects was presented 10 times per session, which yielded a smaller number of trials per condition than we used to assess jPCA during reaching (at least 40). To permit pooling across a larger number of trials when visualizing and quantifying population dynamics with jPCA (Figure 7.1), objects in the grasp task were grouped into eight object clusters on the basis of the trial-averaged similarity of hand posture across all 30 joint

degrees of freedom 10 ms prior to grasp (i.e., object contact). Objects were hierarchically clustered into 8 clusters on the basis of the Ward linkage function (MATLAB clusterdata). Eight clusters were chosen to match the number of conditions in the reaching dataset. Cluster sizes were not uniform; the smallest comprised 2 and the largest 9 different objects, with the median cluster comprising 4 objects.

We also assessed an alternative clustering procedure (Figure S7.2E) that guaranteed objects were divided into 7 equally-sized clusters (5 objects per cluster). Rather than determining cluster membership on the basis of a linkage threshold, cluster linkages were instead used to sort the objects on the basis of their dendrogram placements (MATLAB dendrogram). Clusters were obtained by grouping the first five objects in this sorted list into a common cluster, then the next five, and so on. This resulted in slightly poorer performance of jPCA (see *Quantification*).

For completeness, we also assessed jPCA without clustering (Figure S7.2E), which also resulted in slightly poorer performance and, by virtue of 35 neural trajectories instead of just 8, was considerably more difficult to visualize.

Quantification

In a linear dynamical system, the derivative of the state is a linear function of the state. We wished to assess whether a linear dynamical system could closely describe the neural activity. To this end, we first produced a denoised low-dimensional neural state (X) by using PCA. Second, we numerically differentiated X to produce the empirical derivative, $\dot{X}$. Next, we used regression to fit a linear model, predicting the derivative of the neuronal

state from the current state: $\dot{X} = MX$. Finally, we computed the fraction of variance explained (FVE) by this model:

Equation 7.1

$$FVE = 1 - \left\|\dot{X} - MX\right\|_{fro}^2 / \left\|\dot{X} - \langle\dot{X}\rangle\right\|_{fro}^2$$

M was constrained to be skew-symmetric (M_{skew}) unless otherwise specified; $\langle\cdot\rangle$ indicates the mean of a matrix across samples, but not across dimensions; and $\|\cdot\|_{fro}$ indicates the Frobenius norm of a matrix. Reaching data was 4-fold cross-validated, while grasp data was 5-fold cross-validated.

Control comparisons between arm and hand data

We performed several controls comparing arm and hand data to ensure that our results were not an artifact of trivial differences in the data or pre-processing steps.

First, we considered whether alignment of the data to different events might impact results. For the arm data, we aligned each trial to target onset and movement onset (Figure S7.2A). For the hand data, we aligned each trial to presentation of the object, movement onset, and the time at which the hand reached maximum aperture during grasp (Figure S7.2B). Rotational dynamics were strongest (though still very weak) when neuronal responses were aligned to maximum aperture so this alignment is reported throughout the main text.

Second, we assessed whether rotations might be obscured due to differences in firing rates in the hand vs. arm responses. To this end, we compared peak firing rates for trial-averaged data from the arm and hand after pre-processing (excluding normalization) to directly contrast the inputs to the jPCA analysis given the two effectors/tasks (Figure S7.2C). Peak

firing rates were actually higher for the hand than the arm, eliminating the possibility that our failure to observe dynamics during grasp was an artifact of weak responses.

Finally, we assessed whether differences in the sample size might contribute to differences in variance explained. To this end, we took five random samples of 55 neurons from the reaching data set – chosen to match the minimum number of neurons in the grasping datasets – and computed the cross-validated fraction of variance explained by the rotational dynamics. The smaller samples yielded identical fits as the full sample.

Tangling

We computed tangling of the neural population data (reduced to 15 dimensions by PCA) using a published method (Russo et al. 2018). In brief, the tangling metric estimates the extent to which neural population trajectories are inconsistent with what would be expected if they were governed by an autonomous dynamical system, with smaller values indicating consistency with such dynamical structure. Specifically, tangling measures the degree to which similar neural states, either during different movements or at different times for the same movement, are associated with different derivatives. This is done by finding, for each neural state (indexed by t), the maximum value of the tangling metric $Q(t)$ across all other neural states (indexed by t'):

Equation 7.2

$$Q(t) = \max_{t'} \frac{\|\dot{x}_t - \dot{x}_{t'}\|^2}{\|x_t - x_{t'}\|^2 + \varepsilon}$$

Here, x_t is the neural state at time t (a 15 dimensional vector containing the neural responses at that time), $\dot{x}_t$ is the temporal derivative of the neural state, and $\|\cdot\|$ is the Euclidean norm, while ε is a small constant added for robustness to noise (Russo et al.

2018). This analysis is not constrained to work solely for neural data; indeed, we also apply this same analysis to trajectories of joint angular kinematics to compare with the tangling of neural trajectories.

The neural data were pre-processed using the same alignment, trial averaging, smoothing, and normalization methods described above. Joint angles were collected for both hand and arm data. For this analysis, joint velocity and acceleration were computed (six total dimensions for arm, 90 dimensions for hand). For reaching, we analyzed the epoch from 200 ms before to 100 ms after movement onset. For grasping, we analyzed the epoch starting 200 ms before to 100 ms after maximum aperture. Neuronal responses were binned in 10 ms bins to match the sampling rate of the kinematics.

We tested tangling at different dimensionalities and selected the dimensionality at which Q had largely leveled off for both the population neural activity and kinematics (Figure S7.4), namely 6 for reach kinematics (the maximum) and 15 for grasp kinematics and for the neuronal responses.

7.2.4 Decoding

We analyzed the extent to which we can decode kinematics of the hand and the arm using neural population activity recorded from primary motor cortex and compared performance with and without the assumption of underlying dynamics. To this end, we used the M2 activity from monkey 3 (2 sessions with 44 and 36 M1 neurons and 20 kinematic DoF) performing the grasping task, and monkey 4 (64 M1 neurons and 2 kinematic DoF) performing the reaching task. We analyzed 800 ms of neural data preceding maximum

aperture of the hand in the grasping task, and neural data from 600 ms before to 200 ms after movement onset in the reaching task.

Preprocessing

For decoding, we preprocessed the neural data using one of the two methods: smoothing with a Gaussian kernel (σ = 20 ms) or latent factor analysis via dynamical systems (LFADS, Pandarinath et al., 2018).

LFADS is a generative model that assumes that observed spiking arises from an underlying dynamical system and approximates this system by training a sequential autoencoder. We fixed the number of factors in the model to 20 for both the arm and the hand datasets. We then performed PCA on the preprocessed neural activity and kept the components that cumulatively explained 90% of variance in the neural data.

Kalman Filter

To predict hand and arm kinematics, we applied the Kalman filter (Kalman 1960), commonly used for kinematic decoding (Wu et al. 2004; Menz et al. 2015). In this approach, kinematic dynamics can be described by a linear relationship between past and future states:

Equation 7.3

$$x_t = Ax_{t-1} + v_t$$

where x_t is a vector of joint angles at time t, A is a state transition matrix, and v_t is a vector of random numbers drawn from a Gaussian distribution with zero mean and covariance matrix V. The kinematics x_t can be also explained in terms of the observed neural activity $z_{t-\Delta}$:

Equation 7.4

$$x_t = Bz_{t-\Delta} + w_t$$

Here, $z_{t-\Delta}$ is a vector of instantaneous firing rates across a population of M1 neurons at time $t - \Delta$, B is an observation model matrix, and w_t is a random vector drawn from a Gaussian distribution with zero mean and covariance matrix W. We tested multiple values of the latency, Δ, and report decoders using the latency that maximized decoder accuracy (150 ms).

We estimated the matrices A, B, V, W using linear regression on each training set, and then used those estimates in the Kalman filter update algorithm to infer kinematics of each corresponding test set (see Faragher 2012 and Okorokova et al. 2015 for details) (Faragher 2012; Okorokova et al. 2015). Briefly, at each time t, kinematics were first predicted using the state transition equation (3), then updated with observation information from equation (4). Update of the kinematic prediction was achieved by a weighted average of the two estimates from (3) and (4): the weight of each estimate was inversely proportional to its uncertainty (determined in part by V and W for the estimates based on x_{t-1} and $z_{t-\Delta}$, respectively), which changed as a function of time and was thus recomputed for every time step.

To assess decoding performance, we performed 10-fold cross-validation in which we trained the parameters of the filter on a randomly selected 90% of the trials and tested the model using the remaining 10% of trials. Performance was quantified using the average coefficient of determination (R^2) for the held-out trials across test sets. We report performance for

each degree of freedom separately (Figure S7.3) and also the performance averaged across all degrees of freedom (Figure 7.2).

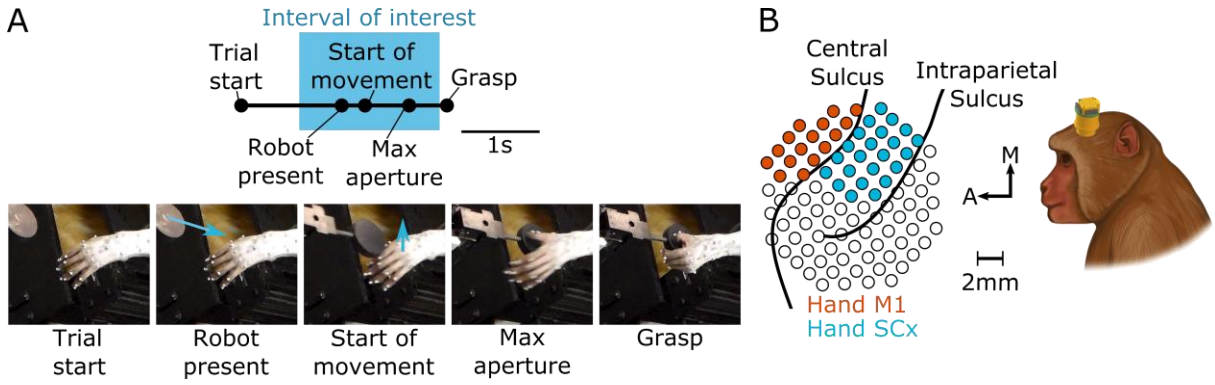

Supplementary Figure 7.1 Grasp Task Behavior and Neurophysiology.

A| Task Intervals: Start of Movement, Maximum Aperture, and Grasp epochs were manually scored from video. Arrows indicate motion of the robot presenting the object or of the hand. B| Multi-electrode arrays were used to record neuronal activity. The array spanned M1 and SCx, but only M1 units were used for this study except when explicitly noted (i.e., in the tangling analysis).

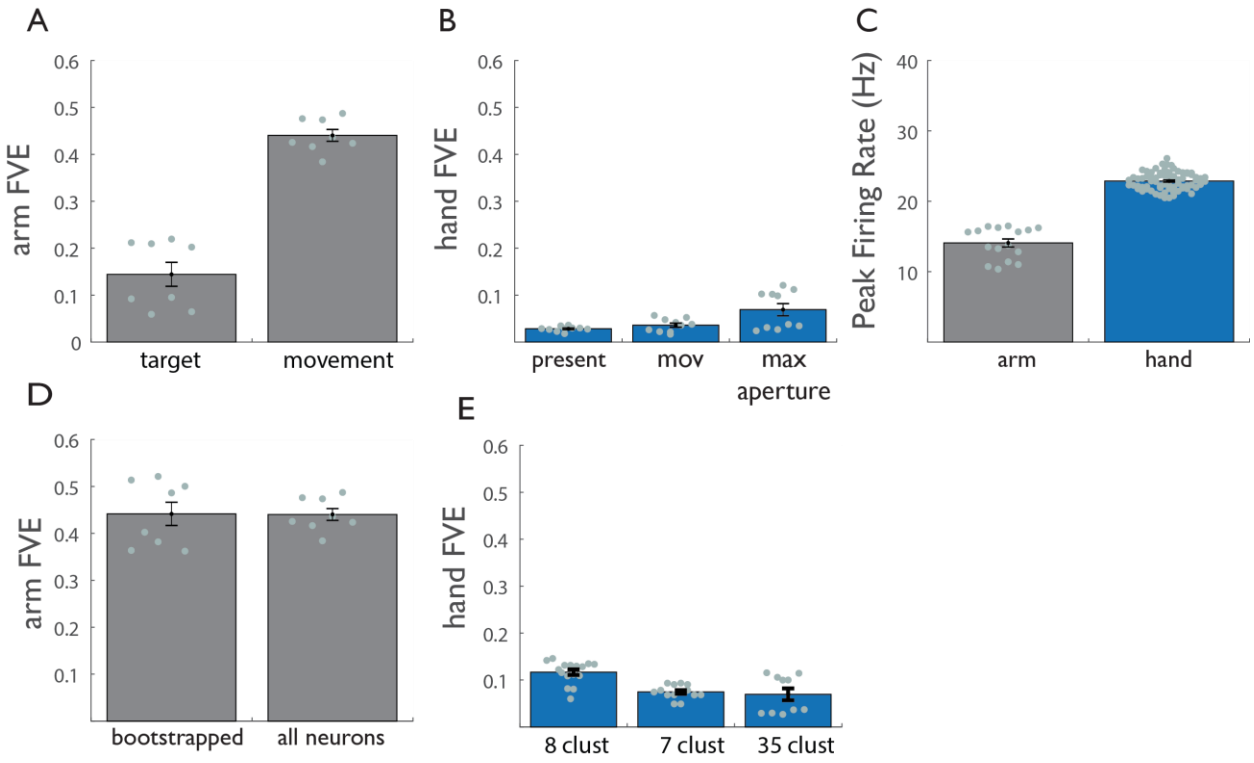

Supplementary Figure 7.2 | Control analyses for reaching and grasping.

A| For reaching: Cross-validated FVE (fraction of variance explained) in the rate of change of neural PCs (dx/dt) explained by the optimal linear dynamical system, with data aligned to target presentation (target) or movement onset (movement). B| For grasping: Cross-validated FVE in the rate of change of neural PCs (dx/dt) explained by the optimal linear dynamical system, when the data are aligned to object presentation (present), movement onset (mov), and maximum aperture (max aperture). C| Peak firing rate for arm (gray) and hand (blue) responses. D| Bootstrapped arm responses (55 neurons) vs. full arm dataset. E| Cross-validated fraction of variance explained (FVE) in the rate of change of neural PCs (dx/dt) explained by the optimal linear dynamical system when the objects are clustered into fewer categories for the hand (see methods). Difference between 8 clusters and 35 clusters is significant (p=.0008) while difference between 7 clusters and 35 clusters is not significant (p=0.57). However, for both clustering methods, difference between hand and arm remains highly significant (8 clusters| p=2.5e-18; 7 clusters | p=2.08e-19). For all figures, error bars represent standard error of the mean, and data points represent cross-validated results across 2 monkeys. Analysis is described in the supplementary methods section.

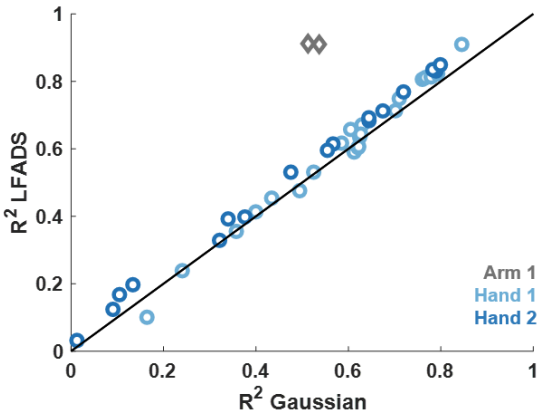

Supplementary Figure 7.3. Decoding performance is consistent across joints.

Mean performance of separate joints (individual points) derived from decoders with Gaussian smoothing or LFADS preprocessing for 1 arm dataset (grey: N = 44; 2 joints) and 2 hand datasets (light blue: N=44, dark blue: N = 36; 30 joints). For all joints, LFADS leads to substantial improvement in decoding for the arm but not for the hand. Reference line (black) indicates unity.

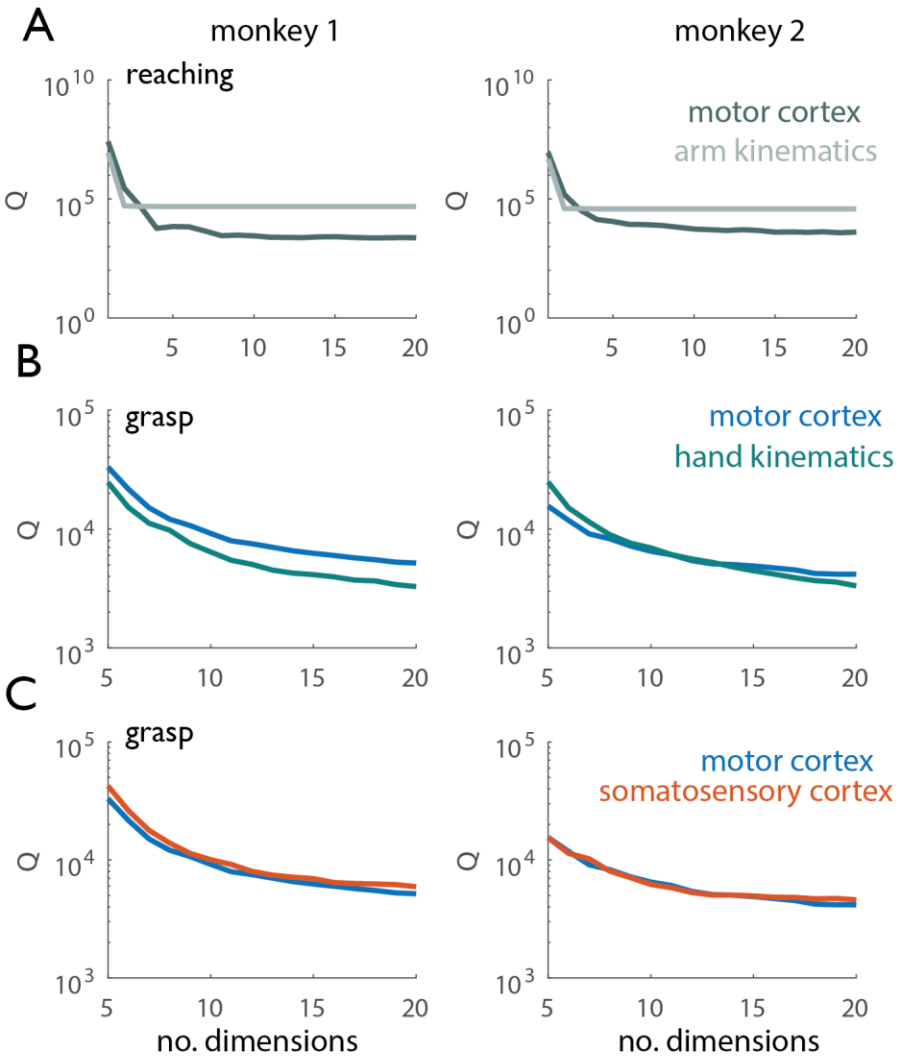

Supplementary Figure 7.4 | Tangling vs. dimensionality.

A| Tangling metric (90th percentile of Q) vs. number of dimensions used to compute Q for reaching. Q values derived from motor cortical responses are shown in dark gray, Q values derived from kinematics are shown in light gray. Arm kinematics exhibit consistently higher tangling than do the corresponding population responses in motor cortex. B| Tangling metric vs. number of dimensions used to compute Q for grasp. Q values derived from motor cortical responses are shown in blue, Q-values derived from hand kinematics are shown in green. When Q has leveled off for the kinematic and neural data (~15 dimensions), neuronal trajectories in motor cortex exhibit higher tangling than do the corresponding hand kinematic trajectories. C| Tangling metric vs. number of dimensions used to compute Q for reaching in motor and somatosensory cortex. Q-values derived from motor cortical responses are shown in blue, those derived from somatosensory responses are shown in orange. Hand motor and somatosensory responses exhibit similar tangling.

Anderson FC, Pandy MG. A Dynamic Optimization Solution for Vertical Jumping in Three Dimensions. *Comput Methods Biomech Biomed Engin* 2: 201–231, 1999.

Anderson FC, Pandy MG. Dynamic Optimization of Human Walking. *J Biomech Eng* 123: 381–390, 2001.

Brochier T, Boudreau MJ, Paré M, Smith AM. The effects of muscimol inactivation of small regions of motor and somatosensory cortex on independent finger movements and force control in the precision grip. [Online]. *Exp brain Res* 128: 31–40, 1999. http://www.ncbi.nlm.nih.gov/pubmed/10473737 [6 Aug. 2018].

Churchland MM, Cunningham JP, Kaufman MT, Foster JD, Nuyujukian P, Ryu SI, Shenoy K V. Neural population dynamics during reaching. *Nature* 487: 51–56, 2012.

Delp SL, Anderson FC, Arnold AS, Loan P, Habib A, John CT, Guendelman E, Thelen DG. OpenSim: Open-Source Software to Create and Analyze Dynamic Simulations of Movement. *IEEE Trans Biomed Eng* 54: 1940–1950, 2007.

Delp SL, Loan JP, Hoy MG, Zajac FE, Topp EL, Rosen JM. An interactive graphics-based model of the lower extremity to study orthopaedic surgical procedures. *IEEE Trans Biomed Eng* 37: 757–767, 1990.

Dempster WT, Gaughran GRL. Properties of body segments based on size and weight. *Am J Anat* 120: 33–54, 1967.

Dotson NM, Hoffman SJ, Goodell B, Gray CM. A Large-Scale Semi-Chronic Microdrive Recording System for Non-Human Primates. *Neuron* 96: 769–782, 2017.

Faragher R. Understanding the Basis of the Kalman Filter Via a Simple and Intuitive Derivation. *IEEE Signal Process Mag* : 128–132, 2012.

Goodman JM, Tabot GA, Lee AS, Suresh AK, Rajan AT, Hatsopoulos NG, Bensmaia SJ. Postural Representations of the Hand in Primate Sensorimotor Cortex. *bioRxiv* (March 2019). doi: 10.1101/566539.

Hallett M, Shahani BT, Young RR. EMG analysis of stereotyped voluntary movements in man. *J Neurol Neurosurg Psychiatry* 38: 1154–62, 1975.

Hatsopoulos NG, Xu Q, Amit Y. Encoding of movement fragments in the motor cortex. *J Neurosci* 27: 5105–14, 2007.

Holzbaur KRS, Murray WM, Delp SL. A Model of the Upper Extremity for Simulating Musculoskeletal Surgery and Analyzing Neuromuscular Control. *Ann Biomed Eng* 33: 829–840, 2005.

Huerta MF, Pons TP. Primary motor cortex receives input from area 3a in macaques. *Brain Res* 537: 367–371, 1990.

Huffman KJ, Krubitzer L. Area 3a: topographic organization and cortical connections in marmoset monkeys. *Cereb Cortex* 11: 849–67, 2001.

Jones,' EG, Coulter JD, Hendry SHC. lntracortical Connectivity of Architectonic Fields in the Somatic Sensory, Motor and Parietal Cortex of Monkeys [Online]. https://onlinelibrary.wiley.com/doi/pdf/10.1002/cne.901810206 [3 Jun. 2019].

Kalman RE. A New Approach to Linear Filtering and Prediction Problems. *Trans ASME–Journal Basic Eng* 82: 35–45, 1960.

Lara AH, Elsayed GF, Zimnik AJ, Cunningham JP, Churchland MM. Conservation of preparatory neural events in monkey motor cortex regardless of how movement is initiated. (2018). doi: 10.7554/eLife.31826.001.

de Leva P. Adjustments to Zatsiorsky-Seluyanov's segment inertia parameters. *J Biomech* 29: 1223–30, 1996.

Menz VK, Schaffelhofer S, Scherberger H. Representation of continuous hand and arm movements in macaque areas M1, F5, and AIP: a comparative decoding study. *J Neural Eng* 12: 056016, 2015.

Mochizuki Y, Mizutani T, Shimizu T, Kawata A. Proportional neuronal loss between the primary motor and sensory cortex in amyotrophic lateral sclerosis. *Neurosci Lett* 503: 73–75, 2011.

Okorokova E, Lebedev M, Linderman M, Ossadtchi A. A dynamical model improves reconstruction of handwriting from multichannel electromyographic recordings. *Front Neurosci* 9: 1–15, 2015.

Pandarinath C, Gilja V, Blabe CH, Nuyujukian P, Sarma AA, Sorice BL, Hochberg LR, Henderson JM, Shenoy K V. Neural population dynamics in human motor cortex during movements in people with ALS. *Elife* 4, 2015.

Pandarinath C, O'Shea DJ, Collins J, Jozefowicz R, Stavisky SD, Kao JC, Trautmann EM, Kaufman MT, Ryu SI, Hochberg LR, Henderson JM, Shenoy K V., Abbott LF, Sussillo D. Inferring single-trial neural population dynamics using sequential auto-encoders. *Nat Methods* 15: 805–815, 2018.

Polit A, Bizzi E. Processes controlling arm movements in monkeys. *Science* 201: 1235–7, 1978.

Remington ED, Narain D, Hosseini EA, Correspondence J, Jazayeri M. Flexible Sensorimotor Computations through Rapid Reconfiguration of Cortical Dynamics. *Neuron* 98: 1005–1019.e5, 2018.

Rouse AG, Schieber MH. Condition-Dependent Neural Dimensions Progressively Shift during Reach to Grasp. *Cell Rep* 25: 3158–3168.e3, 2018.

Russo AA, Bittner SR, Perkins SM, Seely JS, London BM, Lara AH, Miri A, Marshall NJ, Kohn A, Jessell TM, Abbott LF, Cunningham JP, Churchland MM. Motor Cortex Embeds Muscle-like Commands in an Untangled Population Response. *Neuron* 97: 953–966.e8, 2018.

Saleh M, Takahashi K, Amit Y, Hatsopoulos NG. Encoding of coordinated grasp trajectories in primary motor cortex. *J Neurosci* 30: 17079–90, 2010.

Shenoy K V., Sahani M, Churchland MM. Cortical Control of Arm Movements: A Dynamical Systems Perspective. *Annu Rev Neurosci* 36: 337–359, 2013.

Suresh AK, Hu X, Powers RK, Heckman CJ, Suresh NL, Rymer WZ. Changes in Motoneuron Afterhyperpolarization Duration in Stroke Survivors. [Online]. *J Neurophysiol* : jn.01091.2012-, 2014. http://jn.physiology.org/content/early/2014/06/09/jn.01091.2012.full-text.pdf+html.

Wu W, Black MJ, Mumford D, Gao Y, Bienenstock E, Donoghue JP. Modeling and Decoding Motor Cortical Activity Using a Switching Kalman Filter. *IEEE Trans Biomed Eng* 51: 933–942, 2004.

Yamaguchi GT, Zajac FE. A planar model of the knee joint to characterize the knee extensor mechanism. *J Biomech* 22: 1–10, 1989.

Chapter 8 | Conclusions

8.1 Summary of Results

Over the course of my dissertation project, I have explored various aspects of sensorimotor representations of the hand along the neuraxis. We began by investigating how individual tactile afferents encode task relevant features. In the first study, we explored the possibility that a key spatial feature – edge orientation – was encoded in temporal spiking sequences emitted by individual afferent responses. Having replicated in monkeys the phenomenon first documented in humans , we tested whether these orientation signals were robust to changes in other stimulus parameters, including intensity, scanning direction, and location. We found that slight changes in stimulus presentation abolished the ability to decode orientation from temporal sequences, calling into question whether these signals are interpretable by downstream structures under naturalistic conditions in which many stimulus features vary independently.

Next, we again probed feature coding in the responses of individual afferents, but this time in the context of texture perception. Previous studies had shown that our ability to discern fine textures is mediated by precise spiking sequences as the fingertip moves across the surface (Bensmaïa and Hollins 2003; Weber et al. 2013). These texture-specific temporal spiking patterns must remain stable when the movements used to explore the surface change for this neural code to be interpretable downstream. As we alluded to above, if these texture signals vary unpredictably across stimulus conditions, they become ambiguous. We found that the temporal structure of spiking sequences in individual afferents is consistent

across contact force levels, so that textures can be reliably classified across different force conditions when spike timing is taken into consideration. In other words, the temporal code for texture is robust to changes in contact force.

In summary, spiking responses in nerve fibers are nearly deterministic, with repeatable and precise patterning down to sub-millisecond timescales (see also: Johansson and Birznieks 2004; Mackevicius et al. 2012; Bale et al. 2015). Because tactile fibers generate virtually identical responses to repeated presentations of the same stimuli, and differ across stimuli, these response convey near perfect information about stimulus identity (Maia Chagas et al. 2013). As a result, any pair of stimuli can be differentiated based on evoked spiking patterns. However, it is critical to consider how these neural codes are interpreted downstream. Indeed, information about edge orientation carried by temporal spiking sequences is unreliable – because it is so dependent on other stimulus features – whereas information about texture is reliable – because it is invariant to other stimulus features (at least the ones tested). Temporal codes are thus viable in some contexts but not others. In summary, extracting stimulus information from afferent responses is not sufficient to define neural codes – we must strive to understand how these neural codes function in the context of downstream processing and perception. The behavioral relevance of the temporal code for texture was tested in a pair of studies that showed that the perceived roughness of a texture could be predicted from these temporal spiking patterns (Weber et al. 2013; Lieber and Bensmaia 2019a).

In a third study, we examined how populations of afferents encode features of contact rather than features of the objects themselves. The main conclusion was that population

responses during the initiation and termination of contact dwarf responses during maintained contact. In other words, populations of afferents encode contact transients, or changes in skin deformation, rather than the depth of deformation. Moreover, contact events are encoded in the time-varying spiking rates of activated neurons but in the size of the recruited population. Finally, we found that the spatiotemporal profile of the population response to contact events in cortex mirrors its counterpart in the nerve.

Next, we investigated, for the first time, the tactile response properties of neurons in the cuneate nucleus (CN), which constitutes the next level of tactile processing. First, we characterized the topographical organization of the dorsal column nuclei to accurately target receptive fields of the hand. We found that proprioceptive units tend to be more superficial than cutaneous ones, and units with RFs on the proximal limb tend to be more superficial and caudal to those with distal RFs. Having hoped to perform CN recordings in awake behaving monkeys using chronically implanted arrays, we were disappointed to find that the location of the hand representation within CN cannot be accessed using current array technologies. Indeed, we inserted two different types of chronic arrays into several monkeys (FMA and Utah arrays) and none of the implants yielded usable neuronal recordings.

We thus decided to investigate the tactile response properties of CN neurons in anesthetized macaques. In the process, we compared CN responses to their peripheral or cortical counterparts using data that has been previously collected in the lab, which constituted a unique opportunity observe the evolution of tactile signals as they ascend the neuraxis. We found that individual neurons in CN exhibit response properties indicative of

convergence of afferent sensory channels. Furthermore, at the population level, the dimensionality of CN responses and the coding of stimulus features imply an intermediate stage of processing between the nerve and cortex. These preliminary findings suggest that CN plays an active role in tactile processing. In upcoming studies, we will directly investigate the degree to which stimulus features, such as edge orientation or texture, are encoded in the responses of CN neurons, and compare these to their their cortical counterparts. I discuss these future studies in the "Next Steps" section of this chapter.

Finally. we investigated how populations of neurons in primary motor cortex (M1) give rise to grasping movements. Specifically, rotational dynamics have been observed in M1 population responses have been observed while monkeys make reaching movements. One interpretation of these neuronal dynamics is that M1 functions as a pattern generator. We wished to examine whether low-dimensional rotational dynamics are observed during grasping movements, which are complex than are reaching movements. We found that populations of M1 neurons do not exhibit smooth dynamics during grasping. In fact, M1 responses during grasping lack autonomous dynamics to the same extent as S1, a sensory area that is expected to be driven by inputs rather than by intrinsic dynamics. This property may reflect a greater interplay between somatosensory and motor cortices during grasping than during reaching.

8.2 Coding in Individual Neurons versus Populations of Neurons

Throughout this project, we explored neural coding at both the single cell level and at the population level. Emerging technologies are now enabling large-scale simultaneous recordings, on the order of thousands of neurons (Stringer and Pachitariu 2018). This

increased scale in data has been accompanied by an increased focus on population-level analysis methods to describe neural processing. Some have argued that populations of neurons, rather than individual neurons, are the essential unit of computation in the brain (Saxena and Cunningham 2019). Indeed, there have been discoveries about neural computation in the brain that would have been impossible with single unit analysis alone. In the context of stimulus coding, Rigotti et al. found that nonlinear mixed selectivity observed in individual neurons facilitates linear decoding of stimulus features at the population level (Rigotti et al. 2013; Fusi et al. 2016; Recanatesi et al. 2018). Nonlinear mixed selectivity implies that an additional neuron's responses cannot be explained by a linear superposition of the remaining responses to the individual parameters. The authors argued that higher order areas that relate to executive function may use ensembles of neurons as the functional computational unit, while lower sensory areas may use individual neurons. However, a new study examining expansive populations of primary visual cortical neurons has found that populations of V1 neurons encode information most efficiently when responses are high-dimensional and uncorrelated, indicating that nonlinear mixed selectivity may not be exclusive towards higher-cognitive areas, and may instead be a universal feature of neural coding in the brain (Lieber and Bensmaia 2019b; Stringer et al. 2019).

In chapters 2 through 4, we examined neural coding at the individual and population level across the first stage of tactile processing. We found that stimulus information is, in some cases, encoded in the responses of individual neurons, for example in the case of texture. In other cases, information is distributed over populations of neurons, for example in the

case of edge orientation. The dichotomy between single cell level and population level representations is a false one. Not only are there insights to be gleaned from analysis at both levels, but the basic representational unit is not consistently at the same level. For example, understanding texture signals might only be possible by examining individual neurons, whereas the representation of contact events is best studied at the population level.

Following afferent studies, our CN studies also reveal important insights at both the single neuron level, and at the population level. At the single unit level, we find that individual CN neurons receive convergent input from multiple sensory modalities, similar to their cortical counterparts. At the population level, we find that coding of stimulus features in CN represents an intermediate stage between the periphery and cortex. The manner in which afferent channels converge onto individual cortical neurons compared to CN neurons may reveal differences in how these structures process tactile signals and perform neural computations. Furthermore, understanding receptive field structure of individual units will allow us to understand the processing capabilities of CN. In this way, at processing stages beyond first-order afferents, both single unit and population level analysis can provide complementary evidence towards the same goal: to understand what neural computations are performed at each stage of sensory processing, and how stimulus features are represented in these areas.

In the final data chapter, we explore the structure of population-level representations of hand movements in motor cortex. Although the trend towards understanding neural manifolds, or the neural computations that underlie subspaces of neural populations, has

been growing steadily: there is still a debate on whether these results reveal new findings about the brain, or if they are simply recapitulating older studies with flashier methods (Elsayed and Cunningham 2017; Pillow and Aoi 2017). To address this concern, new methods to test whether population results arise out of elementary features described by individual neurons have been developed, to ensure that the "novel" population structure is not a simple byproduct of the population's primary features (Elsayed and Cunningham 2017). In the context of our study comparing hand and arm movement representations, we investigated whether the different neural dynamics observed for reach and grasp might trivially reflect differences in the kinematics (Georgopoulos et al. 1982). Unfortunately, these investigations were hindered by the need for complex encoding models, which quickly became computationally unwieldy. We were unable to conclusively determine whether traditional representationalist views of M1 might account for the observed neuronal dynamics.

Another major concern with population-level analyses is extracting low dimensional neural structure from highly stereotyped behaviors. Many population-level analyses use dimensionality reduction techniques to reveal low-dimensional manifolds that relate to behavior (Gallego et al. 2017). However, studies have shown that the dimensionality of the neural responses is constrained by the dimensionality of the task (Gao et al. 2017). In chapter 7, we acknowledge that the dimensionality of the grasping task is far higher than previous studies looking at reaching tasks. To ensure that differences in neural dynamics are not simply due to differences in dimensionality, we use various analyses (LFADs, tangling), that are differentially susceptible to differences in dimensionality.

8.3 Next Steps

8.3.1 Afferent coding during active tasks

Thus far, we have primarily investigated tactile coding with passive presentation of the stimuli to the motionless hand. However, the haptic perception of the three-dimensional structure of objects – termed stereognosis – requires active exploration and relies on the integration of touch and proprioception. Almost nothing is known about how this integration in effected in the somatosensory system. Efforts are underway at Northwestern University in the Miller lab to chronically implant arrays of electrode in the dorsal root ganglia, where the cell bodies of tactile nerve fibers are located, which will allow for recording of tactile and proprioceptive coding during active interaction with objects and will shed light on how naturalistic tactile coding and its integration with proprioceptive signals.

8.3.2 Coding of Behaviorally Relevant features in the CN

The initial scope of this thesis involved recording from awake behaving macaques, to understand how CN contributes to tactile processing. However, due to technical challenges alluded to above, we were unable to collect CN responses from awake macaques. Nevertheless, our anesthetized recordings reveal that CN plays a role in tactile processing. Much remains to be understood about the nature of the tactile representation in CN and how it differs from its peripheral and cortical counterparts. Specifically, we will scan random dot pattern stimuli across the skin that have been used to characterize the receptive field structure of tactile neurons in the nerve and in somatosensory cortex. We will also record CN responses to textures and to edges so that we can compare these tactile representations to their peripheral and cortical counterparts.

In parallel, we will continue to try to record from the hand representation in the CN of awake, behaving macaques. While proprioceptive signals and the occasional tactile signal from the proximal limb can be accessed through Utah arrays, emerging technologies, for example the N-form by modular bionics, may allow us to access the deeper tissues within CN where the hand representation is located.

8.3.3 Hand Representation in M1

In this thesis, we present one of the first studies to investigate neural population dynamics of hand movements. Most of this study focused on comparing neural dynamics with those observed in proximal arm studies, but there is a lot more to uncover about neural population dynamics during hand movements. For example, we can attempt to dissect why the dynamics underlying reaching different from those underlying grasping. Our hypothesis is that the lack of autonomous dynamics in M1 grasping responses reflects greater inputs. We can verify this hypothesis by reversibly inactivating potential sources of sensory input, including from the periphery (lidocaine) or from somatosensory cortex. Furthermore, we can record the dynamics during other dexterous manipulation behaviors that involve individuated finger movements, and search for structure where so far we have found none.

References

Bale MR, Campagner D, Erskine A, Petersen RS. Microsecond-scale timing precision in rodent trigeminal primary afferents. *J Neurosci* 35: 5935–40, 2015.

Bensmaïa SJ, Hollins M. The vibrations of texture [Online]. *Somatosens Mot Res* 20: 33–43, 2003. http://informahealthcare.com/doi/abs/10.1080/0899022031000083825 [21 Aug. 2014].

Elsayed GF, Cunningham JP. Structure in neural population recordings: an expected byproduct of simpler phenomena? *Nat Neurosci* 20: 1310–1318, 2017.

Fusi S, Miller EK, Rigotti M, Karpova A, Kiani R. Why neurons mix: high dimensionality for higher cognition This review comes from a themed issue on Neurobiology of cognitive behavior. *Curr Opin Neurobiol* 37: 66–74, 2016.

Gallego JA, Perich MG, Miller LE, Solla SA. Neural Manifolds for the Control of Movement. *Neuron* 94: 978–984, 2017.

Gao P, Trautmann E, Yu BM, Santhanam G, Ryu S, Shenoy K, Ganguli S. A theory of multineuronal dimensionality, dynamics and measurement. *bioRxiv* (November 5, 2017). doi: 10.1101/214262.

Georgopoulos AP, Kalaska JF, Caminiti R, Massey JT. On the relations between the direction of two-dimensional arm movements and cell discharge in primate motor cortex. *J Neurosci* 2: 1527–37, 1982.

Johansson RS, Birznieks I. First spikes in ensembles of human tactile afferents code complex spatial fingertip events. *Nat Neurosci* 7: 170–7, 2004.

Lieber JD, Bensmaia SJ. Emergence of an invariant representation of texture in primate somatosensory cortex. *bioRxiv* (May 24, 2019a). doi: 10.1101/646042.

Lieber JD, Bensmaia SJ. High-dimensional representation of texture in somatosensory cortex of primates. *Proc Natl Acad Sci U S A* 116: 3268–3277, 2019b.

Mackevicius EL, Best MD, Saal HP, Bensmaia SJ. Millisecond precision spike timing shapes tactile perception. *J Neurosci* 32: 15309–15317, 2012.

Maia Chagas A, Theis L, Sengupta B, Stüttgen MC, Bethge M, Schwarz C. Functional analysis of ultra high information rates conveyed by rat vibrissal primary afferents. *Front Neural Circuits* 7: 190, 2013.

Pillow JW, Aoi MC. Is population activity more than the sum of its parts? *Nat Neurosci* 20: 1196–1198, 2017.

Recanatesi S, Farrell M, Lajoie G, Deneve S, Rigotti M, Shea-Brown E. Signatures and mechanisms of low-dimensional neural predictive manifolds. *bioRxiv* (November 17, 2018). doi: 10.1101/471987.

Rigotti M, Barak O, Warden MR, Wang X-J, Daw ND, Miller EK, Fusi S. The importance

of mixed selectivity in complex cognitive tasks. *Nature* 497: 585–590, 2013.

Saxena, Shreya; Cunningham JP. Towards the neural population doctrine. *Curr Opin Neurobiol* 55: 103–111, 2019.

Stringer C, Pachitariu M. Computational processing of neural recordings from calcium imaging data This review comes from a themed issue on Machine Learning, Big Data, and Neuroscience. (2018). doi: 10.1016/j.conb.2018.11.005.

Stringer C, Pachitariu M, Steinmetz N, Carandini M, Harris KD. High-dimensional geometry of population responses in visual cortex. *Nature* 571: 361–365, 2019.

Weber AI, Saal HP, Lieber JD, Cheng JW, Manfredi LR, Dammann 3rd JF, Bensmaia SJ. Spatial and temporal codes mediate the tactile perception of natural textures. *Proc Natl Acad Sci U S A* 110: 17107–17112, 2013.